

GHASP : An $H\alpha$ kinematic survey of 203 spiral and irregular galaxies - VII. Revisiting the analysis of $H\alpha$ data cubes for 97 galaxies.

Epinat, B., Amram, P. & Marcelin M.

Laboratoire d'Astrophysique de Marseille, OAMP, Université Aix-Marseille & CNRS, 38 rue Frédéric Joliot-Curie, 13388 Marseille Cedex 13, France

Accepted. Received; in original form

ABSTRACT

The GHASP survey (Gassendi H α survey of SPirals) consists of 3D $H\alpha$ data cubes for 203 spiral and irregular galaxies, covering a large range in morphological types and absolute magnitudes, for kinematics analysis. It is the largest sample of Fabry-Perot data published up to now. In order to provide an homogenous sample, reduced and analyzed using the same procedure, we present in this paper the new reduction and analysis for a set of 97 galaxies already published in previous papers but now using the new data reduction procedure adopted for the whole sample. The GHASP survey is now achieved and the whole sample is reduced using adaptive binning techniques based on Voronoi tessellations. We have derived $H\alpha$ data cubes from which are computed $H\alpha$ maps, radial velocity fields as well as residual velocity fields, position-velocity diagrams, rotation curves and kinematical parameters for almost all galaxies. The rotation curves, the kinematical parameters and their uncertainties are computed homogeneously using the new method based on the power spectrum of the residual velocity field. This paper provides the kinematical parameters for the whole sample. For the first time, the integrated $H\alpha$ profiles have been computed and are presented for the whole sample. The total $H\alpha$ fluxes deduced from these profiles have been used in order to provide a flux calibration for the 203 GHASP galaxies. This paper confirms the conclusions already drawn from half the sample concerning (i) the increased accuracy of position angles measurements using kinematical data, (ii) the difficulty to have robust determinations of both morphological and kinematical inclinations in particular for low inclination galaxies and (iii) the very good agreement between the Tully-Fisher relationship derived from our data and previous determinations found in the literature.

Key words: Galaxies: spiral; irregular; dwarf; Galaxies: kinematics and dynamics;

1 INTRODUCTION

The GHASP survey consists of a large sample of spiral and irregular galaxies observed with a scanning Fabry-Perot for studying their kinematical and dynamical properties through the ionized hydrogen component. The goals of this study have been described in Epinat et al. (2008). The GHASP sample is by now the largest homogenous sample of Fabry-Perot data ever published, comprising 3D data for 203 galaxies. This paper is the seventh of a series called hereafter Paper I to VI (Garrido et al. 2002, 2003, 2004, 2005; Spano et al. 2007; Epinat et al. 2008) presenting the data obtained in the frame of the GHASP survey. The observations were lead during fourteen observing runs at the “Ob-

servatoire de Haute Provence (OHP)”, France, from 1998 to 2004. The survey is now achieved. The observing runs number 8 to 14 have been presented in Paper VI, which relies on a set of 108 galaxies, providing 106 velocity fields and 93 rotation curves. Those data have been reduced with the new data reduction procedure (see Paper VI and references therein). The data presented in this paper are those of the seven first observing runs (already presented in Papers I to IV) that have been re-reduced using the same method as in Paper VI. It also contains data for UGC 3382 and UGC 11300 that have been improved by adding new data (runs 3, 5 and 6) to the ones already published in Paper VI (runs 10

and 13). Thus, the data presented here consist of a set of 97 galaxies, providing 96 velocity fields and 82 rotation curves.

To be clear on the goals and limits of this present work, we summarize hereafter what we present and what we do not in this paper. We present:

- the new individual maps and position-velocity diagrams in Appendix D (on line data only),
- the new rotation curves, in Appendix E and the new corresponding tables in Appendix F.

In this paper, we lead the same kind of analysis as the one presented in Paper VI concerning:

- the study of the parameters of the kinematical models,
- the study of the residual velocity fields,
- the Tully-Fisher relation.

Because it is useful to display and analyze all the data together, we put here in the same tables (in Appendix B) the new parameters and the results already published in Paper VI so that the reader does not have to compile tables coming from different publications. With respect to Papers I to IV, some distances and absolute magnitudes have been re-computed (using better estimations). For the whole GHASP sample we make a new analysis on an absolute flux calibration made using the data calibrated by James et al. (2004) and the integrated $H\alpha$ profiles deduced from our data cubes.

Because this has been discussed in previous papers, we do not present any more:

- the morphological types and luminosity distributions of the whole GHASP sample (see Paper VI),
- the data reduction procedure used here, including the computation of the rotation curves, the determination of the kinematical parameters and the determination of the uncertainties (see Paper VI),
- the instrumental set-up of the instrument for the data re-reduced in this paper (see Papers I to IV),
- the individual comments for each galaxy (see Papers I to IV), except when the new reduction procedure leads to new comments or to conclusions noticeably different from the previous ones (see Appendix A).

In section 2 we make an indirect flux calibration of the $H\alpha$ profiles. In section 3 we present the data and in section 4 we compute the Tully-Fisher relation. In section 5 we give the summary and conclusions. When the distances of the galaxies are not known, a Hubble constant $H_0=75 \text{ km s}^{-1} \text{ Mpc}^{-1}$ is used throughout this paper.

2 CALIBRATION AND $H\alpha$ PROFILES

Even if direct flux calibration is always possible using well calibrated and extended $H\alpha$ emitters like planetary nebulae (Dopita & Hua 1997), during the observations, we decided not to calibrate our data, thus saving observing time. Indeed, our major scientific goal was not to use the Fabry-Perot technique to make photometric studies but kinematic ones. We estimated that $H\alpha$ flux calibrations require additional observing times ranging from 25 to 33%. Nevertheless, an indirect calibration of the total $H\alpha$ flux of the 201/203 galaxies from the GHASP sample has been made using 69 of the 71 galaxies we have in common with James et al.

(2004). From their study using narrow band filters including $H\alpha$ and [NII], James et al. (2004) provided calibrated fluxes for their sample of 334 galaxies. Our spectral resolution allows us to resolve the $H\alpha$ line, moreover the full width half maximum (FWHM) of the narrow band filters are narrow enough to reject [NII]. This is not the case for James et al. (2004) who do not separate $H\alpha$ from [NII] lines. We have corrected this effect assuming a mean and constant spectral ratio $H\alpha/[NII]=3$. Distinct calibrations have been made depending on the observing setup. Indeed, the GHASP sample has been obtained using a 256×256 IPCS (Imaging Photon Counting System) until March 2000 (runs number 1 to 4) and with a new 512×512 IPCS since October 2000 (runs number 5 to 14), with respective pixel scales of $0.96''$ and $0.68''$ (given in Table B1). We reject from the calibration the galaxies for which we have added data observed with both detectors. Their flux was computed *a posteriori* by taking into account the response of each detector and the corresponding exposure time. To compute the total $H\alpha$ flux for each galaxy, we compute the $H\alpha$ profile by summing the flux in the spectrum of each spatial element (see Appendix C). To minimize the foreground sky contamination, only the spatial elements used to compute the different moments (monochromatic images, velocity fields, ...) have been added. We use the velocity field in order to disentangle free spectral range overlaps. We correct the fluxes from the interference filter response, taking into account the aperture of the instrument, the inclination of the filter and its temperature during the observations. We subtract the continuum taking into account the periodicity of the Fabry-Perot transmission (difference between the free spectral range of the interferometer and the FWHM of the interference filter). The systemic velocity computed from the kinematical model (vertical dashed line in Figure C1) is globally well centered on the integrated $H\alpha$ profile. Figure 1 shows the comparison between James et al. (2004) fluxes and our estimated fluxes for the old IPCS (top) and the new IPCS (bottom). The linear regressions are plotted with the dashed lines and their coefficients are respectively $0.73\pm 0.13 \text{ } 10^{-16} \text{ W m}^{-2} \text{ ph}^{-1} \text{ s}$ and $0.48\pm 0.06 \text{ } 10^{-16} \text{ W m}^{-2} \text{ ph}^{-1} \text{ s}$. The fluxes estimated from this calibration are presented in Table B1.

3 DATA ANALYSIS

As detailed in Paper VI, the same procedure (adaptive binning, sky subtraction, ghost removals, ...) has been used to compute the data cubes and the maps deduced from these cubes. For each galaxy, in Appendix D (available online only), from Figure D1 to D96, when possible, we present five frames per figure: the XDSS blue (or red) image (top/left), the $H\alpha$ velocity field (top/right), the $H\alpha$ monochromatic image (middle/left) and, when a model fits the velocity field, the $H\alpha$ residual velocity field (middle/right) and finally, the position-velocity diagram along the major axis (bottom). The white and black double crosses indicate the centers used for the kinematical analysis (given in Table B1, see Paper VI for details) while the black line traces the kinematical major axis deduced from the velocity field analysis (see Paper VI) or the morphological one (taken from HyperLeda) when no position angle of the kinematical major axis could be derived using the kinematics (e.g. Table

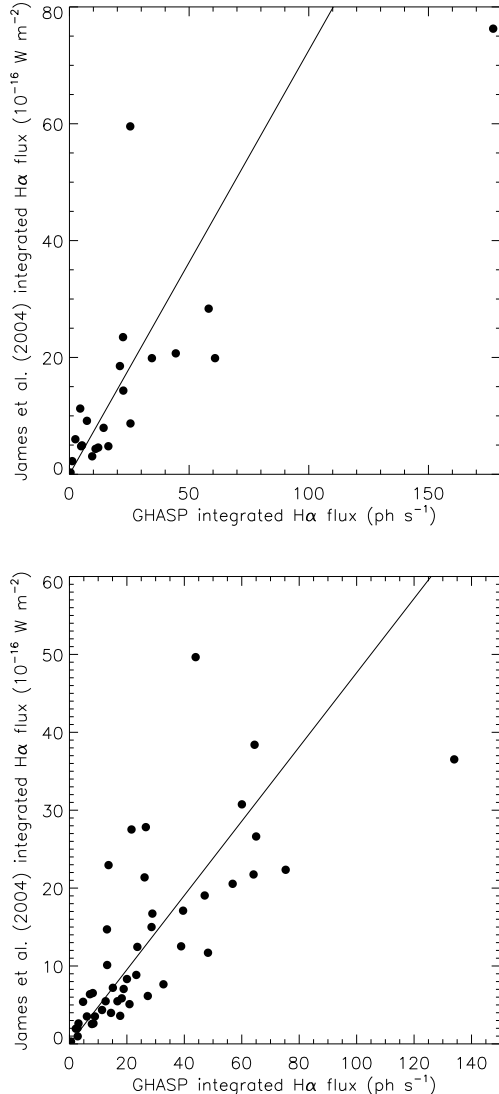


Figure 1. $H\alpha$ flux measured by GHASP versus $H\alpha$ flux from James et al. (2004). The dashed line represents the linear regression on the data from which results our calibration. **Top:** calibration for the IPCS 512x512. **Bottom:** calibration for the IPCS 256x256.

B2). This line ends at the radius $D_{25}/2$ corresponding to the isophotal level 25 mag arcsec $^{-2}$ in the B-band (given in Table B3) in order to compare the velocity field extent with the optical disk of the galaxies. Position-velocity diagrams are computed along the axis defined by this black line, using a virtual slit width of seven pixels. The red line superimposed on the position-velocity diagram is the rotation curve deduced from the model velocity field along this virtual slit (see Paper VI). When no fit is satisfactory (generally because of poor signal-to-noise ratio), we used the real velocity field instead of the model (see individual captions in Figures D1 to D96). The rotation curves are given in Appendix E (figures) and F (tables). They are computed and displayed following the method described in Paper VI. These figures are also available on the Fabry-Perot data base: <http://FabryPerot.oamp.fr/>. Appendix F (that

contains the tables corresponding to the rotation curves) is available online only. The curves are plotted with both sides superimposed in the same quadrant, using different symbols for the receding (crosses) and approaching (dots) side (with respect to the center). The black vertical arrow on the X-axis represents the radius $D_{25}/2$ while the smaller grey arrow on the X-axis represents the transition radius (defined in Paper VI), always smaller than $D_{25}/2$ by definition.

For galaxies seen almost edge-on (inclination higher than 75°) our model does not describe accurately the rotation of a galaxy (see Paper VI). Furthermore, for UGC 1249, UGC 2082, UGC 3851, UGC 4278, UGC 5272, UGC 5935 and UGC 11909, neither rotation curve nor residual velocity fields have been plotted. For them, the position-velocity diagram gives more suitable information than the rotation curve and allows the peak-to-peak or peak-to-valley velocity distribution along the major axis to be followed.

The rotation curves recomputed in this paper may be different from the ones published in Papers I to V since: (i) the adaptive binning gives different weights to low signal-to-noise ratio regions in the velocity field from which is computed the rotation curve; (ii) the exclusion sector around the minor axis is always set at 22.5° (in the galaxy plane) contrarily to what had been done in previous papers where the exclusion sector varied from one galaxy to the other; (iii) the inclination and major axis position angle may be different; (iv) the center may have changed. Indeed, as has been done in Paper VI, the velocity field center chosen to compute the rotation curve matches the morphological center (nucleus) when it is unambiguously defined from the morphology. No comment is given in Appendix A unless the differences between the previous and the new velocity fields and rotation curves lead to inconsistent results.

The mean velocity dispersion on each residual velocity field has been computed for each galaxy and tabulated in Table B2. Details on the computation and on the analysis of residual velocity fields are given in Paper VI. Taking into account the whole sample, the plot presented in Paper VI has been updated in Figure 2. It still shows that the residual velocity dispersion is correlated with the maximum amplitude of the velocity field (shown by the dashed linear regression). We observe a set of galaxies with a high residual velocity dispersion (points above the dotted line in Figure 2). These points correspond to galaxies: (i) dominated by strong bars (UGC 89, UGC 3013, UGC 11283 and UGC 11407), or strong spiral structures (UGC 5786 and UGC 3334) and not correctly described by our model which does not take into account non-axisymmetric motions; (ii) having velocity fields of lower quality (UGC 1655, UGC 1736, UGC 3382, UGC 3528, IC 476, UGC 4256, UGC 4456, UGC 4543, IC 2542, UGC 6277, UGC 6523, UGC 9406, UGC 10502, UGC 11269, UGC 11891 and UGC 12276), all these galaxies present a mean size of the bins greater than 25 pixels and an integrated total $H\alpha$ flux on average lower than $2.7 \pm 2.6 \cdot 10^{-16} \text{ W m}^{-2}$. We also confirm that there is no evidence for correlations between the residual velocity dispersion and the morphological type or the presence of a bar (when it is not dominating the potential of the galaxy).

The morphological parameters (input parameters of the fits) and the results of the fits (kinematical parameters, χ^2 , and parameters of the residual maps) are given in Table B2. Morphological types, distances, absolute magnitudes M_B ,

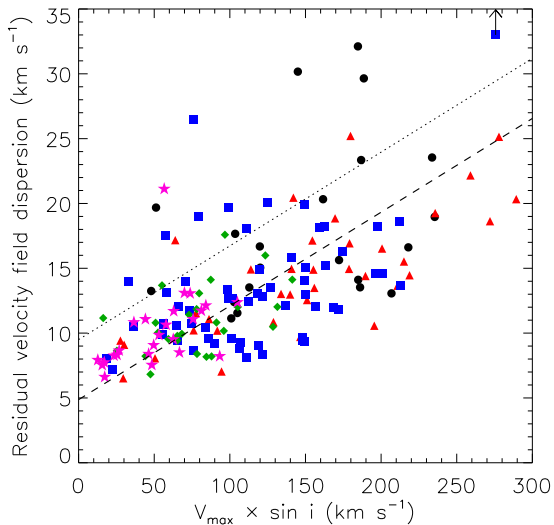


Figure 2. Dispersion in residual velocity field versus maximum velocity, subdivided by Hubble morphological type: black circles $0 \leq t < 2$, red triangles $2 \leq t < 4$, blue squares $4 \leq t < 6$, green rhombuses $6 \leq t < 8$ and pink stars $8 \leq t < 10$. The dashed line represents the linear regression on the data. The points above the dotted line are discussed in section 3. UGC 3334 labelled with an arrow has actually a huge residual velocity dispersion of 54 km s^{-1} (see Table B2).

optical radii $D_{25}/2$, axis ratios and references for HI velocity fields compiled from the literature are given in Table B3, together with maximum velocity parameters computed from the rotation curves (V_{max} and quality flag on V_{max}). The 25 galaxies larger than the field of view of the instrument are flagged in Col. 8 of Table B3. The galaxies for which it was necessary to decrease the degrees of freedom of the model have their fixed parameters flagged with an asterisk (*) in Table B2 (see Paper VI for more details).

The kinematical position angles obtained by GHASP are compared with the photometric position angles (found in HyperLeda) and plotted in Figure 3. The error bar on the morphological position angle has been estimated using the axis ratio and optical radius uncertainties; for clarity, only one morphological position angle is plotted (see Paper VI). In Figure 3, we have used special symbols for galaxies with no accurate morphological position angle (red open circles) and with an inclination lower than 25° (blue squares). Most of the galaxies showing a disagreement in position angles larger than 20° present: (i) a bad morphological determination of the position angle; or (ii) a kinematical inclination lower than 25° ; or (iii) are specific cases discussed in Appendix A or in Appendix B of Paper VI (namely these galaxies are: UGC 3013, UGC 3740, IC 476, UGC 4256, UGC 4273, UGC 4422, UGC 4543, UGC 5931, UGC 10310, UGC 10359, UGC 10470, UGC 10445, UGC 10897, UGC 11283, UGC 11861 and UGC 12060). Morphological position angles of low inclination galaxies have systematically higher uncertainties than kinematical ones (see Figure 3). For kinematical inclinations greater than 25° , the mean error on morphological position angles is $\sim 20^\circ$ and the mean error on kinematical position angles is $\sim 2^\circ$. For inclinations

lower than 25° the difference is larger: the mean error on morphological position angles is $\sim 40^\circ$ while the mean error on kinematical position angles is $\sim 3^\circ$. For the whole sample, the histogram of the variation between kinematical and morphological position angles given in Figure 3 (bottom) indicates that (i) for 57% of the galaxies, the agreement is better than 10° ; (ii) for 79%, the agreement is better than 20° ; (iii) the disagreement is larger than 30° for 15% of the galaxies. The conclusion addressed in Paper VI remains valid, i.e. integral field spectroscopy constitutes the best technique to determine position angles and as a consequence, rotation curves.

The kinematical and morphological inclinations are compared in Figure 4. On the top panel, the photometric inclination is computed using a correction factor depending on the morphological type (see Paper VI). On the middle panel the photometric inclination is derived from the axis ratio. Galaxies for which the morphological position angle could not be determined accurately are represented by red open circles while galaxies with a difference between morphological and kinematical position angles larger than 20° are displayed with blue squares. The conclusions given in Paper VI are still valid: (i) the agreement between photometric and kinematical inclinations is better for high inclination galaxies; (ii) morphological inclination determination is unreliable if the measure of the position angle is not reliable; (iii) the errors on morphological inclinations and on kinematical inclinations are comparable; (iv) kinematical methods may underestimate (or morphological method overestimate) the inclination; (v) the kinematical inclinations are closer to the morphological inclinations when the latter are computed without any correction for the morphological type (see Figure 4 top and middle). The histogram of the difference between morphological and kinematical inclinations (Figure 4, bottom) shows that a difference of inclination larger than 10° is found for less than 40% of the sample. Taking into account the whole GHASP sample, the number of galaxies by bin is higher and the histogram is more symmetrical with respect to that computed in Paper VI.

4 THE TULLY-FISHER RELATION

Among the whole sample of 203 galaxies, we have plotted the Tully-Fisher relation (Tully & Fisher 1977, M_B as a function of $\log 2V_{max}$) for a sub-sample of 177 galaxies in Figure 5. The 26 other galaxies are not considered in the present discussion because (i) for seven galaxies the rotation curve does not reach the maximum rotation velocity (UGC 1117, UGC 1655, UGC 2455, UGC 4393, UGC 6523, UGC 8898 and UGC 9406); (ii) no B magnitude is available for three galaxies (UGC 2800, UGC 11496, UGC 12212) and (iii) no velocity measurement, either on the rotation curve or on the position-velocity diagram is possible for 16 other galaxies (see Table B3). The maximum velocity V_{max} and its error have been obtained from the fit to the velocity field and the solid line in Figure 5 is the relation found by Tully & Pierce (2000) (see Paper VI).

In Figure 5 (Top), the error bars on the velocity are displayed and galaxies with inclination lower than 25° are distinguished (blue open squares). As already noticed in Paper VI, these galaxies have statistically higher velocities than

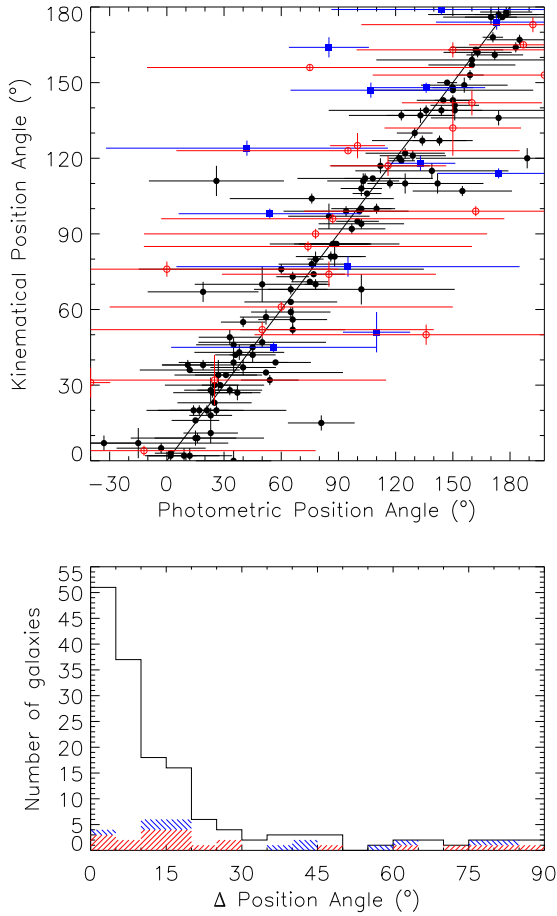


Figure 3. Top: kinematical versus morphological (HyperLeda) position angles of the major axis. Galaxies for which no accurate morphological position angle has been computed are shown by red open circles; galaxies having an inclination lower than 25° are displayed by blue squares; the other galaxies are represented by black circles. **Bottom:** histogram of the variation between kinematical and morphological position angles. The red hash, blue hash and residual white represent respectively the galaxies for which no accurate position angle has been measured, for which inclination is lower than 25° and the other galaxies of the sample.

expected from the Tully & Pierce (2000) relation and have large error bars. Considering this effect, we choose to exclude the 22 galaxies with inclinations lower than 25° from the Tully-Fisher analysis (see Paper VI). Among the 155 remaining galaxies, the maximum velocity V_{max} is reached for 76 of them (black dots, large size), probably reached for 44 of them (blue squares, medium size) and probably not reached for 35 of them (red triangles, small size). They are distinguished in Figure 5 (Middle) and flagged in Table B3. The quality flag on the maximum velocity is given in Table B3 (see Paper VI).

Figure 5 (Middle) confirms the two classifications “ V_{max} probably reached” and “ V_{max} probably not reached” since for the majority of each class the points are respectively in agreement and above the Tully & Pierce (2000) relation. From the two classes “ V_{max} reached” and “ V_{max} probably

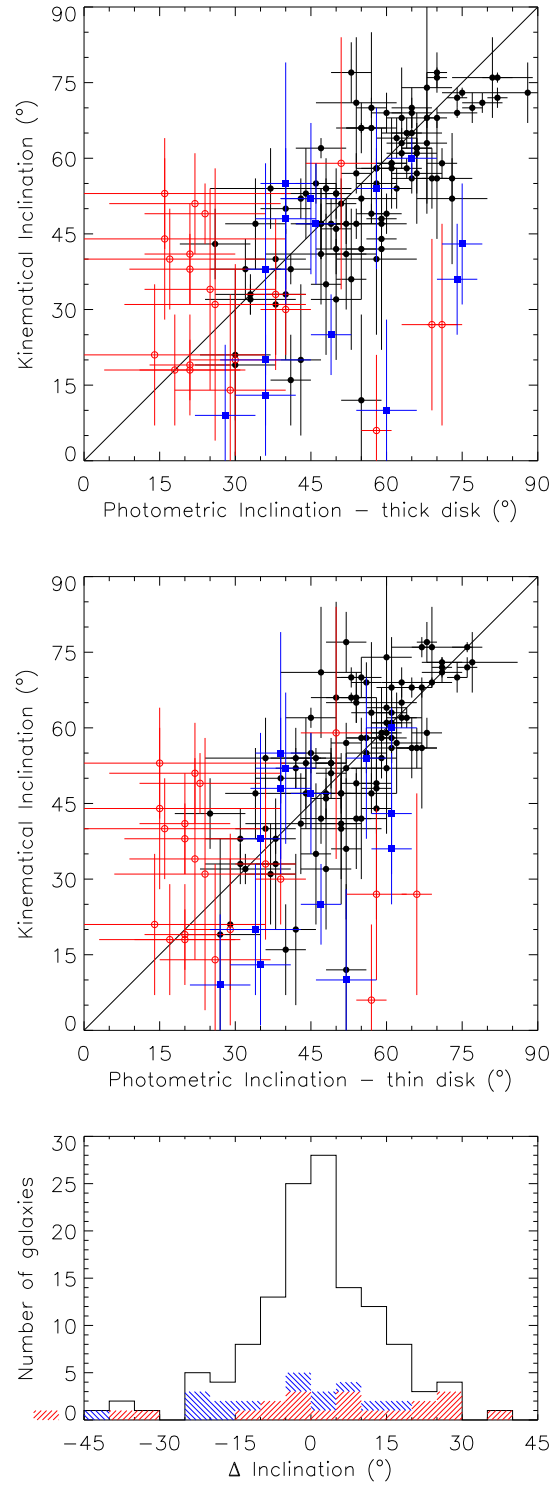


Figure 4. Top: kinematical versus thick disk morphological inclinations. **Middle:** kinematical versus thin disk morphological inclinations. **Top and Middle:** Galaxies for which no accurate morphological position angle has been computed are shown by red open circles; galaxies with a difference between the kinematical and morphological position angles larger than 20° are displayed with blue squares; the other galaxies are represented by black circles. **Bottom:** histogram of the variation between kinematical and morphological inclinations. The red hash, blue hash and residual white represent respectively the galaxies for which no accurate position angle has been measured, for which the differ-

reached”, we find the following relation (see Paper VI for additional details):

$$M_B = (-7.2 \pm 1.2)[\log 2V_{max} - 2.5] - (19.8 \pm 0.1) \quad (1)$$

This relation is displayed as a dashed line in Figure 5, in which morphological types are distinguished for the two best classes (black circles from 0 to 2, red triangles from 2 to 4, blue squares from 4 to 6, green rhombuses from 6 to 8 and pink stars from 8 to 10). The slope of the linear regression computed here from the whole GHASP sample is now exactly the same as the one computed by Tully & Pierce (2000) (this slope was found to be somewhat lower in Paper VI), and its uncertainty has been reduced by a factor 0.75. For the Tully-Fisher relation, we note that fast rotators ($V_{max} > 300 \text{ km s}^{-1}$: UGC 89, UGC 508, UGC 3429, UGC 4422, UGC 4820, UGC 5532, UGC 8900, UGC 8937, UGC 9969 and UGC 11470) are less luminous than expected. This trend has already been noticed and discussed in Paper VI.

5 SUMMARY AND CONCLUSIONS

The knowledge of the links between the kinematical and dynamical state of galaxies helps us to increase our understanding of the physics and evolution of galaxies. The GHASP sample, which consists of 203 spiral and irregular galaxies, covering a wide range of morphological types and absolute magnitudes, has been constituted in order to provide a kinematical reference sample of nearby galaxies. The galaxies have been observed in the $H\alpha$ line using Fabry-Perot techniques, leading to the construction of data cubes. This sample is by now the largest set of galaxies ever homogeneously observed with Fabry-Perot techniques. Major improvements in the reduction (adaptive binning techniques, ghost suppression, treatment of faint outskirts regions, etc) and in the analysis (determination of the rotation curve and of the kinematical parameters and their uncertainties, etc) have been developed and implemented in the data reduction procedure and homogeneously applied to the whole GHASP sample (see Paper VI for additional details).

In this paper, 97 galaxies have been re-reduced using adaptive binning techniques in order to provide homogeneous data for the whole sample. For each galaxy, we have presented the $H\alpha$ velocity field, the $H\alpha$ monochromatic image and eventually the $H\alpha$ residual velocity field, the position-velocity diagram along the major axis and the rotation curve, when available, leading for the whole sample to 200 velocity fields and 177 rotation curves.

From the data cubes, integrated $H\alpha$ profiles have also been produced. A post calibration has allowed to compute indirect absolute $H\alpha$ flux for all the galaxies belonging to the GHASP sample. This post calibration has been done using fluxes for 69 galaxies found in the literature (James et al. 2004).

We confirm and strengthen most of the results already obtained from half the sample:

- A high quality model has been achieved to represent the axi-symmetric rotational component of the galaxies since no typical signatures for biases are observed in the residual velocity fields. This means that the residuals observed in the residual velocity field are due to actual non circular motions and not to an incorrect determination of the kinematical

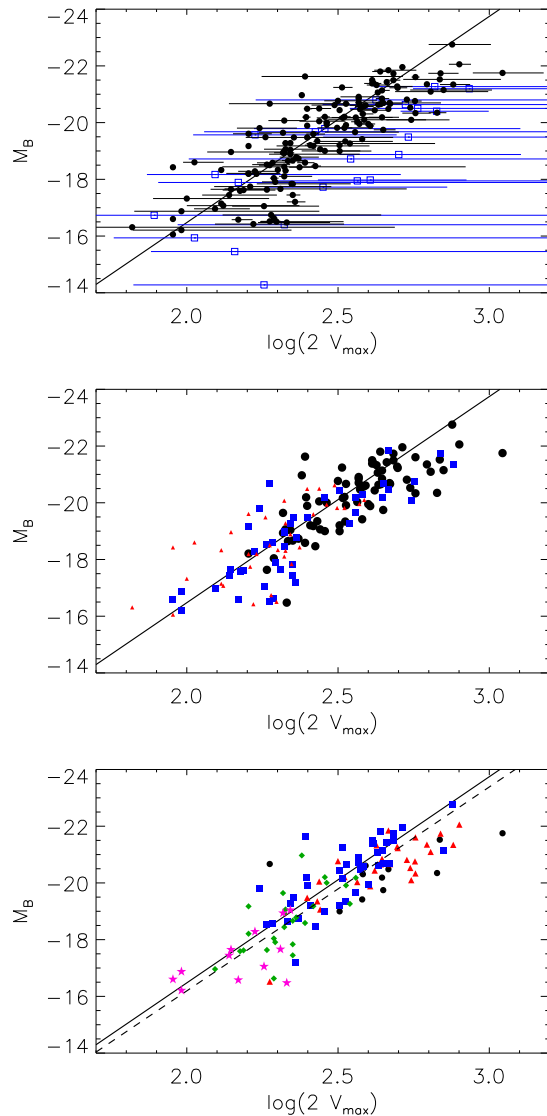


Figure 5. TF relation for our sample of galaxies. The solid line represents the B magnitude Tully-Fisher relation determined by Tully & Pierce (2000) from nearby galaxies in clusters (Ursa Major, Pisces filament, Coma). **Top:** subdivided by inclination - low inclination galaxies ($i < 25^\circ$): blue squares; other galaxies ($i \geq 25^\circ$): black circles. **Middle:** subdivided by V_{max} flags - V_{max} reached: black dots, large size; V_{max} probably reached: blue squares, medium size; V_{max} probably not reached: red triangles, small size. **Bottom:** subdivided by morphological type - black circles from 0 to 2; red triangles from 2 to 4; blue squares from 4 to 6; green rhombuses from 6 to 8; pink stars from 8 to 10; the dashed line represents the best linear fit to the data.

parameters (position of the center, position angle, inclination and rotation velocity). In addition, the position-velocity diagrams confirm the validity of the rotation curves.

- The mean residual velocity dispersion is strongly correlated with the maximum amplitude of the velocity field. For a given velocity range, this correlation does not clearly depend on the morphological type. However strongly barred galaxies have a higher residual velocity dispersion than mild-

barred or unbarred galaxies. Peculiar galaxies also show a high residual velocity dispersion.

- The determinations of kinematical position angles are robust whatever the inclination of the galaxy whereas morphological position angles are poorly determined for low inclination systems. Moreover, morphological position angles have systematically higher uncertainties than kinematical ones. This is a major argument for deriving rotation curves from integral field spectroscopy rather than long slit spectroscopy instruments that could lead to incorrect positioning of the slit (a difference between the morphological and kinematical position angles larger than 30° is found for $\sim 15\%$ of the GHASP sample). This may strongly bias mass distribution models and Tully-Fisher studies. In order to build a mass model, the stellar mass distribution derived from the surface brightness profile is combined with the rotation curve deduced from the velocity field. The position angles of the major axis deduced from the surface brightness image and from the velocity field should be identical. Important inconsistencies may appear if these position angles are misaligned.

- Galaxies with poor determination of their morphological position angles have usually unreliable and overestimated morphological inclinations. The agreement between kinematical and morphological inclinations is better when assuming a thin disk in particular for high inclination galaxies. For galaxies with intermediate disk inclinations (higher than 25° and lower than 75°), to improve the quality of the rotation curve, it is possible to reduce the degrees of freedom in kinematical models by fixing the inclination to the morphological value. This is specially true when only low quality kinematical data are available as it is the case for high redshift galaxies.

- The use of the whole GHASP sample leads to a Tully-Fisher relationship in perfect agreement with Tully & Pierce (2000), despite important differences in the selection of both samples. With respect to the result presented in Paper VI, the use of the whole sample increases the agreement with Tully & Pierce (2000). Three comments should be underlined: (i) galaxies with inclination lower than 25° are inappropriate for Tully-Fisher relation determination since their estimated velocities are easily overestimated; (ii) fast rotators ($V_{max} > 300 \text{ km s}^{-1}$) are maybe less luminous (than expected from the Tully-Fisher relation); (iii) for fast rotators and high luminosity galaxies, the agreement with the Tully-Fisher relation is better when the morphological inclination of the galaxy is computed without taking into account the increasing thickness of the disk when the morphological type of the galaxies moves from early to late types.

From these data and analysis, it is now possible to address the scientific drivers on the whole GHASP sample in forthcoming papers.

ACKNOWLEDGEMENTS

The authors warmly thank their collaborators: Philippe Balard, Chantal Balkowski, Jacques Boulesteix, Olivier Boissin, Claude Carignan, Laurent Chemin, Olivier Daigle, Jean-Luc Gach, Olivia Garrido and Olivier Hernandez for having participated to the previous works making possible the new analyze of the observations. They thank Is-

abelle Jégouzo and Christian Surace for building the Fabry-Perot Database. The authors wish to thank the referee Dr P. James who helped improving the manuscript. They also thank the Programme National Galaxies for supporting the GHASP project in allocating continuously observing time during several years, the Observatoire de Haute-Provence team for its technical assistance during the observations. This research has made use of the NASA/IPAC Extragalactic Database (NED) which is operated by the Jet Propulsion Laboratory, California Institute of Technology, under contract with the National Aeronautics and Space Administration. The authors have also made an extensive use of the HyperLeda Database (<http://leda.univ-lyon1.fr>). The Digitized Sky Surveys were produced at the Space Telescope Science Institute under U.S. Government grant NAG W-2166. The images of these surveys are based on photographic data obtained using the Oschin Schmidt Telescope on Palomar Mountain and the UK Schmidt Telescope. The plates were processed into the present compressed digital form with the permission of these institutions.

REFERENCES

- de Vaucouleurs G., 1979, APJ, 227, 380
 Dopita M. A., Hua C. T., 1997, APJS, 108, 515
 Epinat B., Amram P., Marcelin M., Balkowski C., Daigle O., Hernandez O., Chemin L., Carignan C., Gach J. ., Balard P., 2008, ArXiv e-prints, 805
 Garrido O., Marcelin M., Amram P., 2004, MNRAS, 349, 225
 Garrido O., Marcelin M., Amram P., Balkowski C., Gach J. L., Boulesteix J., 2005, MNRAS, 362, 127
 Garrido O., Marcelin M., Amram P., Boissin O., 2003, AAP, 399, 51
 Garrido O., Marcelin M., Amram P., Boulesteix J., 2002, AAP, 387, 821
 Haynes M. P., Giovanelli R., Salzer J. J., Wegner G., Freudling W., da Costa L. N., Herter T., Vogt N. P., 1999, AJ, 117, 1668
 Irwin J. A., 1994, APJ, 429, 618
 James P. A., Shane N. S., Beckman J. E., Cardwell A., Collins C. A., Etherton J., de Jong R. S., Fathi K., Knapen J. H., Peletier R. F., Percival S. M., Pollacco D. L., Seigar M. S., Stedman S., Steele I. A., 2004, AAP, 414, 23
 Karachentsev I. D., Karachentseva V. E., Huchtmeier W. K., Makarov D. I., 2004, AJ, 127, 2031
 Koopmann R. A., Haynes M. P., Catinella B., 2006, AJ, 131, 716
 Kornreich D. A., Haynes M. P., Lovelace R. V. E., van Zee L., 2000, AJ, 120, 139
 Laine S., Gottesman S. T., 1998, MNRAS, 297, 1041
 Marcum et al. P. M., 2001, APJS, 132, 129
 Moustakas J., Kennicutt Jr. R. C., 2006, APJS, 164, 81
 Nilson P., 1973, Nova Acta Regiae Soc. Sci. Upsaliensis Ser. V, pp 0–+
 Noordermeer E., van der Hulst J. M., Sancisi R., Swaters R. A., van Albada T. S., 2005, AAP, 442, 137
 O’Connell R. W., Gallagher III J. S., Hunter D. A., 1994, APJ, 433, 65

- Paturel G., Andernach H., Bottinelli L., di Nella H., Durand N., Garnier R., Gouguenheim L., Lanoix P., Marthinet M. C., Petit C., Rousseau J., Theureau G., Vauglin I., 1997, *AAPS*, 124, 109
- Paturel G., Fang Y., Petit C., Garnier R., Rousseau J., 2000, *AAPS*, 146, 19
- Paturel G., Garcia A. M., Fouque P., Buta R., 1991, *AAP*, 243, 319
- Rownd B. K., Dickey J. M., Helou G., 1994, *AJ*, 108, 1638
- Saha A., Thim F., Tammann G. A., Reindl B., Sandage A., 2006, *APJS*, 165, 108
- Schulman E., Bregman J. N., Brinks E., Roberts M. S., 1996, *AJ*, 112, 960
- Shapley A., Fabbiano G., Eskridge P. B., 2001, *APJS*, 137, 139
- Spano M., Marcelin M., Amram P., Carignan C., Epinat B., Hernandez O., 2007, *MNRAS*, pp 1084–+
- Springob C. M., Masters K. L., Haynes M. P., Giovanelli R., Marinoni C., 2007, *APJS*, 172, 599
- Swaters R. A., 1999, PhD thesis, , Rijksuniversiteit Groningen, (1999)
- Swaters R. A., Madore B. F., van den Bosch F. C., Balcells M., 2003, *APJ*, 583, 732
- Swaters R. A., van Albada T. S., van der Hulst J. M., Sancisi R., 2002, *AAP*, 390, 829
- Tully R. B., Fisher J. R., 1977, *AAP*, 54, 661
- Tully R. B., Pierce M. J., 2000, *APJ*, 533, 744
- Tully R. B., Verheijen M. A. W., Pierce M. J., Huang J.-S., Wainscoat R. J., 1996, *AJ*, 112, 2471
- van der Kruit P. C., Allen R. J., 1978, *ARAA*, 16, 103
- Vauglin I., Paturel G., Borsenberger J., Fouqué P., Epchtein N., Kimeswenger S., Tiphène D., Lanoix P., Courtois H., 1999, *AAPS*, 135, 133
- Wilcots E. M., Prescott M. K. M., 2004, *AJ*, 127, 1900
- Wilcots E. M., Turnbull M. C., Brinks E., 2001, *APJ*, 560, 110
- Williams B. A., Yun M. S., Verdes-Montenegro L., 2002, *AJ*, 123, 2417

APPENDIX A: NOTES ON INDIVIDUAL GALAXIES

UGC 508. HI inclination (25° , Noordermeer et al. 2005) as well as photometric inclination (14° , from an axis ratio of 0.97) lead to a very high maximum rotation velocity ($\sim 550 \text{ km s}^{-1}$). From Tully-Fisher relationship, its absolute magnitude M_B suggests a maximum velocity around 270 km s^{-1} , leading to an axis ratio of 0.5 (hence an inclination of 60°). This strongly barred galaxy shows moreover clear evidence for interaction, resulting in perturbed morphology and velocity field. This biases the determination of the inclination by morphological as well as kinematical methods, leading to an unrealistically high maximum rotation velocity.

UGC 1117. This galaxy is the famous M33. Because of the limited field-of-view of GHASP we only observed the solid body central part of the rotation curve. The external round shape structures in the different images are due to edge-effects of the interference filter vignetting the field-of-view.

UGC 1249. No rotation curve has been computed because of its high inclination (90°).

UGC 1256. Within $\sim 25''$ ($\sim 1 \text{ kpc}$), the rotation curve shows negative rotation velocity. This is due to the fact that the bar is almost parallel to the major axis.

UGC 1736. The kinematical center chosen in Paper IV is different from the morphological center chosen here, leading to a different rotation curve.

UGC 1913. Same comment as for UGC 1736.

UGC 2023. Despite the fact that this galaxy has been observed again (2 hours exposure time on September 11th 2002) and that these data have been compared and added to the data presented in Paper II, the signal-to-noise ratio remains very weak. From the R-band image observed by James et al. (2004), it is now possible to accurately determine the center of that very low surface brightness object. The major axis position angle and the inclination have been set to the values determined from HI data Swaters (1999). The kinematical center chosen in Paper II is quite different from the one used here ($13''$ westward now, which is 0.5 kpc), leading to a very different shape for the rotation curve. Despite the fact that the systemic velocities are almost the same, in Paper II the rotation curve reaches a plateau at $\sim 20''$ whereas, with the new rotation center, the rotation curve now shows a solid body shape up to $60''$.

UGC 2034. Despite the fact that this galaxy has been observed again for 1.5 hours (on September 12th 2002) and that these data have been compared and added to the data presented in Paper II, the signal-to-noise ratio remains very weak. Due to the lack of rotation and of spatial coverage, our model does not converge. Thus the parameters have been set to HI values from Swaters (1999).

UGC 2045. A difference of 6° is computed between the major axis position angle given in this paper and in Paper IV. This is due to the warp which biases the automatic determination of the major axis position angle with respect to the morphological one. It leads to little change however in the rotation curve. The maximum rotation velocity is thus directly taken from the position-velocity diagram plot.

UGC 2053. The signal-to-noise ratio and the total H α flux of this galaxy are very low. The new maps are not much

different from the ones published in Paper II, so that they are not presented here.

UGC 2080. The determination of the inclination of this almost face-on galaxy leads to lower value when using the kinematics than when using the morphology. A too low inclination leads to a maximum rotation velocity too high with respect to its magnitude and its optical radius. The distance of this nearby galaxy is not accurately determined, but even if the distance is underestimated by a factor two, the kinematical inclination is still too low. Thus the inclination has been set to the morphological value.

UGC 2082. Using the rule defined in Paper VI, we have not plotted the rotation curve of this edge-on galaxy. The maximum rotation velocity may be not reached.

UGC 2141. The signature of a strong bar is clearly visible in the velocity field. It is almost aligned with the major axis and may explain the difference between the value of major axis position angle found in this study and that published in Paper IV (7°). The major axis position angle probably changes with radius within the optical limits for this galaxy. Because of the resulting uncertainty on the major axis position angle, the maximum rotation velocity of that galaxy has been determined directly from its velocity field.

UGC 2183. The inclination computed here ($41 \pm 10^\circ$) is similar to the morphological one (47°) but quite different from that found in HI by Swaters (1999) and adopted in Paper IV (62°). The value 90° suggested by Noordermeer et al. (2005) from optical measurements does not seem realistic.

UGC 2455. The velocity field of this faint low surface brightness galaxy shows a small amplitude making difficult the determination of the rotation curve which is, moreover, affected by a strong bar.

UGC 3013. The determination of the morphological position angle is biased by a strong bar and spiral arms.

UGC 3382. This galaxy has been published in Paper VI from data coming only from run 13. Nevertheless, this galaxy was already observed in run 5 but never published because the signal-to-noise ratio was too low. In this paper, the data from both runs have been added, leading to higher signal-to-noise ratio data and smaller bins allowing a refinement in the kinematical parameters.

UGC 3429. The nucleus of the galaxy is probably hidden behind a dust lane, so that its true position is hard to find on the continuum images because of strong absorption. Thus, we use the center making the central part of the rotation curve most symmetric. This leads to a satisfactory position for the rotation center on the continuum image when assuming that the dust lane is symmetrical with respect to the major axis. Beyond $65''$, the rotation curve is unsure, due to obvious strong non circular motions in the velocity field of this postmerger candidate (Marcum et al. 2001).

UGC 3574. With respect to Paper I, the inclination has been reduced from 30 to $19 \pm 10^\circ$, this new value is more compatible with the morphological one (21°) but leads to a very high maximum rotation velocity with respect to its faint absolute magnitude ($M_B = -18.0$, James et al. 2004). For this nearby object ($V_{sys} = 1433 \text{ km s}^{-1}$), the distance determined using the Hubble relationship (corrected from Virgo infall) is nevertheless unsure, as can be also suspected from its maximal H α extension reaching ~ 2.5 its optical radius.

UGC 3851. The ghost on the data (located on the northern side of the image) has been removed. No rotation curve has been computed because of its high inclination and to the fact that the velocity field corresponding to the very bright region south of the galaxy may be an artefact due to the detector.

UGC 4273. The determination of the morphological position angle is biased by the bar and spiral arms.

UGC 4278. No rotation curve has been computed because of its high inclination (90°).

UGC 4284. The rotation curve is more symmetrical using a kinematical center $5''$ south from the morphological center. However, to have a consistent analysis with the rest of the sample, we decided to keep the morphological center.

UGC 4305. The center has been changed from Paper III, and is now more to the East. It has been determined from a 2MASS image in the infrared. This center still gives a fairly symmetric rotation curve. It coincides approximately with the HI kinematical center but absolutely not with the optical center of isophotes. The counter rotation seen in the rotation curve of Paper III is not seen anymore in the new rotation curve due to the new center. However peculiar motions are still seen in the velocity field near the optical center of isophotes. Depending on the center chosen for kinematical analysis, they can be interpreted as non regular motions or as a counter rotation.

UGC 4499. The inclination has been set to the value computed by Swaters et al. (2003).

UGC 4543. The morphological position angle of this galaxy is difficult to estimate due to its “Magellanic” structure.

UGC 4936. The inclination found now is 17° lower than the one published in Paper III. This value is more compatible with the absolute magnitude of the galaxy as well as its optical radius.

UGC 5272. The position-velocity diagram displays a solid body structure characteristic of a bar like structure or an edge-on galaxy. The optical and H α images both look like a bar rather than a disk galaxy, suggesting a morphological inclination close to 90° . Thus no rotation curve has been plotted. The HI inclination is 59° , computed from a different major axis position angle (20°), this is an additional argument in favour of the bar-like structure seen in the H α image.

UGC 5721. The uncommon rotation curve results from the very irregular velocity field perturbed by a strong bar.

UGC 5931. The morphological position angle of this galaxy is difficult to estimate due to the interaction with its close companion UGC 5935.

UGC 5935. No rotation curve has been computed because of its high inclination, close to 90° .

UGC 6537. The rotation center has been assumed to be the strong nucleus, leading to an asymmetric rotation curve in the outer regions, compatible with the asymmetric velocity field. In Paper III, in order to get a symmetric rotation curve, the rotation center had been shifted by $7''$ (~ 0.5 kpc) with respect to the nucleus, and the major axis position angle rotated by 6° .

UGC 7278. This galaxy does not show any evidence for rotation. However, a velocity amplitude of about 10 km s^{-1} is observed on its velocity field.

UGC 7524. The velocity field only covers the bar of the

galaxy which is almost aligned with the HI major axis position angle, thus no rotation curve has been plotted. Furthermore, only the central part of this galaxy is seen in our field-of-view.

UGC 7592. This galaxy does not show any evidence for rotation. However, a velocity amplitude of about 25 km s^{-1} is observed on its velocity field.

UGC 10310. The morphological position angle is difficult to estimate due to the nature of this barred Magellanic galaxy.

UGC 10359. The determination of the morphological position angle is biased by a strong bar and spiral arms.

UGC 10445. The presence of a bar and spiral arms make both morphological and kinematical position angles determinations difficult.

UGC 10470. A strong bar in this galaxy biases the determination of the major axis position angle and of the inclination. For the latter we adopted the value suggested by the morphological axis ratio (34° from the NED).

UGC 10502. The kinematical inclination is much higher than the morphological one (24° from the axis ratio). Since this galaxy is interacting, its morphological inclination may be underestimated because of its open spiral arms distorted by streaming motions. The average morphological inclination given in Hyperleda is instead 40° , still lower than the kinematical one.

UGC 10897. The morphological position angle is poorly determined for this low inclination galaxy.

UGC 11124. The inclination is difficult to determine because of a strong bar in this interacting galaxy. The kinematical inclination (51°) is higher than the morphological one determined from the axis ratio (22°). Despite the fact that the external isocontours seem almost round, the luminosity of this galaxy is nevertheless more consistent with a high inclination than with a lower one with respect to its rotation velocity.

UGC 11283. The presence of a strong bar and spiral arms make both morphological and kinematical position angle determinations difficult.

UGC 11429. The very peculiar velocity field of this galaxy, which is in pair, displays a concave curvature towards the South on both sides of the galaxy. Thus, the residual velocity field shows a very high dispersion and a signature typical of a rotation curve having a rotation center abnormally displaced toward the South on the major axis (van der Kruit & Allen 1978). This is obviously not the case from the morphology.

UGC 11861. The morphological position angle of this galaxy is difficult to estimate due to its “Magellanic” structure.

UGC 11909. No rotation curve has been computed because of its high inclination (90°).

UGC 11951. The rotation curve published in Paper II is incorrect due to a typo in the value of the position angle of the major axis.

UGC 12060. This galaxy is irregular, barred and has a low surface brightness. These features make the morphological position angle determination difficult.

UGC 12276. The previous data reduction (Paper IV) missed a large part of the velocity field.

UGC 12276c. The total H α diameter of the galaxy ($\sim 8''$) is not much larger than the seeing spot of the observations

($\sim 5''$). Thus no rotation curve has been computed.

UGC 12632. The very high velocity bump on the blue side of the H α rotation curve is also visible in the HI data (Swaters 1999).

Table B1. Calibration parameters.

N $^{\circ}$ UGC (1)	N $^{\circ}$ NGC (2)	α (2000) (3)	δ (2000) (4)	Exposure time <i>s</i> (5)	Scale " (6)	Flux $10^{-16} W m^{-2}$ (7)	Paper (8)
12893		00 ^h 00 ^m 28.0 ^s	17°13'09"	8640	0.68	0.3±0.1	VI
89	0023	00 ^h 09 ^m 53.4 ^s	25°55'24"	8640	0.68	3.3±0.4	VI
94	0026	00 ^h 10 ^m 25.9 ^s	25°49'54"	6240	0.68	2.2±0.3	VI
508	0266	00 ^h 49 ^m 47.8 ^s	32°16'40"	9720	0.68	4.8±0.6	IV
528	0278	00 ^h 52 ^m 04.6 ^s	47°33'01"	3600	0.96	75.4±13.1	II
763	0428	01 ^h 12 ^m 55.7 ^s	00°58'53"	4680	0.68	27.8±3.3	IV
1013	0536	01 ^h 26 ^m 21.9 ^s	34°42'11"	3840	0.68		VI
	0542	01 ^h 26 ^m 30.9 ^s	34°40'31"	3840	0.68	0.5±0.1	VI
1117	0598	01 ^h 33 ^m 51.0 ^s	30°39'35"	5760	0.68	≥97.6±11.6	IV
1249		01 ^h 47 ^m 29.9 ^s	27°19'60"	6000	0.96	≥17.8±3.1	II
1256	0672	01 ^h 47 ^m 54.7 ^s	27°25'57"	11040	0.96	≥25.9±4.5	II
1317	0697	01 ^h 51 ^m 17.6 ^s	22°21'28"	4800	0.68	8.3±1.0	VI
1437	0753	01 ^h 57 ^m 42.2 ^s	35°54'58"	6720	0.68	7.9±0.9	VI
1655	0828	02 ^h 10 ^m 09.7 ^s	39°11'25"	12720	0.68	0.3±0.1	VI
1736	0864	02 ^h 15 ^m 27.7 ^s	06°00'08"	7560	0.68	6.2±0.7	IV
1810		02 ^h 21 ^m 28.7 ^s	39°22'32"	7200	0.68	2.1±0.2	VI
1886		02 ^h 26 ^m 00.6 ^s	39°28'15"	6120	0.68	3.2±0.4	IV
1913	0925	02 ^h 27 ^m 17.3 ^s	33°34'44"	3960	0.68	≥44.9±5.3	IV
2023		02 ^h 33 ^m 18.5 ^s	33°29'30"	14160	0.96	3.9±0.7	II
2034		02 ^h 33 ^m 42.9 ^s	40°31'41"	15840	0.96	1.5±0.3	I
2045	0972	02 ^h 34 ^m 13.4 ^s	29°18'40"	6120	0.68	22.4±2.7	IV
2053		02 ^h 34 ^m 29.3 ^s	29°44'60"	9120	0.96	0.3±0.1	II
2082		02 ^h 36 ^m 16.2 ^s	25°25'25"	7200	0.96	4.0±0.7	II
2080		02 ^h 36 ^m 27.9 ^s	38°58'09"	21840	0.96	12.9±2.2	I
2141	1012	02 ^h 39 ^m 14.9 ^s	30°09'04"	5040	0.68	23.0±2.7	IV
2183	1056	02 ^h 42 ^m 48.3 ^s	28°34'27"	5760	0.68	3.4±0.4	IV
2193	1058	02 ^h 43 ^m 30.1 ^s	37°20'28"	7920	0.68	6.5±0.8	IV
2455	1156	02 ^h 59 ^m 42.3 ^s	25°14'13"	3840	0.96	32.2±5.6	I
2503	1169	03 ^h 03 ^m 34.8 ^s	46°23'10"	7200	0.68	4.5±0.5	IV
2800		03 ^h 40 ^m 03.6 ^s	71°24'19"	8880	0.96	2.0±0.4	I
2855		03 ^h 48 ^m 20.7 ^s	70°07'57"	7200	0.96	25.0±4.3	II
3013	1530	04 ^h 23 ^m 26.7 ^s	75°17'44"	3360	0.68	4.8±0.6	IV
3056	1569	04 ^h 30 ^m 49.2 ^s	64°50'52"	6000	0.68	270.5±32.0	VI
3273		05 ^h 17 ^m 45.1 ^s	53°33'01"	4800	0.68	3.6±0.4	IV
3334	1961	05 ^h 42 ^m 04.6 ^s	69°22'43"	5040	0.68	20.2±2.4	VI
3382		05 ^h 59 ^m 47.7 ^s	62°09'28"	19200	0.68	0.4±0.1	VI
3384		06 ^h 01 ^m 37.2 ^s	73°07'01"	4320	0.68	1.4±0.2	IV
3429	2146	06 ^h 18 ^m 38.4 ^s	78°21'26"	6480	0.68	30.7±3.6	IV
3463		06 ^h 26 ^m 55.8 ^s	59°04'47"	6960	0.68	11.1±1.3	VI
3574		06 ^h 53 ^m 10.4 ^s	57°10'40"	10080	0.96	≥8.7±1.5	I
3521		06 ^h 55 ^m 00.1 ^s	84°02'30"	8400	0.68	0.7±0.1	VI
3528		06 ^h 56 ^m 10.6 ^s	84°04'44"	8400	0.68	0.3±0.1	VI
3618	2308	06 ^h 58 ^m 37.6 ^s	45°12'38"	6000	0.68		VI
3691		07 ^h 08 ^m 01.4 ^s	15°10'39"	3960	0.68	12.2±1.4	IV
3685		07 ^h 09 ^m 05.9 ^s	61°35'44"	5520	0.68	8.0±0.9	VI
3708	2341	07 ^h 09 ^m 12.0 ^s	20°36'11"	6480	0.68	1.2±0.1	VI
3709	2342	07 ^h 09 ^m 18.1 ^s	20°38'10"	6480	0.68	4.2±0.5	VI
3734	2344	07 ^h 12 ^m 28.7 ^s	47°10'00"	11040	0.68	≥3.7±0.4	IV
3826		07 ^h 24 ^m 28.0 ^s	61°41'38"	4560	0.68	4.0±0.5	VI
3809	2336	07 ^h 27 ^m 03.9 ^s	80°10'42"	9120	0.96	≥25.4±4.4	III
3740	2276	07 ^h 27 ^m 13.1 ^s	85°45'16"	4800	0.68	63.8±7.6	VI
3851	2366	07 ^h 28 ^m 51.9 ^s	69°12'31"	7200	0.96	≥128.5±22.3	III
3876		07 ^h 29 ^m 17.5 ^s	27°54'00"	15600	0.68	1.5±0.2	VI
3915		07 ^h 34 ^m 55.8 ^s	31°16'34"	6000	0.68	9.3±1.1	VI
IC476		07 ^h 47 ^m 16.5 ^s	26°57'03"	6240	0.68	0.2±0.1	VI
4026	2449	07 ^h 47 ^m 20.4 ^s	26°55'48"	6240	0.68	0.5±0.1	VI
4165	2500	08 ^h 01 ^m 53.2 ^s	50°44'15"	9600	0.68	13.6±1.6	VI
4256	2532	08 ^h 10 ^m 15.2 ^s	33°57'24"	6960	0.68	2.9±0.3	VI
4273	2543	08 ^h 12 ^m 57.9 ^s	36°15'16"	6240	0.68	9.0±1.1	IV
4274	2537	08 ^h 13 ^m 14.9 ^s	45°59'31"	2640	0.96	15.3±2.7	III

Table B1 – *continued*

N° UGC (1)	N° NGC (2)	α (2000) (3)	δ (2000) (4)	Exposure time <i>s</i> (5)	Scale " (6)	Flux $10^{-16} W m^{-2}$ (7)	Paper (8)
4278		08 ^h 13 ^m 58.9 ^s	45° 44' 37"	7200	0.96	≥14.9±2.6	III
4284	2541	08 ^h 14 ^m 40.2 ^s	49° 03' 42"	7440	0.96	≥34.0±5.9	III
4305		08 ^h 19 ^m 18.4 ^s	70° 43' 03"	6240	0.96	≥94.2±16.4	III
4325	2552	08 ^h 19 ^m 20.0 ^s	50° 00' 31"	6240	0.96	3.8±0.7	I
4393		08 ^h 26 ^m 04.4 ^s	45° 58' 02"	6960	0.68	5.4±0.6	VI
4422	2595	08 ^h 27 ^m 42.0 ^s	21° 28' 45"	7200	0.68	3.2±0.4	VI
4456		08 ^h 32 ^m 03.5 ^s	24° 00' 39"	6720	0.68	2.0±0.2	VI
4499		08 ^h 37 ^m 41.5 ^s	51° 39' 10"	10560	0.96	3.5±0.6	I
4543		08 ^h 43 ^m 21.4 ^s	45° 44' 10"	13680	0.96	2.8±0.5	III
4555	2649	08 ^h 44 ^m 08.4 ^s	34° 43' 02"	6960	0.68	1.5±0.2	VI
4770	2746	09 ^h 05 ^m 59.4 ^s	35° 22' 38"	7920	0.68	0.6±0.1	VI
4820	2775	09 ^h 10 ^m 20.1 ^s	07° 02' 17"	8400	0.68	9.5±1.1	VI
4936	2805	09 ^h 20 ^m 20.4 ^s	64° 06' 10"	6960	0.96	16.6±2.9	III
5045		09 ^h 28 ^m 10.2 ^s	44° 39' 52"	6960	0.68	3.5±0.4	VI
5175	2977	09 ^h 43 ^m 46.8 ^s	74° 51' 35"	5520	0.68	5.2±0.6	VI
5228		09 ^h 46 ^m 03.8 ^s	01° 40' 06"	9120	0.68	7.3±0.9	VI
5251	3003	09 ^h 48 ^m 36.4 ^s	33° 25' 17"	1680	0.68	23.1±2.7	VI
5253	2985	09 ^h 50 ^m 21.9 ^s	72° 16' 47"	6960	0.96	9.5±1.7	I
5272		09 ^h 50 ^m 22.4 ^s	31° 29' 16"	8160	0.96	6.9±1.2	III
5279	3026	09 ^h 50 ^m 55.3 ^s	28° 33' 04"	6000	0.68	5.0±0.6	VI
5316	3027	09 ^h 55 ^m 40.4 ^s	72° 12' 13"	6240	0.96	8.7±1.5	I
5319	3061	09 ^h 56 ^m 12.0 ^s	75° 51' 59"	7200	0.68	3.2±0.4	VI
5351	3067	09 ^h 58 ^m 21.2 ^s	32° 22' 12"	7200	0.68	8.2±1.0	VI
5373		10 ^h 00 ^m 00.5 ^s	05° 19' 58"	7680	0.68	6.0±0.7	VI
5398	3077	10 ^h 03 ^m 20.0 ^s	68° 44' 01"	7920	0.68	20.9±2.5	VI
5414	3104	10 ^h 03 ^m 57.1 ^s	40° 45' 21"	7200	0.96	11.8±2.1	III
IC2542		10 ^h 07 ^m 50.5 ^s	34° 18' 55"	7440	0.68	1.6±0.2	VI
5510	3162	10 ^h 13 ^m 31.7 ^s	22° 44' 14"	6240	0.68	18.9±2.2	VI
5532	3147	10 ^h 16 ^m 53.5 ^s	73° 24' 03"	6480	0.68	27.8±3.3	VI
5556	3187	10 ^h 17 ^m 47.9 ^s	21° 52' 24"	5760	0.68	3.2±0.4	VI
5721	3274	10 ^h 32 ^m 16.9 ^s	27° 40' 08"	8160	0.96	5.3±0.9	I
5786	3310	10 ^h 38 ^m 45.9 ^s	53° 30' 12"	4080	0.68	183.5±21.7	VI
5789	3319	10 ^h 39 ^m 09.4 ^s	41° 41' 11"	6300	0.96	≥16.0±2.8	I
5829		10 ^h 42 ^m 43.7 ^s	34° 26' 54"	11760	0.96	≥3.3±0.6	I
5840	3344	10 ^h 43 ^m 31.1 ^s	24° 55' 21"	5760	0.68	≥60.4±7.2	VI
5842	3346	10 ^h 43 ^m 39.0 ^s	14° 52' 18"	6000	0.68	9.9±1.2	VI
5931	3395	10 ^h 49 ^m 50.2 ^s	32° 58' 59"	10320	0.96	10.5±1.8	I
5935	3396	10 ^h 49 ^m 55.2 ^s	32° 59' 27"	10320	0.96	10.2±1.8	I
5982	3430	10 ^h 52 ^m 11.5 ^s	32° 56' 59"	10080	0.96	8.3±1.4	I
6118	3504	11 ^h 03 ^m 11.3 ^s	27° 58' 20"	5760	0.68	27.4±3.2	VI
6277	3596	11 ^h 15 ^m 06.2 ^s	14° 47' 12"	10320	0.68	9.4±1.1	VI
6419	3664	11 ^h 24 ^m 24.6 ^s	03° 19' 36"	6960	0.68	12.2±1.4	VI
6521	3719	11 ^h 32 ^m 13.4 ^s	00° 49' 09"	6960	0.68	3.6±0.4	VI
6523	3720	11 ^h 32 ^m 21.6 ^s	00° 48' 14"	6960	0.68	1.4±0.2	VI
6537	3726	11 ^h 33 ^m 21.2 ^s	47° 01' 45"	6240	0.96	≥73.8±12.8	III
6628		11 ^h 40 ^m 05.7 ^s	45° 56' 33"	5760	0.96	7.9±1.4	III
6702	3840	11 ^h 43 ^m 59.0 ^s	20° 04' 37"	5280	0.68	2.9±0.3	IV
6778	3893	11 ^h 48 ^m 38.4 ^s	48° 42' 38"	10080	0.96	18.4±3.2	I
6787	3898	11 ^h 49 ^m 15.6 ^s	56° 05' 04"	9360	0.68	2.0±0.2	VI
7021	4045	12 ^h 02 ^m 42.3 ^s	01° 58' 36"	7200	0.68	4.6±0.5	VI
7045	4062	12 ^h 04 ^m 03.8 ^s	31° 53' 42"	6000	0.68	13.8±1.6	VI
7154	4145	12 ^h 10 ^m 01.4 ^s	39° 53' 02"	5520	0.68	30.3±3.6	VI
7278	4214	12 ^h 15 ^m 39.1 ^s	36° 19' 41"	5040	0.96	142.4±24.8	III
7323	4242	12 ^h 17 ^m 30.2 ^s	45° 37' 12"	7200	0.96	18.5±3.2	III
7429	4319	12 ^h 21 ^m 43.1 ^s	75° 19' 22"	6960	0.68	0.1±0.1	VI
7524	4395	12 ^h 25 ^m 48.9 ^s	33° 32' 48"	8400	0.96	≥17.7±3.1	I
7592	4449	12 ^h 28 ^m 10.9 ^s	44° 05' 33"	2880	0.96	429.6±74.7	III
7699		12 ^h 32 ^m 48.1 ^s	37° 37' 20"	6720	0.68	8.3±1.0	VI
7766	4559	12 ^h 35 ^m 57.3 ^s	27° 57' 38"	2400	0.68	≥50.4±6.0	VI
7831	4605	12 ^h 39 ^m 59.7 ^s	61° 36' 29"	3840	0.68	62.1±7.4	VI

Table B1 – *continued*

N $^{\circ}$ UGC (1)	N $^{\circ}$ NGC (2)	α (2000) (3)	δ (2000) (4)	Exposure time <i>s</i> (5)	Scale " (6)	Flux $10^{-16} W m^{-2}$ (7)	Paper (8)
7853	4618	12 ^h 41 ^m 33.1 ^s	41°09'05"	5040	0.68	49.8±5.9	VI
7861	4625	12 ^h 41 ^m 52.9 ^s	41°16'25"	3840	0.68	6.3±0.7	VI
7876	4635	12 ^h 42 ^m 39.3 ^s	19°56'44"	6720	0.68	4.1±0.5	VI
7901	4651	12 ^h 43 ^m 42.7 ^s	16°23'35"	8160	0.68	12.7±1.5	VI
7971	4707	12 ^h 48 ^m 22.9 ^s	51°09'57"	13200	0.96	0.8±0.1	I
7985	4713	12 ^h 49 ^m 57.9 ^s	05°18'42"	6240	0.68	28.6±3.4	VI
8334	5055	13 ^h 15 ^m 49.4 ^s	42°01'46"	4320	0.68	≥88.2±10.4	VI
8403	5112	13 ^h 21 ^m 56.6 ^s	38°44'05"	4080	0.68	30.5±3.6	VI
8490	5204	13 ^h 29 ^m 36.5 ^s	58°25'09"	13920	0.96	≥16.2±2.8	I
	5296	13 ^h 46 ^m 18.7 ^s	43°51'04"	6000	0.68	0.8±0.1	VI
8709	5297	13 ^h 46 ^m 23.7 ^s	43°52'20"	6000	0.68	15.2±1.8	VI
8852	5376	13 ^h 55 ^m 16.1 ^s	59°30'25"	7680	0.68	4.4±0.5	VI
8863	5377	13 ^h 56 ^m 16.7 ^s	47°14'08"	5040	0.68	0.4±0.1	VI
8898	5394	13 ^h 58 ^m 33.7 ^s	37°27'12"	4320	0.68	1.0±0.1	VI
8900	5395	13 ^h 58 ^m 38.0 ^s	37°25'28"	4320	0.68	5.6±0.7	VI
8937	5430	14 ^h 00 ^m 45.8 ^s	59°19'43"	8880	0.68	10.7±1.3	VI
9013	5474	14 ^h 05 ^m 02.0 ^s	53°39'08"	5040	0.68	≥18.8±2.2	VI
9179	5585	14 ^h 19 ^m 48.1 ^s	56°43'45"	8160	0.68	12.5±1.5	VI
9219	5608	14 ^h 23 ^m 17.5 ^s	41°46'34"	6480	0.68	2.9±0.3	VI
9248	5622	14 ^h 26 ^m 12.2 ^s	48°33'51"	10800	0.68	1.8±0.2	VI
9358	5678	14 ^h 32 ^m 05.6 ^s	57°55'16"	7680	0.68	8.8±1.0	VI
9366	5676	14 ^h 32 ^m 46.8 ^s	49°27'29"	5040	0.68	34.7±4.1	IV
9363	5668	14 ^h 33 ^m 24.4 ^s	04°27'02"	8160	0.68	≥21.5±2.5	VI
9406	5693	14 ^h 36 ^m 11.1 ^s	48°35'06"	6000	0.68	0.9±0.1	VI
9465	5727	14 ^h 40 ^m 26.1 ^s	33°59'23"	6480	0.68	4.2±0.5	VI
9576	5774	14 ^h 53 ^m 42.5 ^s	03°34'57"	6840	0.68	11.3±1.3	VI
9649	5832	14 ^h 57 ^m 46.2 ^s	71°40'53"	5520	0.68	3.9±0.5	IV
9736	5874	15 ^h 07 ^m 51.9 ^s	54°45'08"	3840	0.68	2.8±0.3	VI
9753	5879	15 ^h 09 ^m 46.8 ^s	57°00'01"	5040	0.68	18.7±2.2	IV
9858		15 ^h 26 ^m 41.6 ^s	40°33'53"	5280	0.68	6.9±0.8	IV
9866	5949	15 ^h 28 ^m 00.6 ^s	64°45'46"	5280	0.68	7.2±0.9	VI
9943	5970	15 ^h 38 ^m 30.0 ^s	12°11'11"	8400	0.68	16.0±1.9	VI
9969	5985	15 ^h 39 ^m 37.2 ^s	59°19'54"	18840	0.96	12.3±2.1	I
9992		15 ^h 41 ^m 47.9 ^s	67°15'14"	5760	0.68	0.5±0.1	IV
10075	6015	15 ^h 51 ^m 25.3 ^s	62°18'36"	5760	0.68	27.1±3.2	VI
10310		16 ^h 16 ^m 18.5 ^s	47°02'45"	12340	0.96	1.8±0.3	I
10359	6140	16 ^h 20 ^m 56.9 ^s	65°23'23"	4560	0.68	≥17.9±2.1	IV
10470	6217	16 ^h 32 ^m 39.1 ^s	78°11'53"	7920	0.68	35.9±4.2	IV
10445		16 ^h 33 ^m 47.7 ^s	28°59'05"	4320	0.68	8.7±1.0	IV
10502		16 ^h 37 ^m 37.8 ^s	72°22'26"	3120	0.68	6.9±0.8	IV
10521	6207	16 ^h 43 ^m 03.7 ^s	36°49'55"	7680	0.68	10.3±1.2	VI
10546	6236	16 ^h 44 ^m 34.4 ^s	70°46'47"	5280	0.68	13.0±1.5	IV
10564	6237	16 ^h 46 ^m 22.5 ^s	70°21'20"	4560	0.68	6.9±0.8	IV
10652	6283	16 ^h 59 ^m 26.5 ^s	49°55'20"	6000	0.68	6.4±0.8	VI
10713		17 ^h 04 ^m 33.7 ^s	72°26'44"	5040	0.68	1.9±0.2	VI
10757		17 ^h 10 ^m 13.4 ^s	72°24'38"	5280	0.68	2.8±0.3	VI
10769		17 ^h 11 ^m 33.5 ^s	72°24'07"	5280	0.68	0.1±0.1	VI
10791		17 ^h 14 ^m 38.5 ^s	72°23'56"	6000	0.68	0.0±0.1	VI
10897	6412	17 ^h 29 ^m 37.5 ^s	75°42'16"	6960	0.96	16.3±2.8	II
11012	6503	17 ^h 49 ^m 26.3 ^s	70°08'40"	5040	0.68	25.3±3.0	VI
11124		18 ^h 07 ^m 27.6 ^s	35°33'51"	3600	0.68	8.4±1.0	IV
11218	6643	18 ^h 19 ^m 46.7 ^s	74°34'06"	7200	0.96	42.2±7.3	II
11269	6667	18 ^h 30 ^m 39.7 ^s	67°59'14"	3840	0.68	1.1±0.1	VI
11283		18 ^h 33 ^m 52.4 ^s	49°16'41"	8640	0.96	10.4±1.8	II
11283c		18 ^h 34 ^m 00.7 ^s	49°22'21"	7200	0.96	0.6±0.1	II
11300	6689	18 ^h 34 ^m 49.9 ^s	70°31'27"	17520	0.96	≥9.3±1.6	II IV VI
11332	6654A	18 ^h 39 ^m 25.2 ^s	73°34'48"	7200	0.68	15.6±1.8	VI
11407	6764	19 ^h 08 ^m 16.4 ^s	50°55'59"	6480	0.68	6.6±0.8	VI
11429	6792	19 ^h 20 ^m 57.4 ^s	43°07'57"	6000	0.68	4.4±0.5	IV
11466		19 ^h 42 ^m 59.1 ^s	45°17'58"	5040	0.68	14.2±1.7	VI

Table B1 – *continued*

N° UGC (1)	N° NGC (2)	α (2000) (3)	δ (2000) (4)	Exposure time <i>s</i> (5)	Scale " (6)	Flux $10^{-16} W m^{-2}$ (7)	Paper (8)
11470	6824	19 ^h 43 ^m 40.8 ^s	56°06'34"	3600	0.68	2.9±0.3	VI
11496		19 ^h 53 ^m 01.8 ^s	67°39'54"	5520	0.68	0.9±0.1	VI
11498		19 ^h 57 ^m 15.1 ^s	05°53'24"	8400	0.68	1.9±0.2	VI
11557		20 ^h 24 ^m 00.7 ^s	60°11'41"	4320	0.68	10.0±1.2	IV
11597	6946	20 ^h 34 ^m 52.5 ^s	60°09'12"	5280	0.68	≥103.2±12.2	VI
11670	7013	21 ^h 03 ^m 33.7 ^s	29°53'50"	7440	0.68	2.9±0.3	VI
11707		21 ^h 14 ^m 31.8 ^s	26°44'05"	4320	0.68	6.9±0.8	IV
11852		21 ^h 55 ^m 59.4 ^s	27°53'53"	6480	0.68	0.6±0.1	IV
11861		21 ^h 56 ^m 24.2 ^s	73°15'39"	4800	0.68	9.5±1.1	IV
11872	7177	22 ^h 00 ^m 41.2 ^s	17°44'18"	7200	0.68	6.3±0.7	VI
11891		22 ^h 03 ^m 33.8 ^s	43°44'57"	10560	0.96	0.6±0.1	II
11909		<i>22^h06^m16.4^s</i>	<i>47°15'10"</i>	4320	0.68	13.8±1.6	IV
11914	7217	22 ^h 07 ^m 52.5 ^s	31°21'32"	6120	0.68	20.2±2.4	IV
11951	7231	22 ^h 12 ^m 30.2 ^s	45°19'42"	7200	0.96	14.7±2.6	II
12060		22 ^h 30 ^m 34.0 ^s	33°49'09"	18000	0.96	4.1±0.7	I
12082		22 ^h 34 ^m 11.3 ^s	32°51'42"	7440	0.68	1.3±0.2	VI
12101	7320	22 ^h 36 ^m 03.5 ^s	33°56'52"	4680	0.68	2.3±0.3	IV
12212		22 ^h 50 ^m 30.6 ^s	29°08'20"	9360	0.96	1.0±0.2	II
12276	7440	22 ^h 58 ^m 32.6 ^s	35°48'08"	4680	0.68	3.1±0.4	IV
12276c		<i>22^h58^m41.4^s</i>	<i>35°48'33"</i>	4680	0.68	0.2±0.1	IV
12343	7479	23 ^h 04 ^m 56.7 ^s	12°19'21"	5520	0.68	31.0±3.7	IV
12632		23 ^h 29 ^m 58.7 ^s	40°59'25"	5760	0.68	3.4±0.4	IV
12754	7741	23 ^h 43 ^m 54.4 ^s	26°04'31"	10800	0.96	≥44.1±7.7	I

(1) Name of the galaxy in the UGC catalog except for NGC 542, IC 476, IC 2542 and NGC 5296 that do not have UGC name. (2) Name in the NGC catalog when available. (3&4) Coordinates (in 2000) of the center of the galaxy used for the kinematic study except those in *italic* (taken from HyperLeda). (5) Total exposure time in second. (6) Pixel scale in arcsec. (7) Flux deduced from the comparison with James et al. (2004) data. When the galaxy is larger than the field-of-view (see Table B3), we only have a lower limit on the integrated H α flux. (8) Publication papers.

Table B2. Model parameters.

N $^{\circ}$ UGC (1)	V_{sys_Leda} km s $^{-1}$ (2)	V_{sys_FP} km s $^{-1}$ (3)	i_{Morph} $^{\circ}$ (4)	i_{Kin} $^{\circ}$ (5)	P.A. $_{Morph}$ $^{\circ}$ (6)	P.A. $_{Kin}$ $^{\circ}$ (7)	\overline{Res} 10 $^{-3}$ km s $^{-1}$ (8)	σ_{res} km s $^{-1}$ (9)	χ^2_{red} (10)
12893	1102 \pm 7	1097 \pm 2	30 \pm 8	19 \pm 19	95 \pm 90	77 $^{\#}$ \pm 5	-28.1	8	1.2
89	4564 \pm 3	4510 \pm 5	40 \pm 4	33 \pm 13	174 \pm 37	177 \pm 4	42.5	23	8.6
94	4592 \pm 4	4548 \pm 2	50 \pm 4	42 \pm 5	102 \pm 22	94 \pm 2	-3.9	13	2.7
508	4665 \pm 4	4641 \pm 2	15 \pm 27	25 \pm 7*	95 2M \pm 90	123 \pm 2	-0.2	24	8.7
528	639 \pm 7	628 \pm 1	14 \pm 22	21 \pm 14	50 $^{2M}/30^{H\alpha}$ \pm 90	52 \pm 3	0.6	9	1.3
763	1156 \pm 4	1148 \pm 2	48 \pm 5	54 \pm 6	112 \pm 26	117 \pm 3	-0.4	12	2.3
1013	5190 \pm 4		80 \pm 3		68 \pm 7				
NGC 542	4660 \pm 8		90 \pm 0		143 \pm 8				
1117	-182 \pm 3	-191 \pm 1	56 \pm 5	56 \pm 16*	23 \pm 11	18 $^{\#}$ \pm 3	2.1	9	1.4
1249	340 \pm 14		90 \pm 0		150 \pm 8				
1256	424 \pm 6	428 \pm 1	70 \pm 2	76 \pm 2	66 \pm 9	73 \pm 2	1.0	13	2.5
1317	3111 \pm 5	3090 \pm 2	75 \pm 4	73 \pm 1	105 \pm 8	106 \pm 1	-1.3	15	3.3
1437	4893 \pm 4	4858 \pm 2	52 \pm 3	47 \pm 4	134 \pm 26	127 $^{\#}$ \pm 2	-0.8	18	5.2
1655	5340 \pm 16	5427 \pm 7	45 \pm 9	45 \pm 18*		138 $^{\#}$ \pm 6	-2744.9	30	15.4
1736	1561 \pm 2	1522 \pm 2	48 \pm 3	35 \pm 14	24 \pm 21	27 \pm 3	-6.5	18	5.1
1810	7556 \pm 21		75 \pm 3		42 \pm 9				
1886	4859 \pm 23	4836 \pm 3	47 \pm 5	62 \pm 2	52 \pm 40	35 \pm 2	0.8	19	5.9
1913	554 \pm 4	536 \pm 2	59 \pm 3	48 \pm 9	102 \pm 11	108 $^{\#}$ \pm 3	-12.7	12	2.2
2023	604 \pm 6	593 \pm 2	15 \pm 30	19 \pm 18*		135 $^{\#}$ \pm 9*	<0.1	7	0.7
2034	579 \pm 6	567 \pm 2	37 \pm 12	19 \pm 23*	170 \pm 57	162 $^{\#}$ \pm 17*	-0.3	8	1.0
2045	1546 \pm 3	1525 \pm 3	66 \pm 4	61 \pm 8	151 \pm 14	139 $^{\#}$ \pm 4	-3.7	17	4.4
2053	1026 \pm 5		66 \pm 9		43 \pm 23				
2082	707 \pm 3		87 \pm 4		133 \pm 3				
2080	903 \pm 5	893 \pm 1	25 \pm 12	25 \pm 9*	75 2M \pm 85	156 $^{\#}$ \pm 2	-0.1	10	1.5
2141	985 \pm 4	965 \pm 3	68 \pm 5	74 \pm 23	23 \pm 14	11 $^{\#}$ \pm 5	-11.6	11	1.9
2183	1546 \pm 7	1475 \pm 4	47 \pm 11	41 \pm 10	160 \pm 50	159 \pm 3	-2.0	12	2.1
2193	517 \pm 6	519 \pm 1	58 \pm 3	6 \pm 15	100 \pm 14	125 $^{\#}$ \pm 6	<0.1	8	1.0
2455	374 \pm 2	367 \pm 2	43 \pm 7	51 \pm 30*	25 \pm 28	83 $^{\#}$ \pm 21*			
2503	2387 \pm 4	2377 \pm 2	57 \pm 3	49 \pm 2	31 \pm 16	34 \pm 1	-8.4	16	3.8
2800	1174 \pm 5	1174 \pm 2	73 \pm 7	52 \pm 13	103 \pm 19	111 $^{\#}$ \pm 4	0.9	12	2.2
2855	1202 \pm 4	1188 \pm 2	68 \pm 2	68 \pm 2	110 \pm 10	100 \pm 2	-0.6	19	5.4
3013	2468 \pm 14	2453 \pm 6	58 \pm 3	58 \pm 8*	81 \pm 18	15 $^{\#}$ \pm 4	-3.5	25	10.0
3056	-100 \pm 7		65 \pm 7		120 \pm 17				
3273	616 \pm 7	615 \pm 2	90 \pm 0	82 \pm 7	45 \pm 12	42 \pm 4	4.0	12	2.4
3334	3934 \pm 4	3952 \pm 13	47 \pm 7	47 \pm 14*	85 \pm 21	97 $^{\#}$ \pm 6	9.9	54	46.0
3382	4497 \pm 6	4490 \pm 2	21 \pm 10	18 \pm 6	30 $^{2M}/168^{Pa}$ \pm 90	4 $^{\#}$ \pm 2	-2.2	18	5.0
3384	1088 \pm 3		45 \pm 7		62 \pm 59				
3429	898 \pm 6	868 \pm 4	37 \pm 12	54 \pm 8	123 \pm 28	137 $^{\#}$ \pm 3	-7.6	17	4.3
3463	2692 \pm 4	2679 \pm 3	63 \pm 3	63 \pm 3	117 \pm 12	110 \pm 2	-0.1	15	3.6
3574	1441 \pm 3	1433 \pm 1	21 \pm 8	19 \pm 10	10 $^{2M}/121^{H\alpha}/162^{Pa}$ \pm 90	99 \pm 3	<0.1	12	2.3
3521	4426 \pm 7	4415 \pm 2	61 \pm 3	58 \pm 5	76 \pm 17	78 $^{\#}$ \pm 3	3.2	16	4.1
3528	4421 \pm 18	4340 \pm 5	59 \pm 5	42 \pm 12	38 \pm 24	43 $^{\#}$ \pm 4	-17.8	32	17.6
3618	5851 \pm 6		49 \pm 5		171 \pm 24				
3691	2202 \pm 4	2203 \pm 2	62 \pm 4	64 \pm 4	65 \pm 19	68 $^{\#}$ \pm 3	<0.1	10	1.7
3685	1796 \pm 4	1795 \pm 1	55 \pm 4	12 \pm 17	133 \pm 18	118 $^{\#}$ \pm 4	-1.3	9	1.4
3708	5201 \pm 26	5161 \pm 4	16 \pm 24	44 \pm 16	136 Ni \pm 90	50 $^{\#}$ \pm 4	-11.6	18	5.4
3709	5223 \pm 50	5292 \pm 4	46 \pm 4	55 \pm 4	66 \pm 27	52 $^{\#}$ \pm 2	-4.7	18	5.3
3734	969 \pm 5	966 \pm 1	26 \pm 7	43 \pm 7	144 \pm 59	139 \pm 2	7.7	12	2.2
3826	1733 \pm 3	1724 \pm 2	30 \pm 9	20 \pm 19	160 $^{2M}/85^{Ni}$ \pm 56	74 $^{\#}$ \pm 5	135.4	9	1.2
3809	2202 \pm 4	2200 \pm 1	58 \pm 4	58 \pm 2	178 \pm 17	177 $^{\#}$ \pm 1	<0.1	14	3.3
3740	2417 \pm 6	2416 \pm 2	40 \pm 6	48 \pm 14	19 \pm 29	67 $^{\#}$ \pm 4	<0.1	11	1.7
3851	99 \pm 2		90 \pm 0		30 \pm 7				
3876	860 \pm 7	854 \pm 2	61 \pm 3	59 \pm 5	178 \pm 14	178 $^{\#}$ \pm 3	-0.2	10	1.6
3915	4679 \pm 7	4659 \pm 3	59 \pm 5	47 \pm 4	25 \pm 26	30 \pm 2	6.8	13	2.7
IC 476	4734 \pm 32	4767 \pm 3	40 \pm 5	55 \pm 24	102 \pm 49	68 \pm 6	-5.9	18	5.5
4026	4782 \pm 11	4892 \pm 3	73 \pm 4	56 \pm 4	136 \pm 12	139 \pm 2	4.0	19	5.7
4165	515 \pm 4	504 \pm 1	21 \pm 9	41 \pm 10	74 Pa \pm 86	85 $^{\#}$ \pm 2	-0.4	10	1.6
4256	5252 \pm 5	5252 \pm 3	36 \pm 4	38 \pm 21	26 \pm 35	111 $^{\#}$ \pm 6	15.9	26	11.1
4273	2458 \pm 18	2398 \pm 2	65 \pm 5	60 \pm 4	54 \pm 15	32 $^{\#}$ \pm 2	-2.3	14	3.3
4274	445 \pm 3	430 \pm 1	69 \pm 6	27 \pm 17		175 \pm 3	<0.1	8	1.1

Table B2 – *continued*

N ^o UGC	V_{sys_Leda} km s ⁻¹	V_{sys_FP} km s ⁻¹	i_{Morph}	i_{Kin}	P.A. _{Morph}	P.A. _{Kin}	\overline{Res} 10 ⁻³ km s ⁻¹	σ_{res} km s ⁻¹	χ^2_{red}
(1)	(2)	(3)	(4)	(5)	(6)	(7)	(8)	(9)	(10)
4278	558±4		90±0		172±3				
4284	559±3	536±2	61±3	59±9	170±14	176±3	0.5	10	1.4
4305	158±2	139±1	51±6	40±27*	15±21	9 [#] ±4			
4325	518±4	508±2	68±4	63±14	52±14	57±3	-0.4	11	2.0
4393	2126±5	2119±4	50±5	50±9*	50±35	70 [#] ±7	0.6	11	1.7
4422	4333±4	4321±2	49±4	25±8	12±26	36±2	-18.3	20	6.2
4456	5497±23	5470±1	28±6	9±14	42±74	124±3	7.3	14	3.1
4499	692±4	682±1	80±6	50±14*	151±13	141±4	0.5	7	0.7
4543	1960±4	1948±2	45±6	52±15	174±36	136 [#] ±4	0.7	14	3.0
4555	4235±6	4235±2	21±12	38±7	140 ^{2M} /78 ^{SDSS} ±90	90±2	0.5	15	3.5
4770	7063±9	7026±3	36±9	20±13	54±48	98 [#] ±3	-36.8	14	3.0
4820	1355±4	1350±2	41±4	38±3	160±23	157±2	<0.1	13	2.7
4936	1733±5	1728±1	36±6	13±12	174±32	114 [#] ±2	0.2	10	1.4
5045	7716±23	7667±2	41±4	16±9	136±31	148±2	-2.8	13	2.7
5175	3052±11	3049±2	65±4	56±3	145±14	143±2	-2.3	13	2.9
5228	1873±7	1869±2	82±2	72±2	122±6	120±2	-0.7	9	1.3
5251	1481±3	1465±3	88±9	73±6	78±4	80 [#] ±3	<0.1	15	3.5
5253	1322±7	1322±2	38±6	40±4	176±31	176 [#] ±2	-0.7	13	2.5
5272	520±3		90±0		118±6				
5279	1488±4		90±0		83±6				
5316	1059±3	1031±2	70±2	77±4	130±9	130±3	-5.4	14	3.2
5319	2448±9	2439±1	40±5	30±9	125 ^{2M} /7 ^{Pa} ±29	165 [#] ±2	-21.0	9	1.3
5351	1473±4		82±6		105±6				
5373	302±3	291±2	60±6	10±18	110±18	51±8	-0.5	8	0.9
5398	14±5		40±10		45±35				
5414	603±3	592±2	54±8	71±13	35±29	39 [#] ±4	-0.4	13	2.7
IC 2542	6113±20	6111±2	43±4	20±15	173±32	174±3	-0.9	20	6.3
5510	1301±3	1298±2	38±5	31±10	26±37	20 [#] ±3	-0.3	10	1.4
5532	2812±8	2802±1	33±9	32±3	150±42	147±1	<0.1	14	2.9
5556	1581±3		75±2		105±7				
5721	537±4	527±6	62±3	62±30*	95±14	95 [#] ±21*	0.2	14	3.1
5786	990±3	992±4	16±25	53±11	18 ^{SDSS} ±90	153±5	0.5	17	4.6
5789	742±2	730±2	63±3	68±10	37±12	27±3	4.0	8	1.1
5829	630±3	626±2	25±13	34±20		18 [#] ±6	-0.5	9	1.2
5840	582±4	580±1	18±14	18±11		153 [#] ±3	<0.1	12	2.1
5842	1261±10	1245±1	34±6	47±9	104±36	112 [#] ±2	-1.5	10	1.7
5931	1621±3	1604±3	58±4	54±16	35±20	180 [#] ±5	10.2	13	2.9
5935	1656±7		90±0		99±14				
5982	1583±6	1573±2	58±4	55±4	33±17	28±2	-1.5	15	3.6
6118	1539±5	1525±2	27±7	39±8*	150 ^{2M} /57 ^{Pa} ±50	163 [#] ±3	16.3	11	1.9
6277	1192±3	1191±3	17±16	17±17*	0 ^{2M} ±90	76±3	-5.1	19	5.7
6419	1365±24	1381±2	57±5	66±19	27±23	34±7	-1.8	8	0.9
6521	5879±5	5842±2	50±3	46±4	21±19	20±2	-0.9	17	4.5
6523	5913±13	5947±2	24±7	24±14*	36 ^{Va} /12 ^{Pa} /51 ^{Pa} ±90	173 [#] ±3	-6.4	13	2.8
6537	862±5	856±2	49±5	47±5	14±19	20 [#] ±2	-0.2	12	2.3
6628	850±5	863±1	33±10	20±20*	144±58	179±2	1.4	10	1.4
6702	7372±10	7332±2	32±7	38±6	60±75	76 [#] ±2	8.4	15	3.6
6778	969±4	951±1	60±3	49±4	162±15	163 [#] ±2	2.7	12	2.3
6787	1173±3	1157±3	57±3	70±2	108±15	112±2	-0.7	17	4.4
7021	1979±8	1976±3	56±4	56±7*	89±17	86 [#] ±2	-0.6	14	3.1
7045	770±6	758±1	70±2	68±2	101±8	99±2	0.2	10	1.5
7154	1011±28	1009±1	64±3	65±3	100±11	95 [#] ±2	<0.1	12	2.3
7278	291±2		44±9						
7323	517±4	505±1	51±4	51±11*	19±21	38±3	<0.1	10	1.5
7429	1476±24		73±3		162±10				
7524	317±3		90±0		127±7				
7592	204±3		63±5		47±16				
7699	496±1		78±2		32±6				
7766	814±3	807±1	65±4	69±3	150±10	143 [#] ±2	<0.1	12	2.4
7831	147±4	136±3	70±3	56±12	125±7	110 [#] ±5	<0.1	9	1.2

Table B2 – continued

N ^o UGC (1)	V_{sys_Leda} km s ⁻¹ (2)	V_{sys_FP} km s ⁻¹ (3)	i_{Morph} ° (4)	i_{Kin} ° (5)	P.A. _{Morph} ° (6)	P.A. _{Kin} ° (7)	\overline{Res} 10 ⁻³ km s ⁻¹ (8)	σ_{res} km s ⁻¹ (9)	χ^2_{red} (10)
7853	537±4	530±2	58±5	58±28*	40±17	37#±4	12.8	8	1.1
7861	611±4	598±1	47±6	47±24*	116 ^{Pa} /30 ^{SDSS} ±31	117#±4	<0.1	11	1.9
7876	955±8	944±1	44±5	53±9	3±34	164#±3	0.3	8	1.1
7901	799±2	788±2	50±3	53±2	77±16	74#±2	<0.1	12	2.2
7971	467±6	457±2	26±18	31±27	25 ^{Ni} ±90	32±11	0.3	8	1.0
7985	653±3	642±2	24±12	49±6	110 ^{2M} /87 ^{Ha} /153 ^{Pa} /100 ^{Ni} /88 ^{SDSS} ±90	96#±3	-0.1	8	1.0
8334	508±3	484±1	55±5	66±1	102±16	100±1	-0.1	11	1.7
8403	969±4	975±2	54±3	57±4	129±17	121±2	-0.1	9	1.3
8490	202±2	190±1	58±8	40±15	5±17	167±3	-0.2	11	1.8
NGC 5296	2243±3	2254±2	65±6	65±4	12±22	2±3	-6.2	4	0.3
8709	2407±13	2405±3	82±3	76±1	147±5	150#±2	0.1	15	3.3
8852	2023±17	2075±1	55±7	52±3	65±24	63±2	0.9	10	1.5
8863	1796±7	1789±4	77±4	77±13*	38±8	38#±7*	-41.4	14	3.3
8898	3464±10	3448±2	71±3	27±20	30 ^{2M} /140 ^{Pa} /117 ^{SDSS} ±10	31±6	41.5	7	0.7
8900	3466±11	3511±3	66±5	57±10	172±15	161±2	5.8	20	6.6
8937	2968±9	2961±5	50±5	32±12	177±23	5#±3	2361.4	19	5.7
9013	255±23	262±1	50±4	21±16*	85±21	164±4	1.8	7	0.8
9179	302±2	293±2	53±3	36±14	33±16	49±4	<0.1	9	1.4
9219	666±11		81±6		99±13				
9248	3867±6	3865±2	58±3	58±4	86±18	81#±2	3.5	15	3.6
9358	1907±4	1912±3	62±3	54±4	2±14	2#±2	2.3	15	3.5
9366	2102±3	2109±2	66±3	62±2	45±10	45#±2	-0.6	14	2.9
9363	1584±3	1577±1	33±6	18±14*	107±42	147±3	3.2	8	1.1
9406	2279±2	2281±2	51±7	59±25	60 ^{2M} /150 ^{SDSS} ±36	132±12	78.0	11	2.0
9465	1495±3	1485±2	90±0	65±4	143±14	127±3	0.3	8	1.1
9576	1565±5	1555±2	52±4	41±11	125±21	122±3	-0.4	10	1.6
9649	447±4	440±1	70±3	54±6*	40±12	55#±3	<0.1	10	1.6
9736	3128±4	3135±2	51±3	51±5	57±19	39#±2	2.9	14	3.2
9753	771±3	764±2	74±4	69±1	2±8	3±2	0.5	11	1.8
9858	2621±3	2638±3	90±0	75±2	78±6	70±2	0.6	17	4.6
9866	427±4	430±1	69±3	56±6	150±11	148±2	-5.1	7	0.8
9943	1958±4	1946±1	48±5	54±2	87±20	86#±2	-0.1	9	1.4
9969	2519±3	2516±2	63±3	61±1	15±12	16±1	7.4	19	5.4
9992	426±4		60±5						
10075	831±3	827±1	66±3	62±2	28±10	30#±1	<0.1	9	1.4
10310	716±3	702±2	42±11	42±20*	165±47	7#±7	<0.1	11	2.0
10359	907±4	911±2	32±8	44±12*	76±43	104#±3	<0.1	13	2.5
10470	1368±3	1354±2	45±5	34±9*	155±26	107#±2	-0.6	10	1.6
10445	962±3	961±2	46±4	47±12	142±24	110±4	-0.4	11	1.8
10502	4297±5	4291±2	40±5	50±5	94±33	99±2	-0.2	20	6.4
10521	852±2	832±2	71±3	59±3	17±10	20±2	0.7	9	1.2
10546	1280±4	1268±2	55±3	42±10	9±19	2#±3	-2.9	14	3.1
10564	1132±4	1120±2	53±4	77±6	156±23	149±3	0.9	11	2.1
10652	1092±26	1089±1	30±7	21±13	56±54	45#±3	0.6	8	1.0
10713	1073±4		90±0		8±7				
10757	1168±8	1210±2	59±3	44±22	66±18	56±6	0.7	11	1.8
10769	1230±13		57±4		41±24				
10791	1328±6	1318±3	0±0	34±20*		92±4	726.5	10	1.7
10897	1334±3	1313±1	31±6	31±17*	139±40	115±3	0.3	13	2.7
11012	36±12	25±1	74±2	72±2	123±7	119#±2	0.4	8	1.0
11124	1608±4	1606±2	22±17	51±10		2#±3	-0.4	11	1.8
11218	1483±2	1477±2	64±3	58±2	36±11	42±2	-0.5	12	2.3
11269	2590±6	2563±6	60±3	69±4	97±18	92#±3	3.8	30	14.4
11283	1963±5	1944±4	34±7	34±17*	9±58	120±5	-3.7	18	4.9
11283c	1963±5		68±3		82±14				
11300	488±3	482±1	77±2	70±3	171±5	168±2	-1.6	12	2.3
11332	1569±25		82±2		65±5				
11407	2412±4	2402±8	64±3	64±22*	65±13	65±10*	1.0	20	6.6
11429	4642±4	4679±7	61±3	61±16*	23±14	28#±6			
11466	820±9	826±3	55±3	66±5	35±20	46#±3	-0.3	13	2.6

Table B2 – *continued*

N ^o UGC	V_{sys_Leda} km s ⁻¹	V_{sys_FP} km s ⁻¹	i_{Morph} °	i_{Kin} °	P.A. _{Morph} °	P.A. _{Kin} °	\overline{Res} 10 ⁻³ km s ⁻¹	σ_{res} km s ⁻¹	χ_{red}^2
(1)	(2)	(3)	(4)	(5)	(6)	(7)	(8)	(9)	(10)
11470	3530±40	3546±5	47±6	47±7	50±33	47±3	258.0	25	10.7
11496	2105±6	2115±2	0±0	44±16		167±4	135.8	9	1.2
11498	3266±8	3284±4	79±4	71±2	75±10	71 [#] ±2	-23.4	22	7.9
11557	1388±4	1392±1	29±16	29±22*		96 [#] ±3	0.1	11	1.8
11597	46±3	40±2	17±19	40±10	60 ^{Sp} ±90	61 [#] ±3	0.4	13	2.5
11670	778±3	776±3	90±0	65±2	159±7	153 [#] ±2	0.8	16	3.9
11707	906±4	897±2	65±4	70±4	65±21	59±3	0.3	11	1.8
11852	5850±8	5821±3	47±5	47±7	16±35	9 [#] ±3	4.1	20	6.8
11861	1477±4	1476±2	75±4	43±12	11±14	38 [#] ±3	<0.1	16	4.0
11872	1147±5	1140±1	54±6	47±3	88±19	86±2	-0.1	13	2.7
11891	461±4	466±6	43±10	43±23*		119±10	11.1	21	7.4
11909	1106±5		90±0		1±6				
11914	951±2	945±1	33±7	33±4	88±34	86 [#] ±2	0.2	15	3.5
11951	1085±10	1085±2	81±8	76±8	88±14	81 [#] ±4	0.2	12	2.4
12060	884±5	879±2	74±4	36±11	147±18	7 [#] ±3	-0.4	12	2.2
12082	803±2	792±2	29±11	14±19		143±5	0.6	8	1.1
12101	777±3	770±2	58±5	58±9*	133±18	137 [#] ±4	0.5	13	2.8
12212	892±4	899±2	71±9	71±27*		82±7	0.9	13	2.8
12276	5664±4	5642±2	38±6	33±15	160 ^{Pa} /55 ^{2M} ±37	142 [#] ±5	9.2	20	6.2
12276c	5664±4		24±10		41 ^{Pa} ±90				
12343	2381±3	2371±2	43±4	52±4	25±19	23 [#] ±2	-0.3	16	4.2
12632	422±5	415±2	37±13	46±16*		47±4	-0.4	9	1.3
12754	753±9	742±2	50±3	53±5	163±18	162 [#] ±2	0.2	13	2.8

(1) Name in the UGC catalog (see table B1). (2) Systemic velocity found in HyperLeda data base. (3) Systemic velocity deduced from our velocity field analysis. (4) Morphological inclination from HyperLeda (Paturel et al. 1997). (5) Inclination deduced from the analysis of our velocity field; those marked with an asterisk (*) have been fixed equal to morphological value from HyperLeda, except UGC 9649, UGC 10359, UGC 10470 for which we used morphological inclinations from NED, and UGC 508, UGC 2023, UGC 2034, UGC 2455, UGC 4499, UGC 6118, UGC 6628, UGC 9013, UGC 9363, UGC 10791 and UGC 12632 for which we used inclinations determined from HI data (see table B3). (6) Morphological position angle from HyperLeda, except for those marked (*Ha*: Haynes et al. 1999; *Ni*: Nilson 1973; *Pa*: Paturel et al. 2000; *SDSS*: 2006 Sloan Digital Sky Survey, DR5; *Sp*: Springob et al. 2007; *2M*: Two Micron All Sky Survey team 2003, 2MASS extended objects; *Va*: Vauglin et al. 1999). (7) Position angle deduced from our velocity field; those marked with an asterisk (*) have been fixed equal to morphological value. The symbol # indicates that the position angle refers to the approaching side. (8) Mean residual velocity on the whole velocity field. (9) Residual velocity dispersion on the whole velocity field. (10) Reduced χ^2 of the model.

Table B3. Galaxy parameters.

N ^o UGC (1)	t (2)	Type (3)	D Mpc (4)	M _b mag (5)	b/a (6)	i _{b/a} ° (7)	D _{25/2} "/kpc (8)	V _{max} km s ⁻¹ (9)	V _{max} flag (10)	HI data (11)
12893	8.4±0.8	Sd	12.5 ^{Ja}	-15.5	0.89±0.06	27±7	34±5/2.1±0.3	72±67	2	
89	1.2±0.6	SBa	64.2 ^{Mo}	-21.5	0.79±0.04	38±3	46±4/14.5±1.4	343±117	1	W ^{N05}
94	2.4±0.6	S(r)ab	64.2 ^{Mo}	-20.4	0.68±0.04	47±3	34±3/10.5±0.8	209±21	1	W ^{N05}
508	1.5±0.9	SBab	63.8	-21.8	0.97±0.11	14±25	85±7/26.3±2.2	553±127	1	W ^{N05}
528	2.9±1.1	SABb	12.1	-19.6	0.97±0.09	14±21	72±5/4.2±0.3	84±52	1	W ^{Web}
763	8.6±1.0	SABm	12.7 ^{Ja}	-18.9	0.74±0.04	42±3	85±6/5.2±0.4	104±11	1	
1013	3.1±0.2	SB(r)b pec	70.8	-22.0	0.31±0.03	72±2	88±6/30.1±2.0			W ^{Web}
NGC 542	2.8±3.9	Sb pec	63.7	-19.5	0.22±0.03	77±2	34±6/10.4±1.7	125±8 ^{PV}	2	
1117	6.0±0.4	Sc	0.9 ^{Sa}	-18.9	0.58±0.06	54±4	1863±64/8.1±0.3*	79±17	4	
1249	8.8±0.6	SBm pec	7.2 ^{Ka}	-18.3	0.38±0.05	68±3	193±11/6.7±0.4*	65±8 ^{PV}	3	W ^{S02}
1256	6.0±0.3	SBc pec	7.2 ^{Ka}	-18.9	0.39±0.02	67±1	210±12/7.3±0.4*	105±9	2	W ^{Web}
1317	4.9±0.7	SAB(r)c	42.2	-21.5	0.33±0.04	71±2	114±7/23.4±1.5	205±9	1	W ^{Web}
1437	4.9±1.0	SABc	66.8	-21.8	0.63±0.03	51±2	43±5/13.8±1.7	218±15	1	W ^{Web}
1655	1.0±0.5	Sa	73.0	-21.6	0.75±0.09	42±8	86±10/30.3±3.5	205±64	4	
1736	5.1±0.6	SABc	17.6 ^{Ja}	-20.1	0.69±0.03	46±3	112±7/9.5±0.6	193±68	3	
1810	3.1±0.6	Sb pec	102.4	-22.2	0.36±0.02	69±1	52±4/26.0±2.0			W ^{Web}
1886	3.6±0.6	SABb	66.5	-20.8	0.70±0.06	45±5	16±3/5.1±0.8	267±8	1	W ^{Web}
1913	7.0±0.4	SBcd	9.3 ^{Ka}	-20.1	0.53±0.04	58±3	319±13/14.4±0.6*	105±16	3	W ^{Web}
2023	9.9±0.6	I	7.8 ^{Ja}	-15.9	0.97±0.11	13±27	77±10/2.9±0.4	53±49	3	W ^{S02}
2034	9.7±1.1	IAB	10.1	-16.7	0.84±0.10	33±10	90±11/4.4±0.5	39±46	2	W ^{S02}
2045	2.0±0.4	Sab	22.7 ^{Mo}	-20.5	0.48±0.05	61±3	112±10/12.4±1.1	185±16 ^{PV}	3	W ^{N05}
2053	9.9±0.4	IB	12.7	-16.3	0.55±0.08	56±6	56±8/3.4±0.5			W ^{S02}
2082	5.9±0.5	Sc	10.2	-18.3	0.19±0.01	79±1	156±7/7.7±0.4	100±8 ^{PV}	3	W ^{Web}
2080	6.0±0.3	SABc	13.7	-19.2	0.91±0.08	24±11	127±11/8.5±0.7	131±42	1	W ^{Web}
2141	0.4±1.5	S0-a	12.2 ^{Ja}	-18.1	0.50±0.03	60±2	63±5/3.7±0.3	157±20 ^{PV}	3	W ^{N05}
2183	1.0±0.4	Sa	18.6 ^{Ja}	-19.0	0.73±0.11	43±9	56±11/5.1±1.0	160±32	1	W ^{N05}
2193	5.3±0.6	Sc	9.8 ^{Mo}	-18.7	0.55±0.04	57±2	74±5/3.5±0.2	174±423	2	W ^{Web}
2455	9.8±0.6	IB	7.8 ^{Ka}	-18.6	0.78±0.06	38±5	86±6/3.3±0.2	21±12	4	W ^{S02}
2503	2.6±1.0	SB(r)b	34.4 ^{Ko}	-21.6	0.59±0.03	54±2	97±6/16.2±1.1	285±12	1	W ^{Web}
2800	9.9±0.7	I	20.6 ^{Sw}		0.50±0.06	60±4	70±9/7.0±0.9	103±20	2	W ^{Web}
2855	5.1±0.6	SABc	17.5 ^{Ja}	-21.4	0.41±0.03	65±2	106±7/9.0±0.6	229±9	1	W ^{Web}
3013	3.1±0.5	SB(r)b	36.3	-21.3	0.57±0.03	55±2	55±5/9.6±0.8	212±21	1	W ^{Web}
3056	9.6±1.2	IB	2.5 ^{Oc}	-18.7	0.57±0.06	55±4	119±9/1.4±0.1			
3273	8.8±1.2	SAB(r)m	12.2 ^{Sw}	-18.3	0.33±0.04	71±3	77±11/4.6±0.7	106±7	3	W ^{Web}
3334	4.2±1.0	SABb	55.6	-22.8	0.70±0.07	45±6	132±8/35.7±2.2	377±85	1	W ^{Web}
3382	1.0±0.4	SB(r)a	62.8	-20.4	0.94±0.05	20±9	38±4/11.5±1.1	335±111	2	W ^{N05}
3384	8.8±0.5	Sm	17.0	-14.6	0.77±0.06	40±5	13±2/1.0±0.2			W ^{Web}
3429	2.3±0.7	SBab pec	17.9 ^{Mo}	-21.3	0.81±0.11	36±11	159±8/13.8±0.7	322±30	1	
3463	4.7±0.9	SABc	38.6	-20.7	0.49±0.03	61±2	66±4/12.4±0.8	168±9	1	
3574	5.9±0.5	Sc	21.8 ^{Ja}	-18.0	0.94±0.05	20±8	44±4/4.7±0.4*	202±96	1	W ^{Web}
3521	4.8±1.8	Sc	62.6	-19.8	0.52±0.03	59±2	35±4/10.7±1.1	166±12	3	
3528	2.0±0.3	SBab	61.8	-20.1	0.58±0.06	55±4	41±5/12.2±1.6	276±66	2	
3618	2.0±0.3	Sab	80.0	-20.9	0.70±0.05	46±4	44±4/16.9±1.4			
3691	6.1±1.0	S(r)c	28.9 ^{Sh}	-20.2	0.50±0.06	60±4	61±8/8.5±1.1	143±10	2	
3685	3.0±0.4	SB(r)b	26.3 ^{Ja}	-19.7	0.61±0.04	52±3	57±4/7.3±0.5	133±177	3	W ^{Web}
3708	4.5±1.7	Sbc pec	70.0	-20.7	0.96±0.11	15±23	25±6/8.3±2.0	234±69	1	
3709	5.7±1.6	Sc	70.7	-21.5	0.71±0.05	45±4	35±3/12.1±1.1	241±14	1	
3734	4.4±0.9	SABb	15.9 ^{Ja}	-18.6	0.90±0.04	25±6	62±5/4.7±0.3*	108±16	1	W ^{Web}
3826	6.5±0.8	SABc	25.7 ^{Ja}	-17.9	0.87±0.07	29±8	98±9/12.2±1.2	74±66	1	W ^{Web}
3809	4.0±0.3	SB(r)bc	32.9	-22.0	0.56±0.05	56±3	150±12/24.0±1.9*	258±9	1	
3740	5.4±0.6	SAB(r)c pec	17.1 ^{Sh}	-19.8	0.78±0.06	39±5	67±5/5.5±0.4	87±20	2	W ^{Web}
3851	9.8±0.6	IB	3.4 ^{Sh}	-17.1	0.33±0.02	71±1	132±8/2.2±0.1*	65±8 ^{PV}	3	W ^{S02}
3876	6.5±0.8	Scd	14.5 ^{Ja}	-17.4	0.50±0.03	60±2	57±4/4.0±0.3	112±10	2	
3915	4.6±1.6	Sbc	63.6	-21.4	0.55±0.06	57±4	34±6/10.3±1.7	205±16	1	
IC 476	4.2±2.6	SABb	63.9	-19.0	0.78±0.05	39±5	18±3/5.7±0.8	70±22	3	
4026	2.0±0.4	Sab	64.7	-20.8	0.41±0.03	66±2	43±4/13.5±1.2	284±14	2	
4165	6.9±0.4	SBcd	11.0 ^{Mo}	-18.2	0.94±0.05	20±8	74±5/3.9±0.2	80±18	1	W ^{Web}
4256	5.2±0.6	SABc	71.7	-21.6	0.82±0.04	35±4	50±4/17.3±1.3	123±59	1	W ^{Web}
4273	3.1±0.4	SBb pec	35.4 ^{Ja}	-20.7	0.48±0.05	61±3	65±6/11.2±1.1	219±11	1	W ^{Web}
4274	8.4±1.6	SBd	6.9 ^{Ka}	-17.7	0.53±0.05	58±4	62±8/2.1±0.3	102±57	2	W ^{S02}

Table B3 – *continued*

N° UGC	t	Type	D Mpc	M _b mag	b/a	i _{b/a} °	D _{25/2} "/kpc	V _{max} km s ⁻¹	V _{max} flag	HI data
(1)	(2)	(3)	(4)	(5)	(6)	(7)	(8)	(9)	(10)	(11)
4278	6.5±0.8	SBc	9.6	-19.2	0.14±0.01	82±1	87±6/4.0±0.3*	80±8 ^{PV}	2	W ^{S02}
4284	6.0±0.4	SABc	9.8	-18.4	0.52±0.03	59±2	91±6/4.3±0.3*	118±14	3	W ^{Web}
4305	9.8±0.8	I	3.4 ^{Sw}	-16.9	0.70±0.05	45±4	200±12/3.3±0.2*	48±28	2	W ^{S02}
4325	9.0±0.5	SABm	10.9 ^{Mo}	-18.2	0.54±0.03	57±2	89±6/4.7±0.3	85±13	3	W ^{S02}
4393	4.6±1.3	SBc	31.5 ^{Ja}	-19.3	0.66±0.05	49±4	44±7/6.7±1.1	47±10	4	
4422	4.9±0.6	SAB(r)c	58.1	-21.1	0.68±0.04	47±3	51±5/14.4±1.4	353±94	1	
4456	5.2±0.6	S(r)c	74.0	-20.8	0.89±0.04	27±5	31±3/11.0±1.1	211±321	1	
4499	7.9±0.8	SBd	12.2 ^{Ja}	-17.0	0.45±0.03	63±2	57±5/3.4±0.3	62±13	2	W ^{S02}
4543	8.0±0.5	Sd	30.3 ^{Sw}	-17.6	0.77±0.05	40±5	37±4/5.4±0.5	70±15	2	W ^{S02}
4555	4.0±0.6	SABb	58.0	-20.9	0.94±0.07	20±11	45±5/12.7±1.4	185±30	1	
4770	1.1±0.6	SBa	95.9	-21.3	0.83±0.07	34±8	48±5/22.3±2.3	330±194	3	
4820	1.7±0.8	S(r)ab	17.1 ^{Sh}	-20.3	0.79±0.04	38±4	127±6/10.6±0.5	336±20	1	
4936	6.9±0.3	SAB(r)c	25.6 ^{Ko}	-20.6	0.81±0.06	35±6	102±7/12.6±0.8	264±227	2	
5045	5.0±0.5	SAB(r)c	105.1	-21.2	0.76±0.04	40±4	35±3/18.0±1.5	429±228	1	
5175	3.2±0.7	Sb	44.1	-20.6	0.48±0.05	61±3	62±5/13.2±1.1	188±10	1	
5228	4.9±0.5	SBc	24.7	-19.9	0.25±0.02	76±1	68±5/8.2±0.6	125±9	1	
5251	4.3±0.8	SBbc pec	21.5	-20.5	0.22±0.01	77±1	142±7/14.8±0.7	125±9	3	W ^{Web}
5253	2.3±0.9	Sab	21.1	-20.7	0.81±0.05	36±5	108±7/11.1±0.7	235±17	1	W ^{N05}
5272	9.8±0.6	IB	7.1 ^{Ka}	-16.1	0.23±0.02	76±1	48±4/1.7±0.2	45±8 ^{PV}	3	W ^{S02}
5279	9.7±1.1	IB	21.3	-19.0	0.27±0.02	74±1	67±5/6.9±0.5	110±8 ^{PV}	1	
5316	6.5±0.8	SBc	17.6	-19.9	0.38±0.03	68±2	100±7/8.6±0.6	145±9	3	W ^{Web}
5319	5.3±0.6	SB(r)c	35.8	-19.7	0.77±0.05	39±4	47±3/8.2±0.6	180±47	2	
5351	2.1±0.6	SABa	19.3 ^{Sh}	-19.4	0.32±0.04	71±2	62±3/5.8±0.3	135±8 ^{PV}	1	W ^{N05}
5373	9.9±0.3	IB	1.4 ^{Ka}	-14.3	0.62±0.05	52±4	148±10/1.0±0.1	90±162	2	
5398	7.9±3.8	Sd	3.8 ^{Ka}	-17.8	0.81±0.08	36±8	162±13/3.0±0.2			
5414	9.9±0.2	IAB(r)	10.0 ^{Sw}	-16.6	0.68±0.08	47±6	90±10/4.3±0.5	74±10	2	W ^{S02}
IC 2542	4.6±1.3	SBc	83.4	-20.5	0.75±0.04	42±4	31±3/12.4±1.2	290±192	2	
5510	4.6±1.0	SAB(r)c	18.6	-19.3	0.80±0.05	37±5	64±6/5.8±0.5	167±44	1	
5532	3.9±0.6	Sbc	41.1	-22.1	0.85±0.08	32±8	122±10/24.2±1.9	398±24	1	W ^{Web}
5556	5.0±0.8	SBc pec	22.2	-18.9	0.32±0.02	71±1	67±4/7.2±0.4			W ^{Web}
5721	6.6±0.8	SBcd	6.5 ^{Ka}	-16.5	0.50±0.03	60±2	49±4/1.5±0.1	99±29	3	W ^{S02}
5786	4.0±0.1	SAB(r)b	14.2 ^{Sh}	-19.6	0.96±0.11	15±23	54±6/3.7±0.4	80±15	3	W ^{Web}
5789	5.9±0.4	SBc	14.1 ^{Sa}	-19.6	0.49±0.04	61±2	109±7/7.4±0.5*	131±10	3	W ^{Web}
5829	9.7±0.9	IB	9.0 ^{Sw}	-16.2	0.92±0.07	22±11	135±9/5.9±0.4*	48±26	2	W ^{S02}
5840	4.0±0.3	SB(r)bc	6.9 ^{Ka}	-18.9	0.95±0.07	17±13	200±10/6.7±0.3*	251±138	1	W ^{Web}
5842	6.0±0.4	SBc	15.2 ^{Sh}	-18.8	0.83±0.05	34±5	79±5/5.8±0.4	115±18	2	
5931	5.9±0.5	SBc pec	21.2 ^{Sh}	-19.8	0.55±0.05	56±4	52±6/5.3±0.6	157±32	3	
5935	9.4±1.5	SBm pec	26.4 ^{Sw}	-20.5	0.41±0.04	66±2	93±11/11.9±1.4		4	W ^{S02}
5982	5.1±0.7	SBc	20.8 ^{Sh}	-20.0	0.56±0.05	56±4	120±10/12.1±1.0	199±13	1	W ^{Web}
6118	2.1±0.6	SB(r)ab	19.8 ^{Sh}	-20.0	0.90±0.05	26±7	74±5/7.1±0.4	137±24	1	W ^{N05}
6277	5.1±0.5	SABc	16.9	-19.5	0.96±0.07	17±15	106±9/8.7±0.7	270±258	2	√ ^{K00}
6419	8.9±0.9	SBm	18.8	-18.6	0.65±0.04	50±3	44±4/4.0±0.4	53±11	3	√ ^{W04}
6521	3.7±0.9	S(r)bc	78.6	-21.2	0.67±0.03	48±2	50±3/19.1±1.2	249±18	1	
6523	1.4±1.1	Sa	80.0	-21.0	0.92±0.04	23±7	32±3/12.5±1.3	118±63	4	
6537	5.1±0.5	SB(r)c	14.3 ^{Tu}	-20.5	0.67±0.05	48±4	158±9/11.0±0.6*	187±17	1	W ^{Web}
6628	8.8±1.0	SAB(r)m	15.3 ^{Sw}	-17.9	0.87±0.07	30±8	65±6/4.8±0.5	183±168	3	W ^{S02}
6702	1.3±1.0	Sa	99.8	-20.6	0.86±0.05	31±6	24±3/11.5±1.5	195±23	1	
6778	5.1±0.8	SABc pec	15.5 ^{Sh}	-20.7	0.53±0.03	58±2	81±6/6.1±0.4	223±14	2	W ^{Web}
6787	1.7±0.8	Sab	18.9	-20.5	0.60±0.03	53±2	104±6/9.5±0.5	232±10	2	W ^{N05}
7021	1.3±0.8	SAB(r)a	26.8	-19.7	0.62±0.04	52±3	77±5/10.0±0.6	223±18	1	
7045	5.3±0.6	SABc	11.4 ^{Mo}	-19.2	0.39±0.03	67±2	124±6/6.9±0.3	160±9	1	
7154	6.9±0.4	SBcd	16.2	-20.0	0.46±0.03	63±2	139±9/10.9±0.7	145±9	1	W ^{Web}
7278	9.8±0.5	IB	2.9 ^{Sh}	-17.4	0.78±0.08	39±8	204±12/2.9±0.2			W ^{S02}
7323	8.0±0.4	SBd	8.1 ^{Sw}	-18.3	0.70±0.04	45±3	114±7/4.5±0.3	84±15	2	W ^{S02}
7429	2.4±0.7	SB(r)ab	23.7	-19.8	0.40±0.03	67±2	73±5/8.4±0.6			
7524	8.8±0.7	SB(r)m	4.6 ^{Ko}	-18.4	0.33±0.02	71±1	125±8/2.8±0.2*	45±8 ^{PV}	3	W ^{S02}
7592	9.8±0.5	IB	2.9 ^{Sh}	-18.3	0.58±0.04	54±3	140±9/2.0±0.1			W ^{S02}
7699	6.0±0.6	SBc	9.3	-17.6	0.28±0.01	74±1	108±6/4.9±0.3	92±8 ^{PV}	1	
7766	6.0±0.4	SBc	13.0	-21.0	0.46±0.05	63±3	317±15/20.0±1.0*	120±9	1	W ^{Web}
7831	4.9±0.4	SBc	5.2 ^{Ka}	-18.5	0.39±0.03	67±2	177±8/4.5±0.2	92±15	2	W ^{Web}

Table B3 – continued

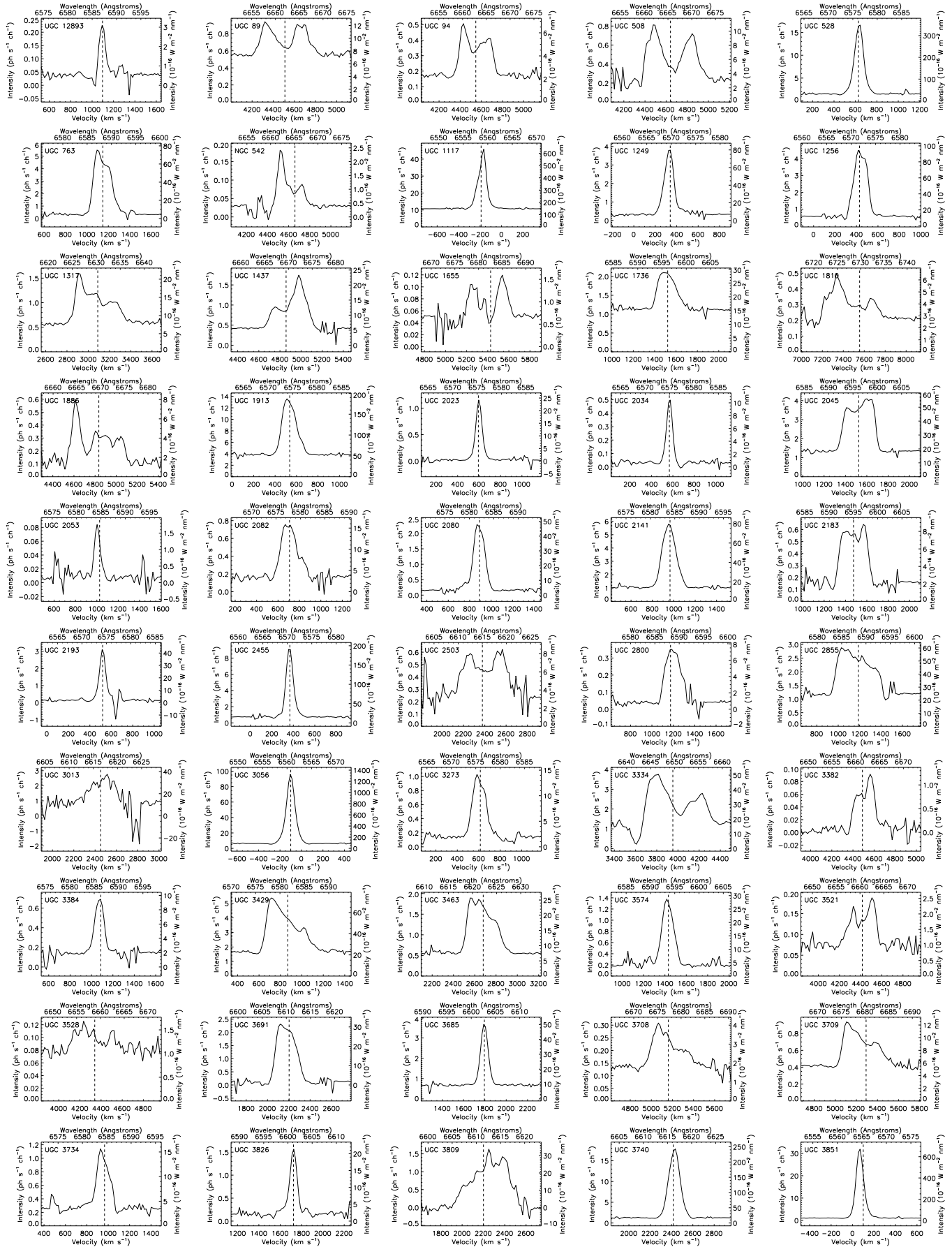
N ^o UGC	t	Type	D Mpc	M _b mag	b/a	i _{b/a} °	D _{25/2} "/kpc	V _{max} km s ⁻¹	V _{max} flag	HI data
(1)	(2)	(3)	(4)	(5)	(6)	(7)	(8)	(9)	(10)	(11)
7853	8.6±1.1	SBm	8.9 ^{Mo}	-18.9	0.64±0.05	50±3	106±6/4.6±0.3	110±35	3	W ^{Web}
7861	8.8±0.7	SAB(r)m pec	10.2 ^{Mo}	-17.3	0.75±0.05	41±4	41±4/2.0±0.2	50±21	3	W ^{Web}
7876	6.5±0.9	SABc	14.5	-17.9	0.72±0.05	44±4	58±7/4.1±0.5	98±14	2	
7901	5.2±0.6	Sc pec	20.7 ^{Sh}	-20.6	0.66±0.03	49±3	115±6/11.6±0.6	215±10	1	
7971	8.7±0.5	Sm	8.4 ^{Sw}	-16.3	0.92±0.11	24±15	66±8/2.7±0.3	33±27	3	W ^{S02}
7985	6.9±0.5	SBcd	13.7 ^{Mo}	-18.7	0.92±0.08	23±11	51±5/3.4±0.3	112±13	1	
8334	4.0±0.2	Sbc	9.8	-21.1	0.61±0.06	53±4	356±20/16.9±1.0*	214±9	1	
8403	5.8±0.6	SBc	19.1 ^{Ja}	-19.2	0.61±0.04	52±3	90±6/8.3±0.6	128±10	1	W ^{Web}
8490	8.9±0.4	Sm	4.7 ^{Sh}	-17.1	0.64±0.07	51±5	135±8/3.1±0.2*	90±29	2	W ^{S02}
NGC 5296	-1.1±0.8	S0-a	32.8	-18.2	0.58±0.04	54±3	28±3/4.5±0.5	80±9	3	W ^{Web}
8709	4.9±0.8	SABc pec	35.0	-21.4	0.24±0.02	76±1	112±7/19.0±1.1	207±9	1	W ^{Web}
8852	2.3±0.6	SAB(r)a	30.6	-20.0	0.62±0.08	52±6	77±9/11.4±1.3	186±10	3	
8863	1.1±0.4	SBa	25.5 ^{Ko}	-20.3	0.39±0.03	67±2	108±5/13.4±0.6	191±13	2	W ^{N05}
8898	3.1±0.6	SBb pec	49.0	-20.5	0.41±0.03	66±2	79±6/18.7±1.3	65±45	4	W ^{Web}
8900	3.2±0.6	Sb pec	49.2	-21.7	0.47±0.06	62±4	75±8/17.8±1.8	345±37	2	W ^{Web}
8937	3.1±0.4	SBb	49.0 ^{Mo}	-21.1	0.67±0.06	48±4	69±6/16.4±1.4	320±105	1	
9013	6.0±0.3	Sc pec	7.2 ^{Ka}	-18.2	0.66±0.04	49±3	72±5/2.5±0.2*	62±45	2	V ^{R94}
9179	6.9±0.4	SABc	5.7 ^{Ka}	-17.8	0.61±0.03	52±2	128±8/3.5±0.2	111±36	3	
9219	9.7±1.4	IB	10.2 ^{Ja}	-16.6	0.44±0.03	64±2	49±4/2.4±0.2	45±8 ^{PV}	2	
9248	3.1±0.5	Sb	54.9	-20.2	0.57±0.03	55±2	40±4/10.6±1.0	166±11	1	
9358	3.3±0.8	SABb	29.1	-20.8	0.52±0.03	59±2	94±6/13.3±0.9	221±14	1	
9366	4.7±0.9	Sc	37.7 ^{Mo}	-21.7	0.45±0.03	63±2	107±6/19.6±1.2	241±9	1	W ^{Web}
9363	6.9±0.4	S(r)cd	22.3	-19.8	0.84±0.05	33±6	57±5/6.2±0.5*	143±105	1	V ^{S96}
9406	6.9±0.4	SB(r)cd	33.8	-19.0	0.64±0.08	50±6	44±8/7.3±1.3	19±10	4	
9465	7.9±0.9	SABd	26.4 ^{Ja}	-18.0	0.40±0.03	67±2	23±3/3.0±0.4	97±9	1	
9576	6.9±0.4	SABc pec	27.4 ^{Ja}	-19.6	0.63±0.05	51±4	51±4/6.8±0.6	104±25	1	V ^{I94}
9649	3.1±0.7	SBb	7.7 ^{Ja}	-16.5	0.42±0.03	65±2	56±5/2.1±0.2	94±11	2	W ^{Web}
9736	5.0±0.7	SABc	45.4	-20.6	0.65±0.03	49±2	71±4/15.7±1.0	192±16	1	
9753	3.5±0.7	Sbc	12.4 ^{Sh}	-19.1	0.36±0.04	69±2	114±7/6.8±0.4	138±9	1	W ^{Web}
9858	4.0±0.5	SABb	38.2	-20.4	0.20±0.02	79±1	118±12/21.8±2.3	160±9	2	W ^{Web}
9866	4.0±0.3	S(r)bc	7.4 ^{Ja}	-17.2	0.41±0.03	65±2	55±4/2.0±0.1	114±11	2	
9943	5.0±0.6	SB(r)c	28.0	-20.7	0.69±0.05	46±4	82±5/11.1±0.7	185±10	1	
9969	3.1±0.3	SB(r)b	36.0 ^{Sh}	-21.4	0.50±0.03	60±2	119±7/20.8±1.3	311±9	1	W ^{Web}
9992	9.8±0.6	I	10.4	-15.3	0.61±0.05	52±4	44±6/2.2±0.3			W ^{S02}
10075	6.0±0.4	Sc	14.7 ^{Ja}	-19.9	0.44±0.04	64±3	174±9/12.4±0.7	168±9	1	
10310	9.2±0.6	SBm	12.7 ^{Sw}	-17.1	0.80±0.09	37±9	77±10/4.7±0.6	66±27	3	W ^{S02}
10359	5.6±0.6	SBc pec	16.0	-19.0	0.85±0.07	32±8	63±5/4.9±0.4*	143±30	1	W ^{Web}
10470	4.0±0.2	SB(r)bc	21.2 ^{Ja}	-20.2	0.73±0.05	43±4	67±5/6.9±0.5	164±39	1	W ^{Web}
10445	6.0±0.9	SB(r)c pec	16.9 ^{Ja}	-17.6	0.71±0.04	45±3	57±4/4.7±0.3	77±17	2	W ^{Web}
10502	5.3±0.6	Sc	61.2	-21.2	0.78±0.05	39±4	60±5/17.9±1.5	163±14	1	W ^{Web}
10521	4.9±0.7	Sc	18.0 ^{Mo}	-20.2	0.38±0.03	68±2	106±9/9.3±0.7	124±9	1	
10546	6.0±0.5	SABc	20.4 ^{Ja}	-19.1	0.59±0.04	54±3	55±5/5.4±0.4	106±22	1	W ^{Web}
10564	6.5±0.8	SBc	18.4 ^{Ja}	-17.6	0.62±0.05	52±3	37±4/3.3±0.3	75±8	2	W ^{Web}
10652	3.8±2.6	S(r)bc	18.2	-17.7	0.87±0.05	29±6	33±3/2.9±0.3	141±82	2	
10713	3.0±0.4	Sb	18.3	-19.0	0.19±0.02	79±1	54±7/4.8±0.7	105±8 ^{PV}	2	W ^{Web}
10757	6.0±0.4	Sc	19.5	-17.7	0.53±0.04	58±2	36±4/3.4±0.4	81±33	3	W ^{Web}
10769	3.0±0.5	SABb	20.0	-17.0	0.59±0.04	54±3	28±3/2.7±0.3			W ^{Web}
10791	8.8±0.5	SABm	21.7	-16.7	1.00±0.13	0±0	56±9/5.9±0.9	95±48	3	W ^{Web}
10897	5.2±0.5	SABc	20.5 ^{Ja}	-19.5	0.86±0.05	30±6	64±4/6.3±0.4	113±56	2	W ^{Web}
11012	5.9±0.7	Sc	5.3 ^{Ka}	-18.7	0.33±0.03	71±2	185±11/4.7±0.3	117±9	1	
11124	5.9±0.5	SBc	23.7 ^{Ja}	-18.6	0.93±0.10	22±16	67±10/7.7±1.1	96±15	2	W ^{Web}
11218	5.2±0.6	Sc	22.8 ^{Ko}	-20.8	0.48±0.03	61±2	100±5/11.0±0.6	185±9	1	W ^{Web}
11269	2.0±0.5	SABa	35.0 ^{Ja}	-19.9	0.56±0.04	56±3	56±5/9.5±0.8	202±13	1	W ^{N05}
11283	7.8±0.9	SBd	31.3 ^{Sw}	-19.3	0.86±0.05	31±6	40±4/6.1±0.7	173±73	2	W ^{Web}
11283c	5.4±2.2	Sc	31.3 ^{Sw}	-16.5	0.41±0.03	66±2	28±3/4.2±0.5			W ^{Web}
11300	6.4±0.9	SABc	8.4 ^{Ja}	-17.8	0.28±0.01	74±1	99±5/4.0±0.2*	112±9	2	W ^{Web}
11332	7.0±0.5	SBcd	23.0 ^{Ja}	-19.5	0.21±0.01	78±1	63±5/7.1±0.5	91±8 ^{PV}	3	
11407	3.6±0.6	SBbc	35.8	-20.8	0.49±0.03	61±2	75±6/13.0±1.0	158±30	1	V ^{W01}
11429	3.1±0.5	SBb	65.2	-21.8	0.53±0.03	58±2	63±4/19.8±1.3	232±35	2	W ^{Web}
11466	4.8±1.9	Sc	14.2	-18.5	0.59±0.03	54±2	45±4/3.1±0.3	133±10	1	W ^{Web}

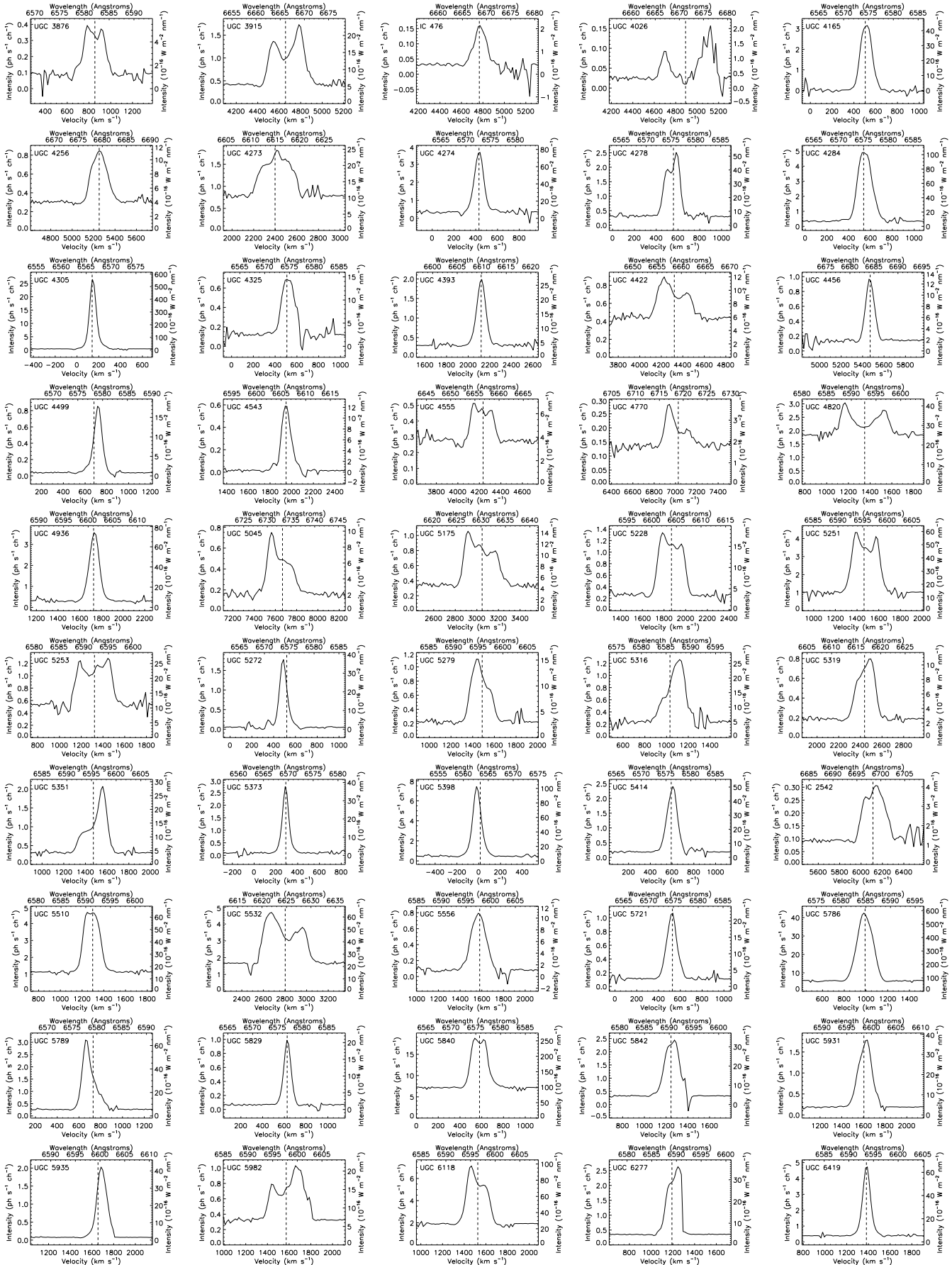
Table B3 – *continued*

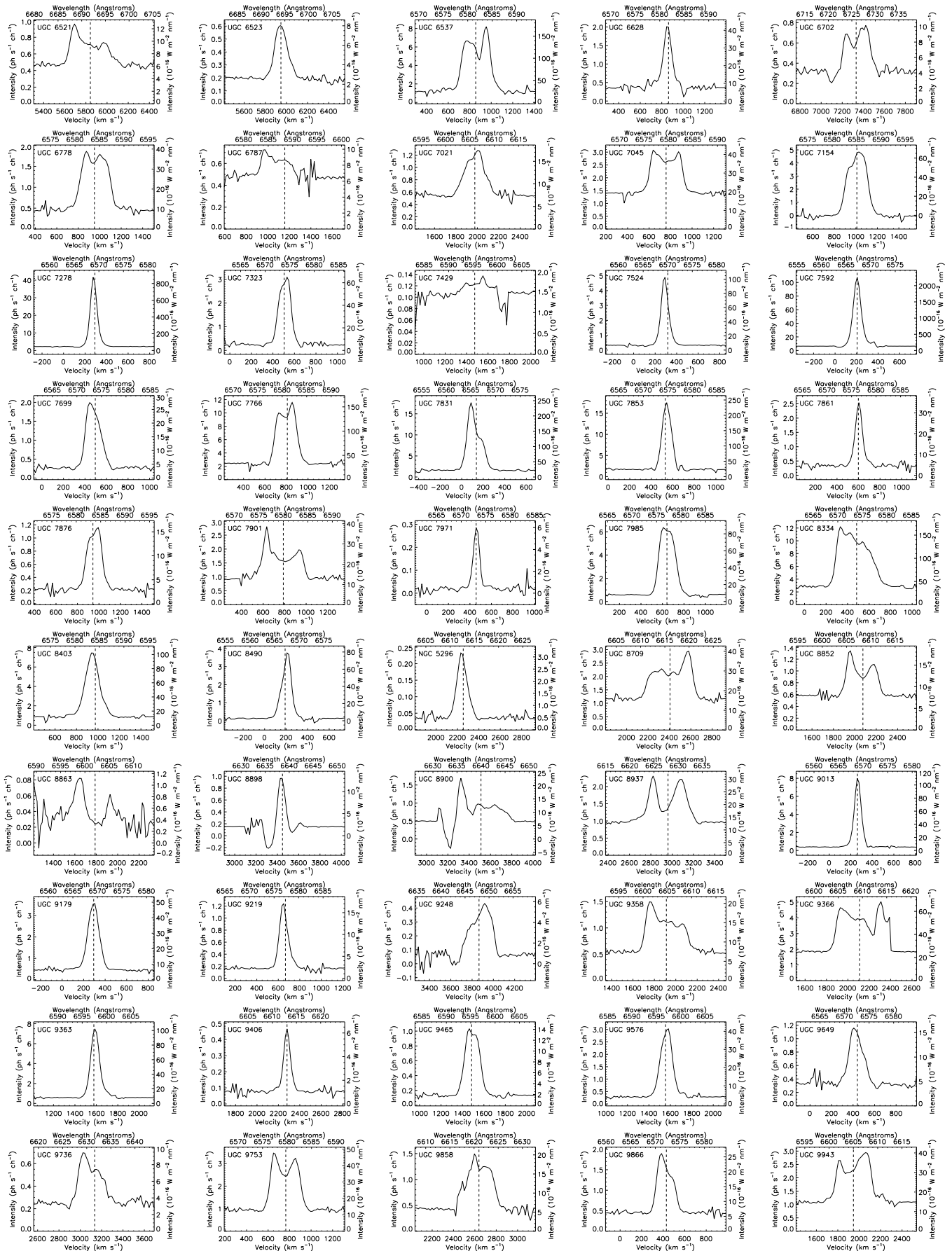
N° UGC	t	Type	D Mpc	M _b mag	b/a	i _{b/a}	D _{25/2} "/kpc	V _{max} km s ⁻¹	V _{max} flag	HI data
(1)	(2)	(3)	(4)	(5)	(6)	(7)	(8)	(9)	(10)	(11)
11470	2.2±0.6	Sab	50.8	-21.3	0.71±0.07	45±5	72±9/17.8±2.2	380±40	2	
11496	8.8±0.5	Sm	31.9		1.00±0.13	0±0	57±9/8.9±1.3	96±29	2	W ^{Web}
11498	3.1±0.7	SBb	44.9	-20.5	0.32±0.04	71±2	84±9/18.2±1.9	274±9	1	
11557	7.8±0.9	SABd	19.7 ^{Sw}	-18.4	0.90±0.11	26±14	59±8/5.7±0.8	105±72	2	W ^{S02}
11597	5.9±0.3	SABc	5.9 ^{Ka}	-20.6	0.96±0.09	16±18	342±14/9.8±0.4*	154±32	3	
11670	0.5±1.0	S(r)a	12.8	-19.4	0.33±0.03	71±2	125±7/7.7±0.4	190±9	1	W ^{N05}
11707	7.9±1.0	Sd	15.9 ^{Sw}	-16.6	0.57±0.03	55±2	31±3/2.4±0.3	97±5	2	W ^{S02}
11852	1.0±0.5	SBa	80.1	-20.2	0.72±0.05	44±4	28±3/10.8±1.3	221±27	2	W ^{N05}
11861	7.8±0.9	SABd	25.1 ^{Sw}	-20.2	0.48±0.03	61±2	54±4/6.5±0.5	181±39	2	W ^{S02}
11872	2.5±0.5	SAB(r)b	18.1 ^{Ko}	-20.0	0.63±0.07	51±5	85±6/7.4±0.5	183±12	1	
11891	9.9±0.5	I	9.0	-16.4	0.78±0.08	39±8	100±15/4.3±0.6	83±35	3	W ^{Web}
11909	4.5±1.6	Sbc	17.7	-19.3	0.20±0.01	78±1	61±6/5.2±0.5	110±8 ^{PV}	2	W ^{Web}
11914	2.5±0.7	S(r)ab	15.0 ^{Ko}	-20.3	0.86±0.06	31±6	135±7/9.8±0.5	285±26	1	W ^{N05}
11951	1.1±0.8	SBa	17.4	-19.3	0.36±0.04	69±3	51±8/4.3±0.7	106±7	3	W ^{N05}
12060	9.9±0.5	IB	15.7 ^{Sw}	-16.5	0.49±0.03	61±2	33±4/2.5±0.3	107±27	1	W ^{S02}
12082	8.7±0.8	SABm	10.1 ^{Ja}	-16.4	0.90±0.07	26±10	81±9/3.9±0.4	105±137	3	W ^{Web}
12101	6.6±0.9	Scd	15.1 ^{Sh}	-18.5	0.55±0.06	57±4	77±7/5.6±0.5	94±12	3	V ^{W02}
12212	8.7±0.5	Sm	15.5 ^{Sw}		0.51±0.07	59±5	59±10/4.4±0.7	78±15	4	W ^{Web}
12276	1.1±0.5	SB(r)a	77.8	-20.7	0.81±0.06	36±5	34±3/12.8±1.1	94±37	2	W ^{N05}
12276c	5.1±5.0	S?	77.8	-17.4	0.92±0.06	23±9	9±2/3.3±0.7			W ^{N05}
12343	4.4±0.9	SBbc	26.9 ^{Ja}	-21.1	0.75±0.03	42±3	109±5/14.2±0.6	221±14	1	V ^{L98}
12632	8.7±0.5	SABm	8.0	-17.4	0.83±0.11	34±11	127±14/4.9±0.6	69±19	2	W ^{S02}
12754	6.0±0.4	SBC	8.9 ^{Sw}	-18.6	0.65±0.03	49±2	109±6/4.7±0.3*	123±11	1	W ^{Web}

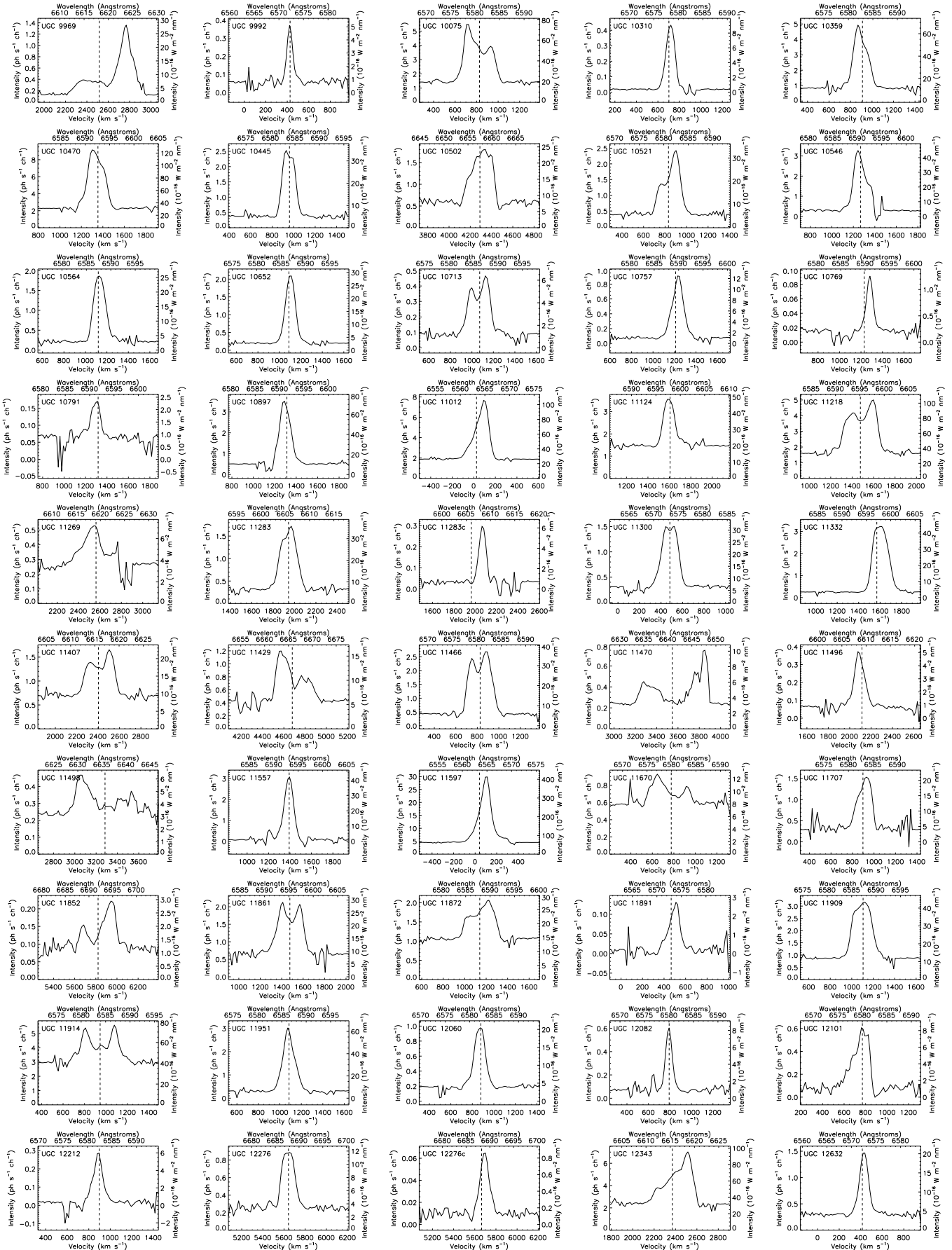
(1) Name of the galaxy in the UGC catalog (see table B1). (2) Morphological type from the de Vaucouleurs classification (de Vaucouleurs 1979) in HyperLeda data base. (3) Morphological type from HyperLeda data base. (4) Distance D, deduced from the systemic velocity taken in NED corrected from Virgo infall, assuming $H_0 = 75 \text{ km s}^{-1} \text{ Mpc}^{-1}$, except for those marked (*Ja*: James et al. 2004; *Ka*: Karachentsev et al. 2004; *Ko*: Koopmann et al. 2006; *Mo*: Moustakas & Kennicutt 2006; *Oc*: O’Connell et al. 1994; *Sa*: Saha et al. 2006; *Sh*: Shapley et al. 2001; *Tu*: Tully et al. 1996). (5) Absolute B magnitude from D and apparent corrected B magnitude (HyperLeda). (6) Axis ratio from HyperLeda. (7) Inclination derived from the axis ratio ($\arccos b/a$). (8) Isophotal radius at the limiting surface brightness of 25 B mag/sq arcsec, from HyperLeda (Paturel et al. 1991) in arcsecond and kpc adopting the distance given in column 4; an asterisk (*) indicates that the galaxy is larger than GHASP field of view. (9) Maximum velocity, V_{max} , derived from the fit of the velocity field or from the position-velocity diagram (marked with ^{PV}). (10) Quality flag on V_{max} (1: reached; 2: probably reached; 3 probably not reached; 4: not reached). (11) Aperture synthesis HI data references: W for WHISP data (S02: Swaters et al. 2002; N05: Noordermeer et al. 2005; *web*: <http://www.astro.rug.nl/~whisp>); V for VLA data (I94: Irwin 1994; R94: Rownd et al. 1994; S96: Schulman et al. 1996; L98: Laine & Gottesman 1998; K00: Kornreich et al. 2000; W01: Wilcots et al. 2001; W02: Williams et al. 2002; W04: Wilcots & Prescott 2004).

APPENDIX C: H α PROFILES









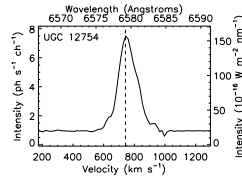


Figure C1. Integrated $H\alpha$ profiles. The profiles have been displayed over three times the spectral range ($\sim 25\text{\AA}$, top label or $\sim 1100\text{ km s}^{-1}$, bottom label). The instrumental intensity in photo-electron per second and per channel is given on the left Y-axis. The calibrated intensity is displayed on the right Y-axis. The dashed vertical line indicates the systemic velocity provided by our kinematical models (see Table B2).

**APPENDIX D: INDIVIDUAL MAPS AND
POSITION-VELOCITY DIAGRAMS**

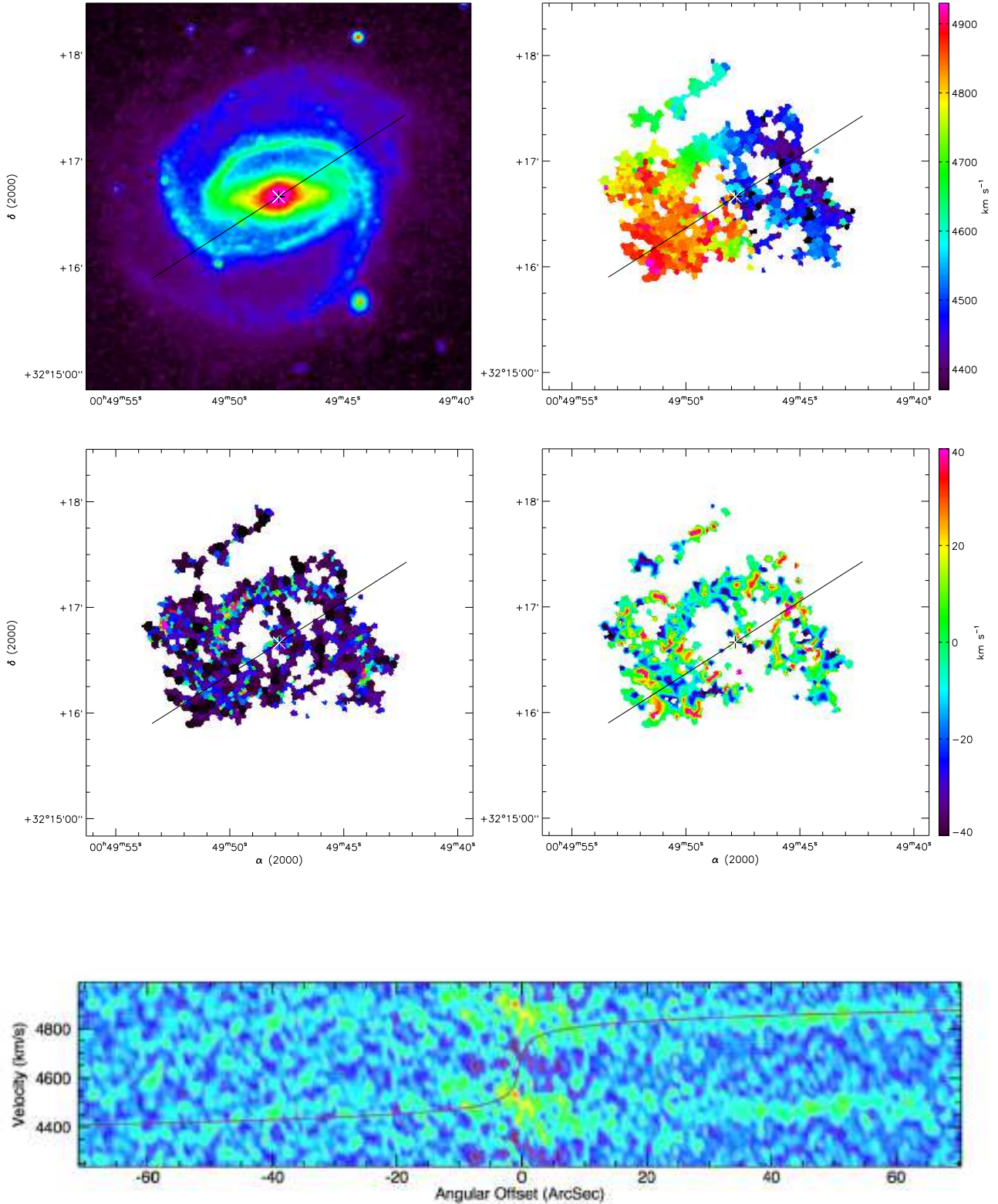


Figure D1. UGC 508. **Top left:** XDSS Blue Band image. **Top right:** H α velocity field. **Middle left:** H α monochromatic image. **Middle right:** H α residual velocity field. The white & black cross is the kinematical center. The black line is the major axis, its length represents the D_{25} . **Bottom:** Position-velocity diagram along the major axis (full width of 7 pixels), arbitrary flux units. The red line plots the rotation curve computed from the model velocity field along the major axis (full width of 7 pixels).

APPENDIX E: ROTATION CURVES

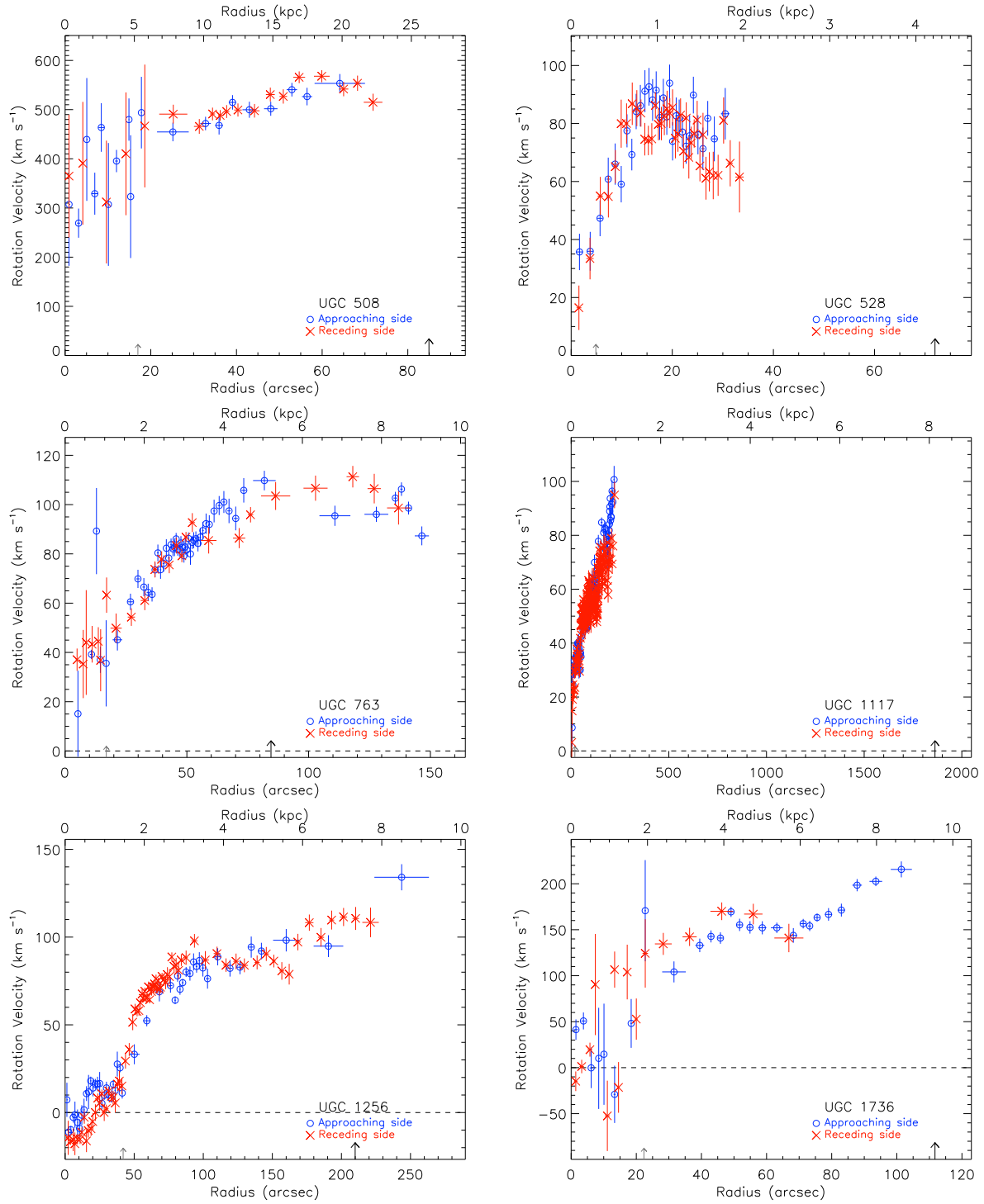


Figure E1. From top left to bottom right: $\text{H}\alpha$ rotation curve of UGC 508, UGC 528, UGC 763, UGC 1117, UGC 1256, and UGC 1736.

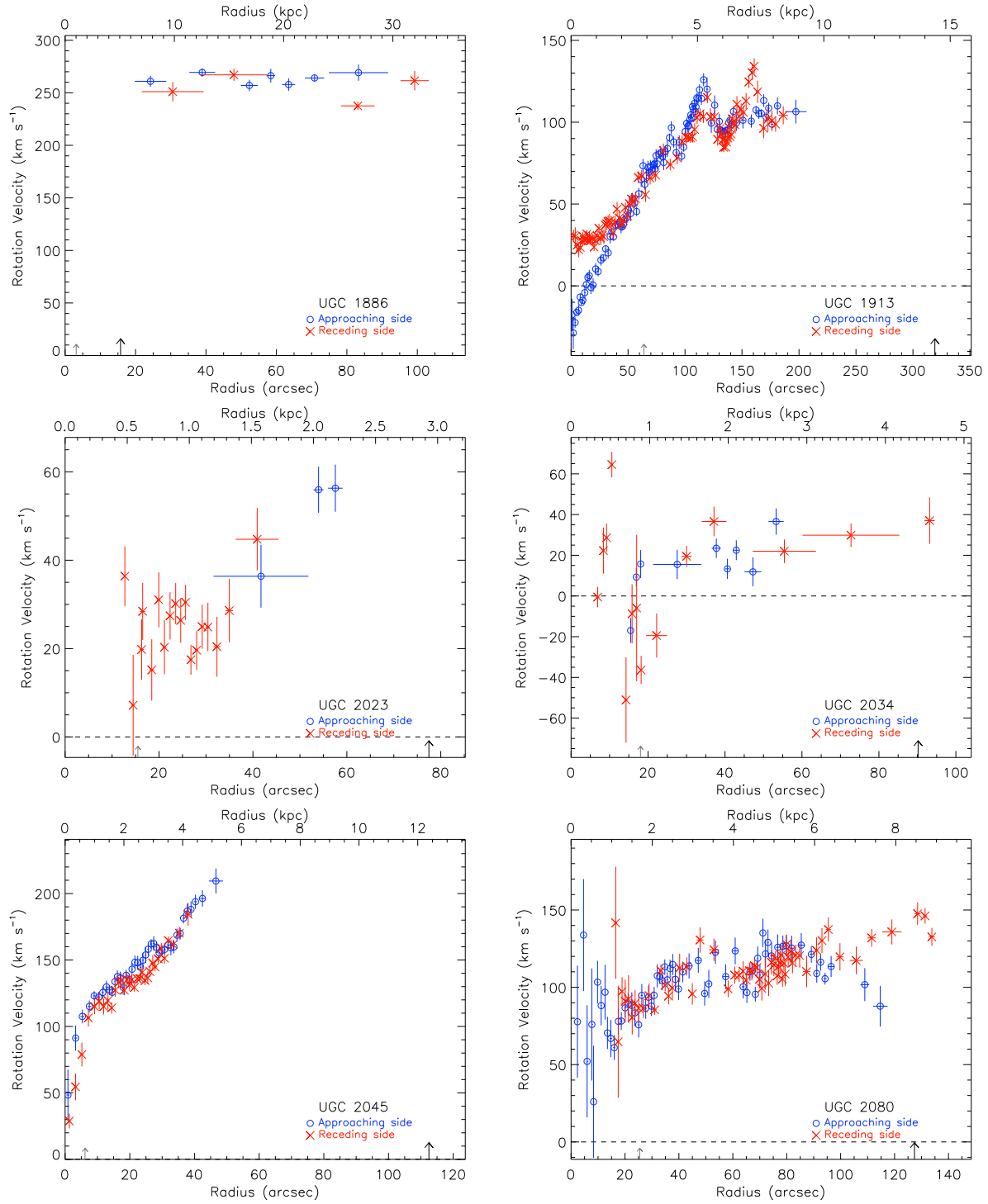


Figure E2. From top left to bottom right: $H\alpha$ rotation curve of UGC 1886, UGC 1913, UGC 2023, UGC 2034, UGC 2045, and UGC 2080.

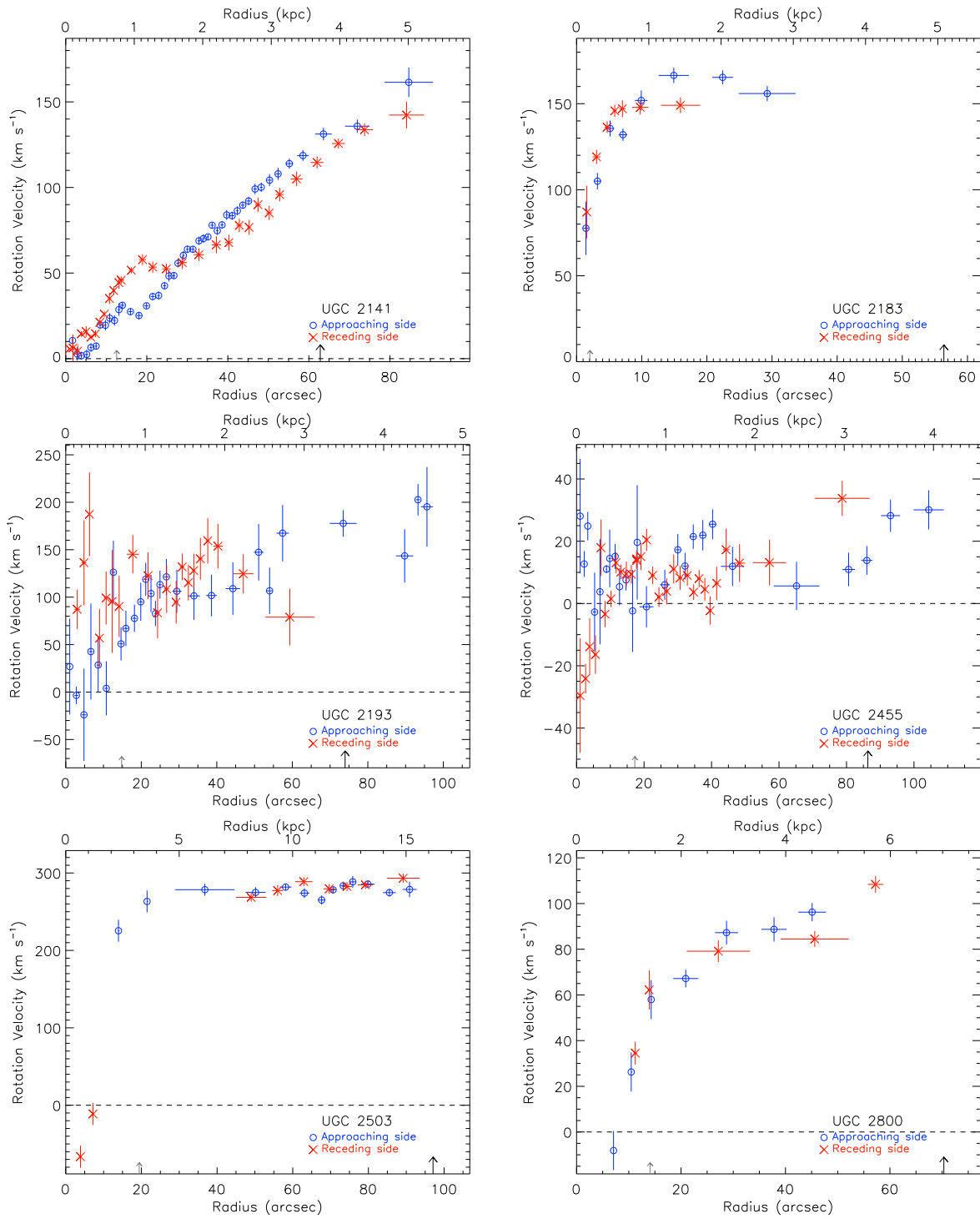


Figure E3. From top left to bottom right: H α rotation curve of UGC 2141, UGC 2183, UGC 2193, UGC 2455, UGC 2503, and UGC 2800.

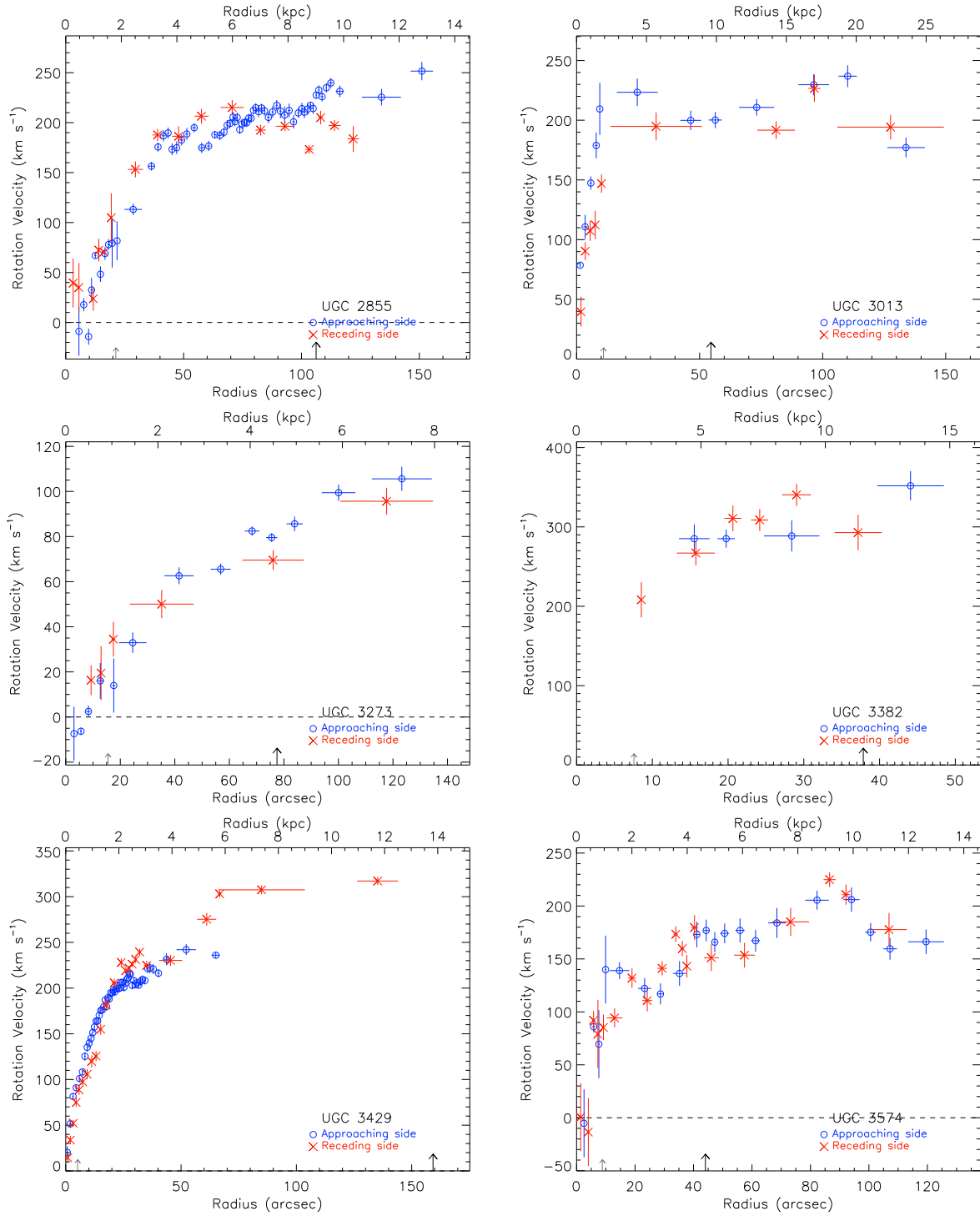


Figure E4. From top left to bottom right: H α rotation curve of UGC 2855, UGC 3013, UGC 3273, UGC 3382, UGC 3429, and UGC 3574.

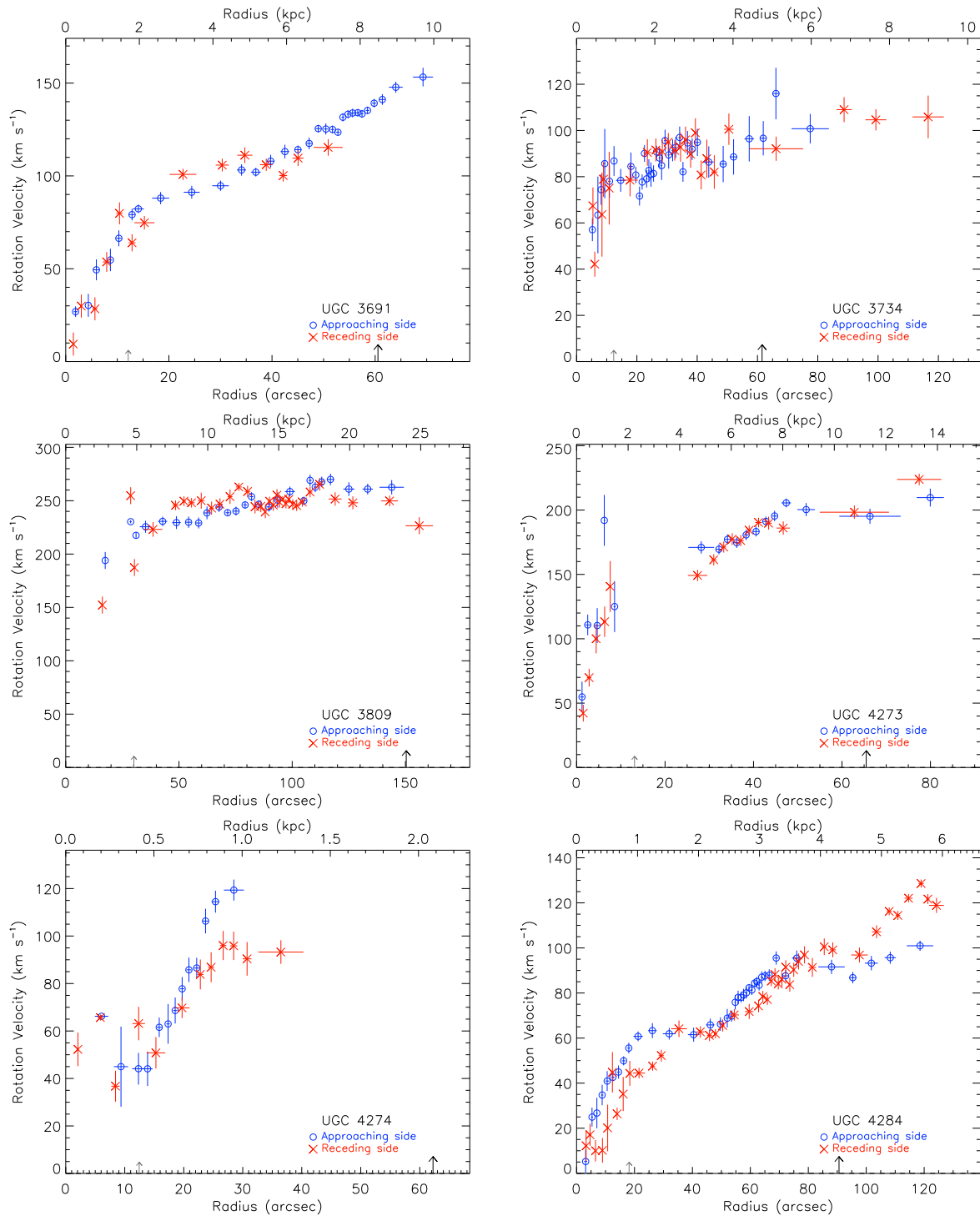


Figure E5. From top left to bottom right: H α rotation curve of UGC 3691, UGC 3734, UGC 3809, UGC 4273, UGC 4274, and UGC 4284.

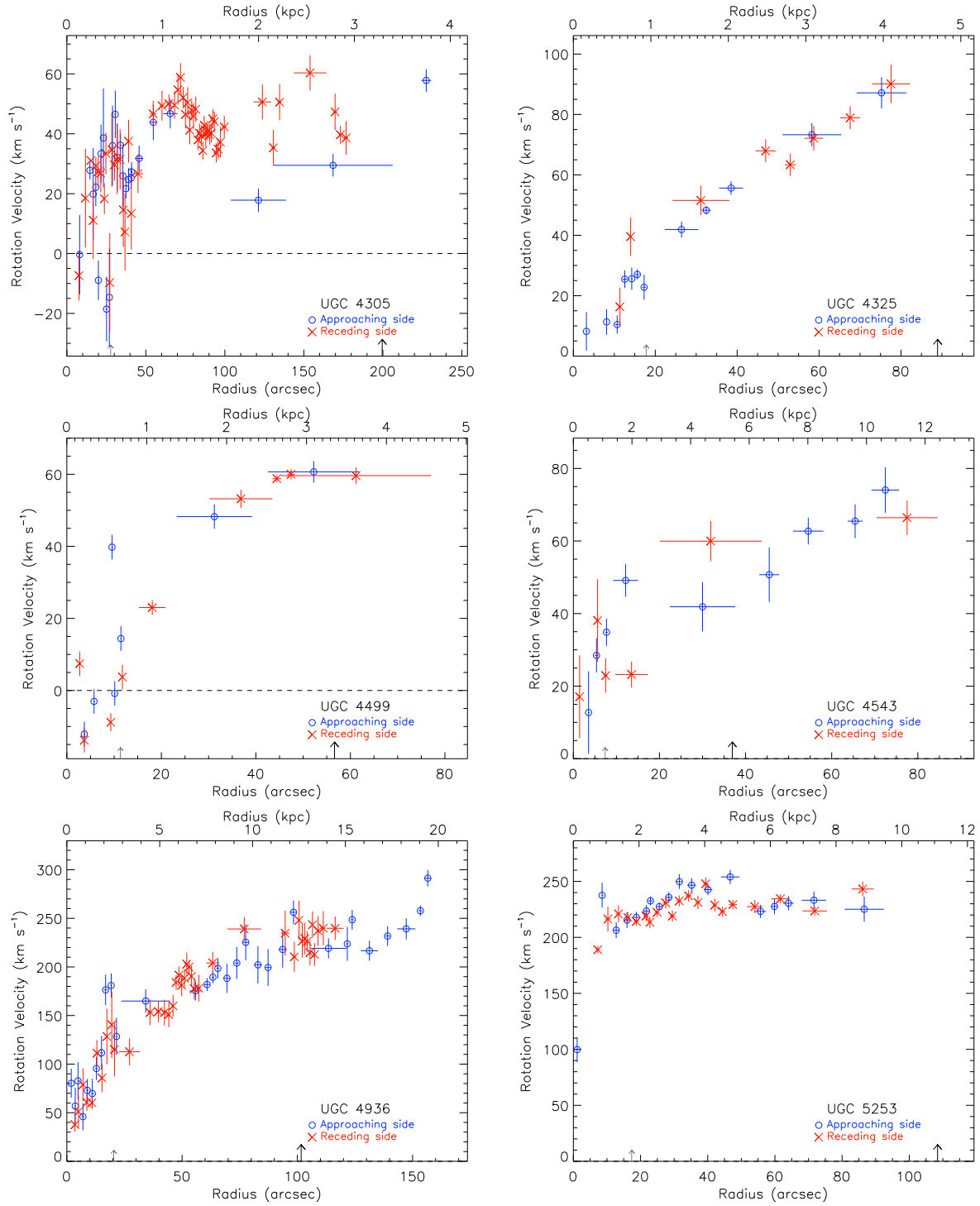


Figure E6. From top left to bottom right: H α rotation curve of UGC 4305, UGC 4325, UGC 4499, UGC 4543, UGC 4936, and UGC 5253.

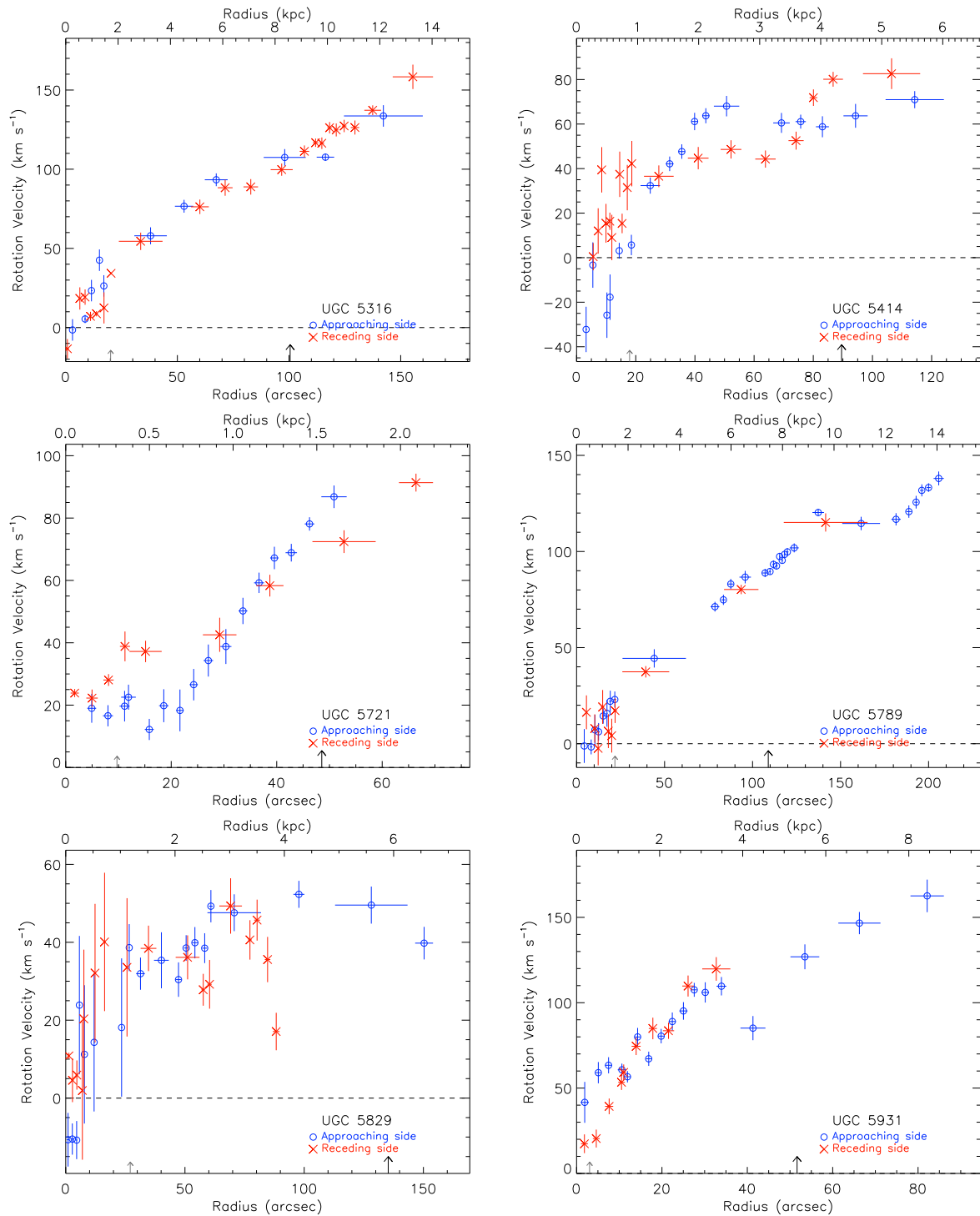


Figure E7. From top left to bottom right: H α rotation curve of UGC 5316, UGC 5414, UGC 5721, UGC 5789, UGC 5829, and UGC 5931.

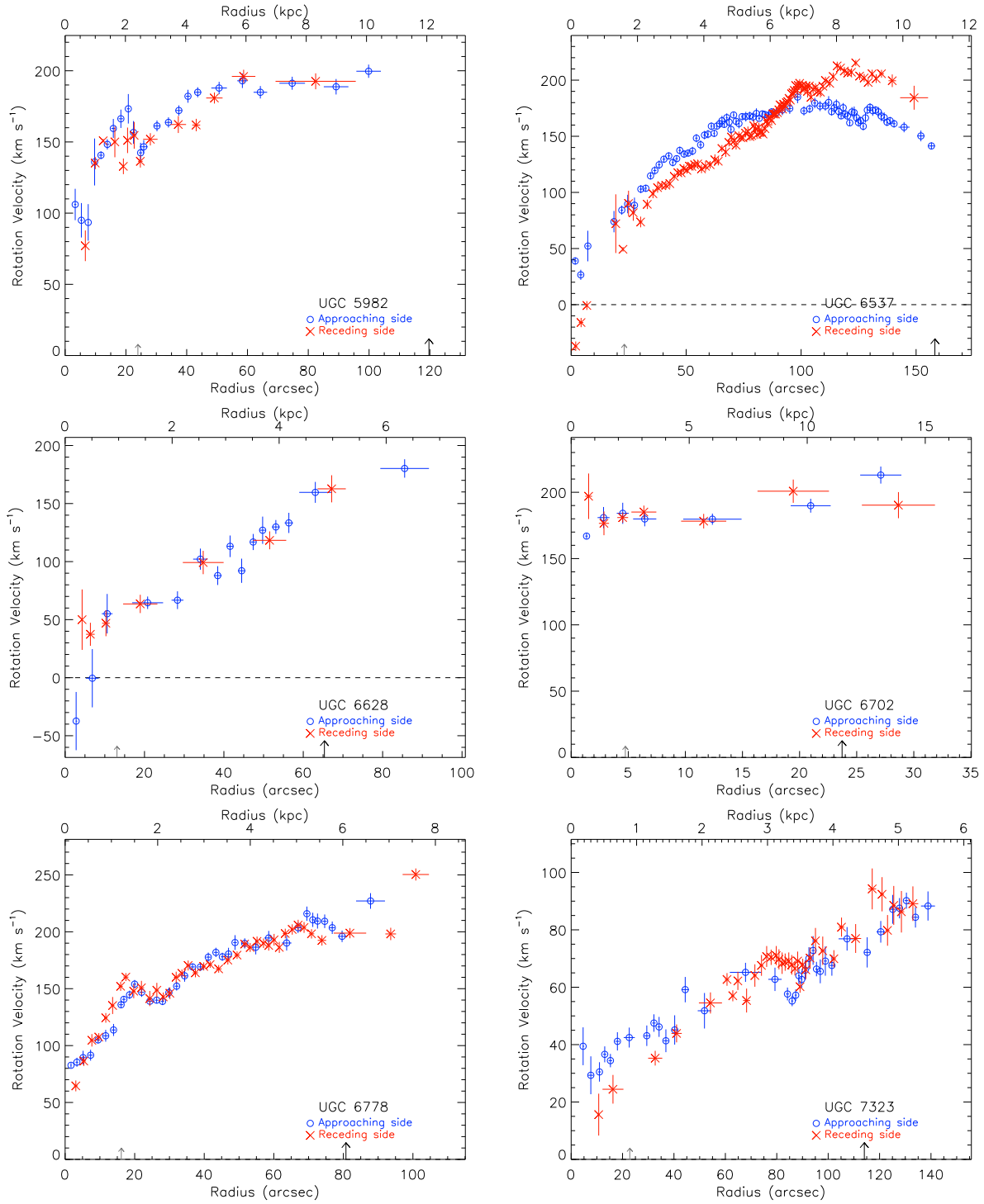


Figure E8. From top left to bottom right: $H\alpha$ rotation curve of UGC 5982, UGC 6537, UGC 6628, UGC 6702, UGC 6778, and UGC 7323.

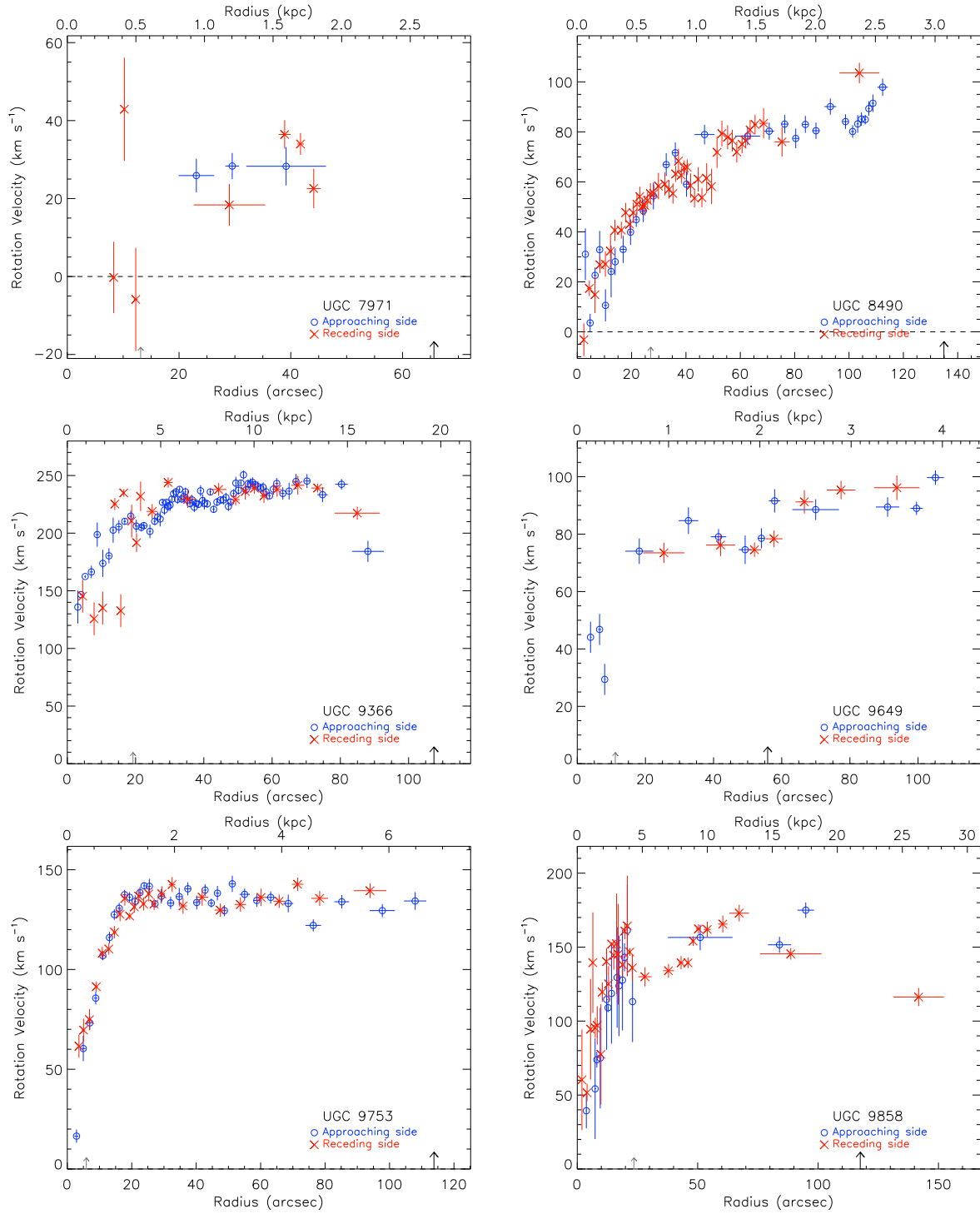


Figure E9. From top left to bottom right: H α rotation curve of UGC 7971, UGC 8490, UGC 9366, UGC 9649, UGC 9753, and UGC 9858.

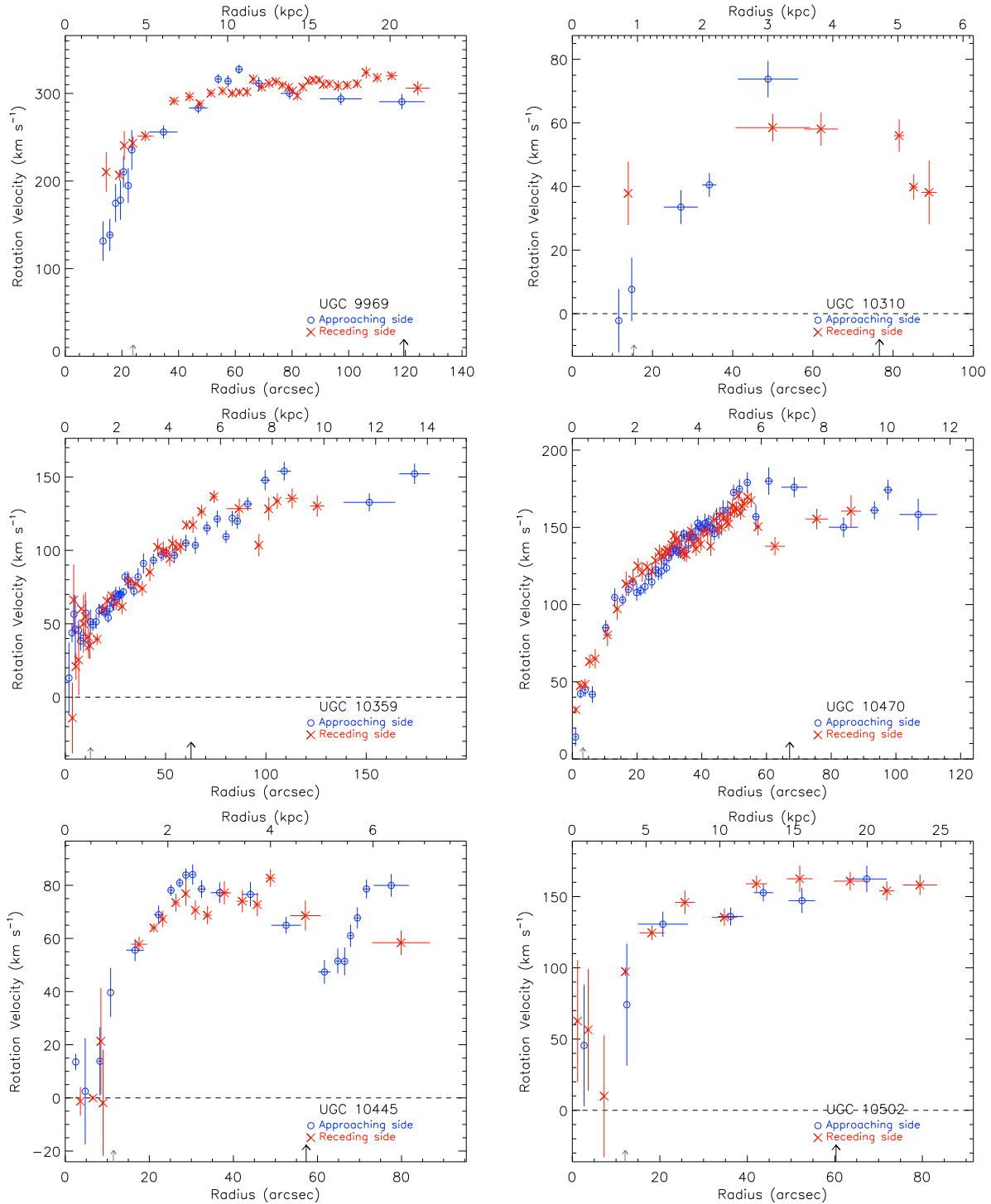


Figure E10. From top left to bottom right: $H\alpha$ rotation curve of UGC 9969, UGC 10310, UGC 10359, UGC 10470, UGC 10445, and UGC 10502.

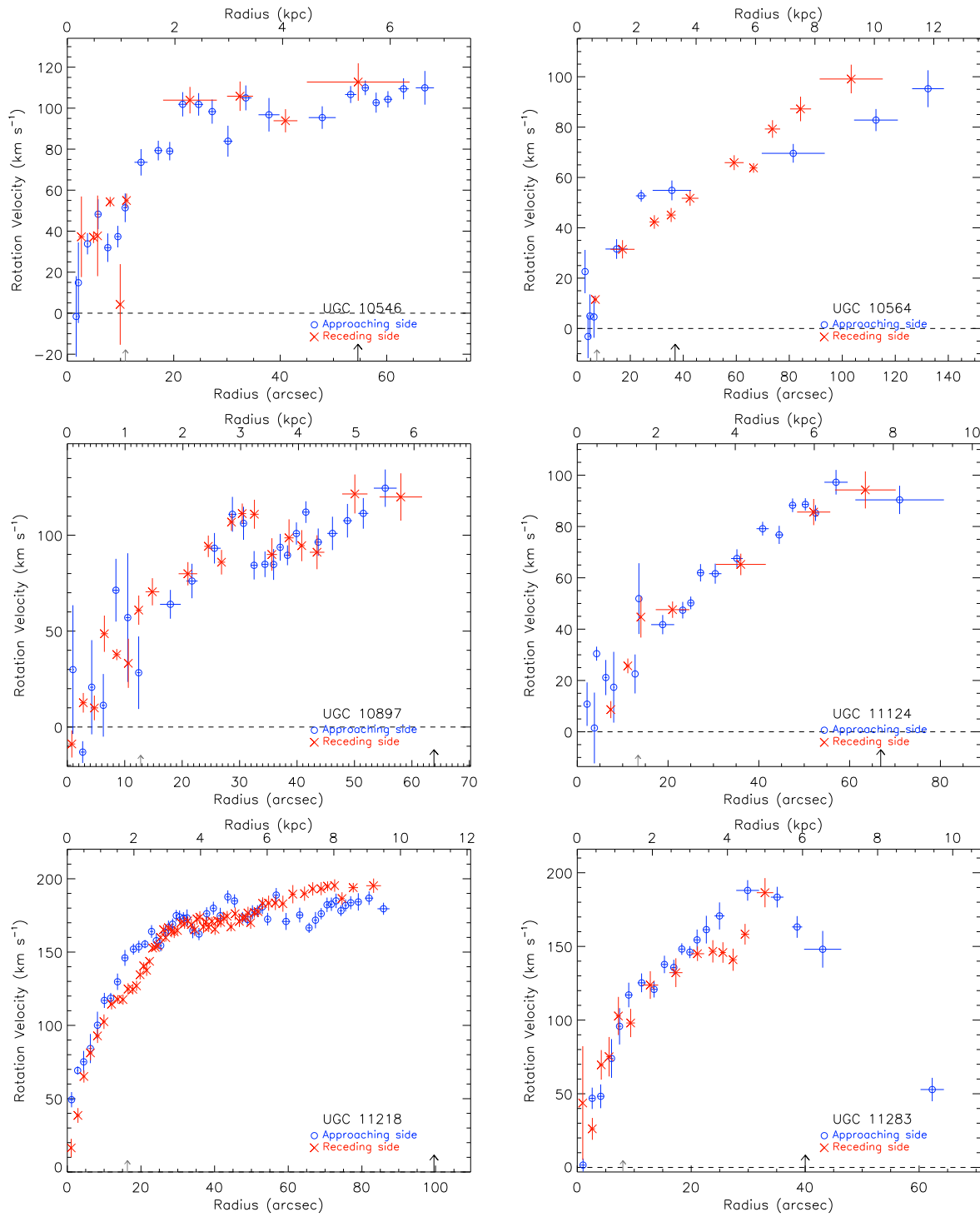


Figure E11. From top left to bottom right: H α rotation curve of UGC 10546, UGC 10564, UGC 10897, UGC 11124, UGC 11218, and UGC 11283.

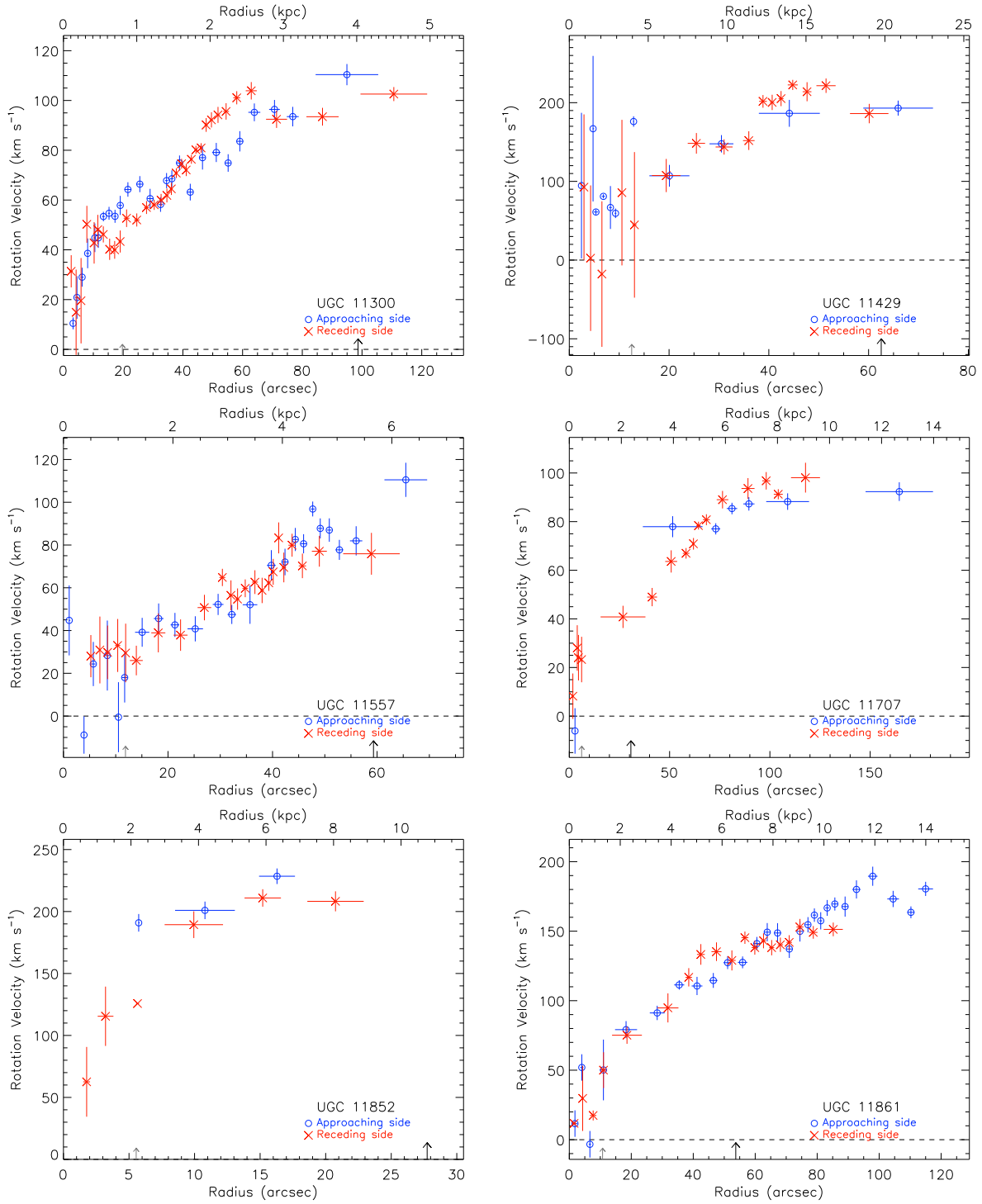


Figure E12. From top left to bottom right: H α rotation curve of UGC 11300, UGC 11429, UGC 11557, UGC 11707, UGC 11852, and UGC 11861.

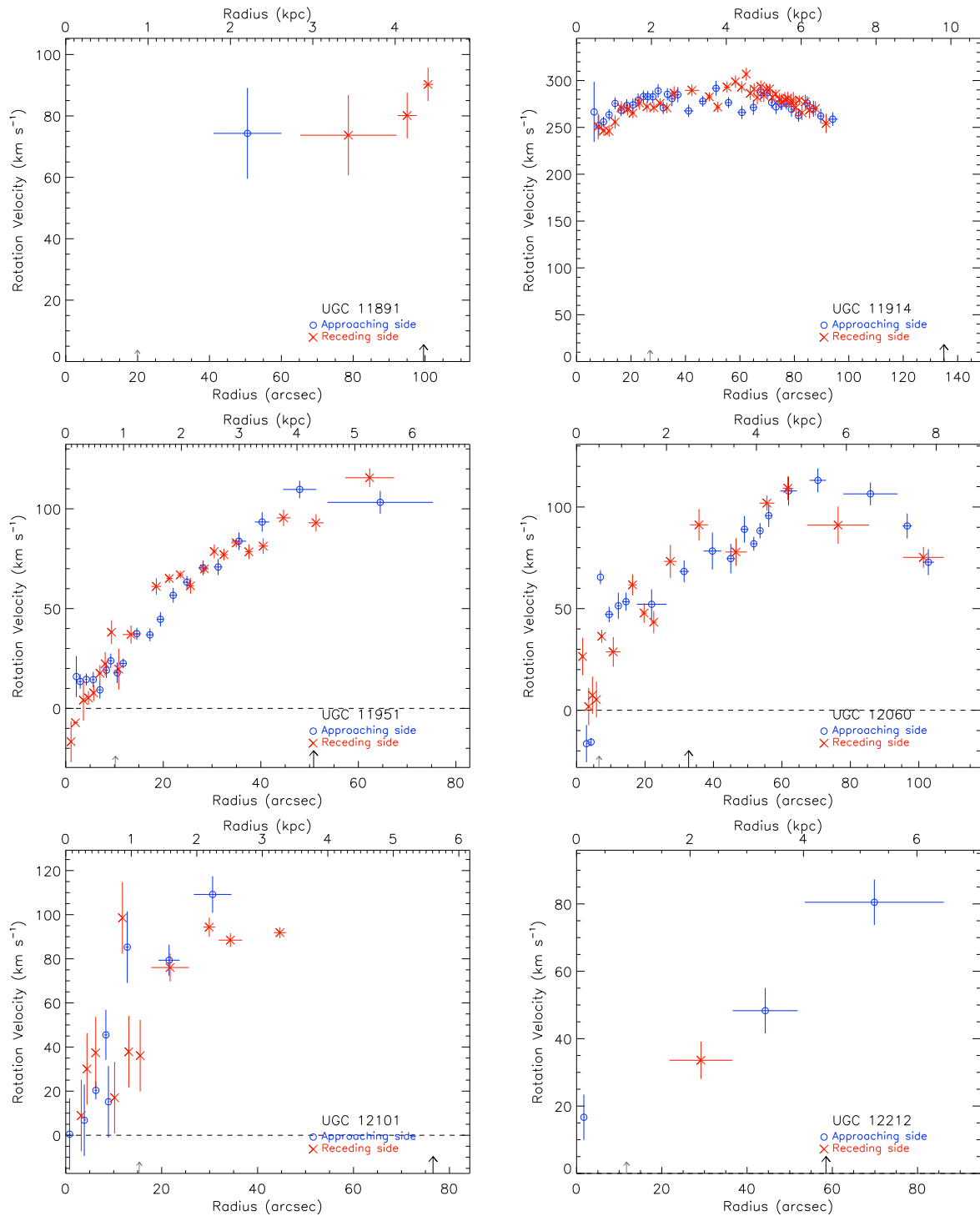


Figure E13. From top left to bottom right: $\text{H}\alpha$ rotation curve of UGC 11891, UGC 11914, UGC 11951, UGC 12060, UGC 12101, and UGC 12212.

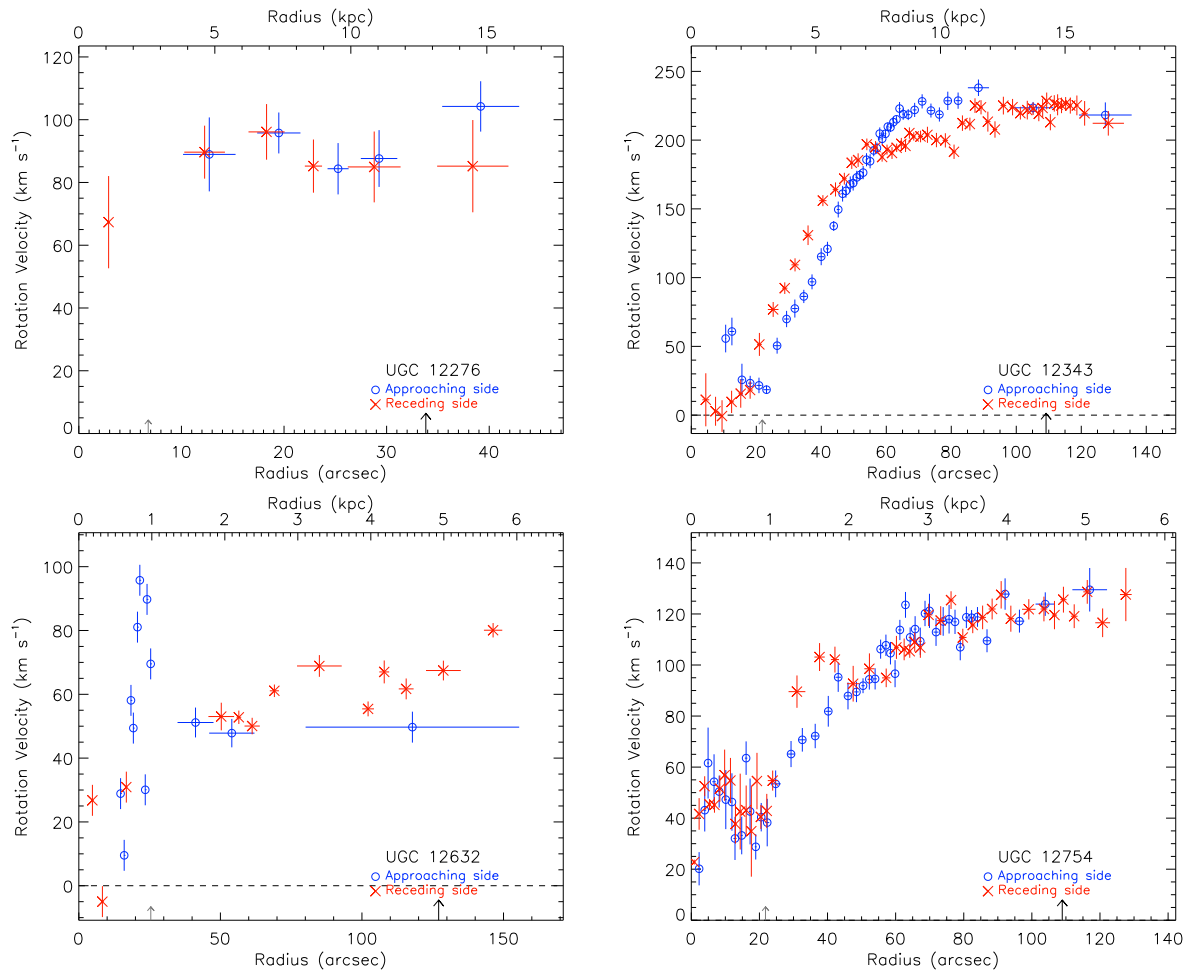


Figure E14. From top left to bottom right: $H\alpha$ rotation curve of UGC 12276, UGC 12343, UGC 12632, UGC 12754.

APPENDIX F: ROTATION CURVES TABLES

Table F1. UGC 00508 rotation curve

r (kpc) (1)	σ_r (kpc) (2)	r (") (3)	σ_r (") (4)	v (km s ⁻¹) (5)	σ_v (km s ⁻¹) (6)	N bins (7)	side (8)
0.28	0.00	0.9	0.0	307	124	1	a
0.28	0.00	0.9	0.0	364	124	1	r
0.97	0.11	3.1	0.4	269	29	4	a
1.28	0.00	4.1	0.0	390	124	1	r
1.56	0.00	5.1	0.0	439	124	1	a
2.14	0.24	6.9	0.8	329	42	2	a
2.61	0.20	8.4	0.7	463	49	3	a
2.98	0.00	9.6	0.0	312	124	1	r
3.12	0.00	10.1	0.0	307	124	1	a
3.71	0.10	12.0	0.3	395	22	3	a
4.39	0.00	14.2	0.0	410	124	1	r
4.61	0.03	14.9	0.1	479	42	2	a
4.73	0.00	15.3	0.0	323	124	1	a
5.51	0.03	17.8	0.1	493	72	2	a
5.75	0.00	18.6	0.0	466	124	2	r
7.78	1.14	25.2	3.7	454	18	23	a
7.81	1.02	25.2	3.3	490	19	23	r
9.69	0.39	31.3	1.3	465	15	23	r
10.14	0.38	32.8	1.2	471	13	23	a
10.64	0.18	34.4	0.6	491	12	23	r
11.12	0.29	35.9	0.9	468	18	23	a
11.20	0.16	36.2	0.5	488	10	23	r
11.66	0.19	37.7	0.6	496	13	23	r
12.09	0.27	39.1	0.9	514	14	23	a
12.48	0.27	40.3	0.9	499	13	23	r
13.30	0.50	43.0	1.6	499	16	23	a
13.68	0.37	44.2	1.2	497	13	23	r
14.82	0.32	47.9	1.0	530	14	23	r
14.85	0.48	48.0	1.6	501	14	23	a
15.76	0.27	50.9	0.9	526	14	23	r
16.37	0.38	52.9	1.2	540	13	23	a
16.90	0.43	54.6	1.4	565	12	23	r
17.47	0.36	56.5	1.2	526	17	23	a
18.54	0.57	59.9	1.8	567	12	23	r
19.83	1.82	64.1	5.9	553	19	17	a
20.11	0.34	65.0	1.1	541	14	23	r
21.11	0.24	68.3	0.8	553	15	23	r
22.24	0.67	71.9	2.2	514	17	21	r

(1), (3) Galactic radius. (2), (4) Dispersion around the galactic radius. (5) Rotation velocity. (6) Dispersion on the rotation velocity. (7) Number of velocity bins. (8) Receding – r – or approaching – a – side.